Order Number 9431379

Strangeness enhancement in heavy ion collisions at the AGS as a possible signature of the quark gluon plasma formation

Zhao, Kaihui, Ph.D.

City University of New York, 1994

U·M·I
300 N. Zeeb Rd.
Ann Arbor, MI 48106

A

STRANGENESS ENHANCEMENT IN HEAVY ION COLLISIONS AT THE AGS AS A POSSIBLE SIGNATURE OF THE QUARK GLUON PLASMA FORMATION

by

KAIHUI ZHAO

A dissertation submitted to the Graduate Faculty in Physics in partial fulfillment of the requirements for the degree of Doctor of Philosophy, The City University of New York.

1994

This manuscript has been read and accepted for the Graduate Faculty in Physics in satisfaction of the dissertation requirement for the degree of Doctor of Philosophy.

April 19, 1994
Date

Seymour J. Lindenbaum
Chair of Examining Committee

April 22, 1994
Date

Edward Tryon
Executive Officer

Chellis Chasman

Martin A. Kramer

Ronald S. Longacre

Stephen Orenstein
Supervisory Committee

THE CITY UNIVERSITY OF NEW YORK

ABSTRACT

STRANGENESS ENHANCEMENT IN HEAVY ION COLLISIONS AT THE AGS AS A POSSIBLE SIGNATURE OF THE QUARK GLUON PLASMA FORMATION

by

Kaihui Zhao

Advisor: S.J. Lindenbaum, Mark W. Zemansky Professor of Physics

Enhanced strangeness production was suggested a decade ago[1] as a possible signature of Quark Gluon Plasma (QGP), which is a state of unconfined quarks and gluons that will exist in superdense and hot nuclear matter as predicted by Quantum Chromodynamics (QCD). Theorists believe that such a state (QGP) existed in the early universe for $\sim 10^{-23}$ seconds, and could possibly be created in laboratory with relativistic heavy-ion collisions. We utilized the 14.6 $\times$ A GeV/c *Si* beam provided by the Alternating Gradient Synchrotron (AGS) at Brookhaven National Laboratory (BNL) to bombard different targets (Al, Si, W, Au, Pb, etc) in searching for a QGP. Particles produced in the forward hemisphere (NN center of mass system) from these collisions traveled through upto 3 TPC (Time Projection Chamber) modules which were in a 5 kilogauss magnetic field. Each detected track was recorded individually with regards to position,momentum and charge.

A significantly enhanced K^0_s and Λ production in relativistic heavy-ion collisions over that of a simple cascade of NN collisions was detected. But the enhancement of single strangeness particles may not be good signature of QGP, because secondary scatterings of resonant states (e.g. Δ and N^*) in a hadron gas may as well increase their production. This makes the multistrange hyperon (e.g.

Ξ^-) production a better alternative for a QGP signature, because its formation through resonant state rescatterings in hadron gas is more difficult than that of single strangeness particles (e.g. K^0_s, Λ). Excessive strangeness content in a QGP may favor Ξ^- production (as well as strangelets) during hadronization.

Copious production of Ξ^- has been detected with limited statistics. The measured ratio of $N(\Xi^-)/N(\Lambda)=0.12\pm0.02\pm0.025$ is at least 3 times larger than the predictions of generally known hadronic cascade models. Various models and general considerations have been explored trying to understand the physical implications of the experimental results.

Acknowledgements:

I would like to take this opportunity to thank the many people who have contributed to this thesis directly and indirectly.

To begin with the direct contributors. It is impossible to adequately thank my advisor, Prof. Seymour J. Lindenbaum, for everything he has done for me. His dedication to and enthusiasm for physics are inspiring. His four decades outstanding career in physics has benefitted me with his tremendous experience and wisdom. He led me into the field of relativistic heavy ion physics five years ago and guided me through from choosing thesis subject to finishing this thesis. He was the first one to insist that we should look into multiple strange particle production signals when people just started reporting single-strange enhancement over that of a cascade of NN data. Having a brief discussion with him is always invaluable, he can grab the important points in minutes and offer valuable advice.

Besides, I can always count on his constant support and positive encouragement when things are not easy. It warms your heart and gives your confidence. He is tireless in working toward providing his group with the first-class physics environment from which I have benefitted greatly.

Dr. Ronald S. Longacre can also not be thanked enough. Many of the analyses presented in this thesis were done with his expert help and discussions, such as calculating acceptance when statistics were low. He is always ready to discuss physics problems with me. I enjoyed the many enthusiastic discussions with him.

Dr. Robert Hackenburg has taught me a lot of things in hardware aspect of high energy physics experiments (from detector repaire, fast trigger logic to data acquisition) when I worked on setting up E881 under his direct leadership and had enthusiastic discussions with him.

At CCNY, Prof. M.A. Kramer and Prof. C.S. Chan also have been helped in every step of my thesis work. Especially in the first two years, the two of them have offered very valueable help in introducing me to this new field.

My fellow students Yujie Zhu, Efstratos Efstathiadis and engineer Bill Licciardi have been very helpful during all these years on analyzing E810 data and setting up E881. I especially enjoyed taking shift with them when running experiments (E810 & E881) and discussing physics with them when analyzing data.

At the Brookhaven National Laboratory, Dr. K.J. Foley, Dr. E.D. Platner, Dr. R.W. Hackenburg, Dr. A. Etkin and Steve Eiseman have designed and built (hardware) the TPC modules before I came to participate in E810 data taking. Dr. W.A. Love, Dr. T. Morris and Dr. A.C. Saulys have designed and developped the E810 software system and also analyzed the data on K^0_s and Λ production and their various distributions in addition to the AGS baryon stopping and π^- correlation (HBT) studies. It was their pioneering work, that has made the analysis presented in this thesis possible.

Don David, Carl Jacobs, Tom Mogavero, Danny Padrazo, Bob Chmiel, Hank Arnesen, Lee Hawkins and Larry Toler have been very helpful during the period. Especially during the first two years and when running experiments, I learned a lot from them. I want to particularly thank Tom Mogavero. With my little knowledge of electronic devices, I often went to him for help when I had difficulty on my project. I'll always miss him.

Sharon Smith and Liz Mogavero have helped on a large amount of paper work for an off campus foreign student to survive.

My biggest thanks goes to my parents for taking care of my son and my son for having to live 8000 miles away from his parents. I hope I made them proud.

Finally, for the constant support of a host of family and friends, I owe a debt that cannot be repaid any more than it can be forgotten. My loving gratitude to you all.

This work was completed with the support of the United States Department of Energy.

Contents

Title Page i

Approval ii

Abstract iii

Acknowledgments v

Contents viii

List of Tables xi

List of Figures xii

1. Introduction 1

1.1 The Strong Interaction 1

1.2 The Carrier of the Strong Force 2

1.3 Baryons, Mesons, and Leptons 5

1.4 The Quarks: Flavors and Colors 6

1.5 The Quantum Chromodynamics(QCD) 8

1.6 The Role of Gluons in QCD 9

1.7 Testing QCD 11

1.8 Searching For QGP 13

2. Strangeness Production in QGP and Hadron Gas 15

2.1 Why Strangeness 16

2.1.1 Pauli Blocking Effect 17

2.1.2 Higher Strangeness Production Rates 17

2.1.3 High Density of Strangeness in QGP 19

2.1.4 The Role of Gluons in QGP 19

2.1.5 Stopping Power For Heavy Ions at the AGS 21
2.1.6 MPS TPC With Wide Rapidity Coverage 22
2.2 Previous Data on Strangeness Production 23
2.2.1 K/π Ratio and the RQMD Model 23
2.2.2 K^0_s, Λ Production and Models(ARC and AGSHIJET+N*) 27
3. Experimental Apparatus 31
3.1 The MPS Magnet 31
3.2 The TPC Modules 32
3.3 The Electronics 37
3.4 The Gas System 39
3.5 The *Si* Beam 41
3.6 The Trigger 43
3.7 The Data Acquisition(DAQ) System 43
3.8 The Track Reconstruction 46
4. The Experimental Procedure 52
4.1 Experimental Method 52
4.2 Event Selection—Centrality Cuts 56
4.3 Data Analysis 57
4.4 Acceptance Calculation 67
5. The Results and Discussions 70
5.1 The Rapidity Distributions of K^0_ss and Λs 70
5.2 The Transverse Mass Distributions of K^0_ss and Λs 77
5.3 The Cascade Models' Predictions of Strangeness Production 89
5.4 The Ξ^- Production 98
5.5 The Multi-Λ Production 110
5.6 The Possible Resonant States That Decay Strongly 110
5.7 Have We Seen The QGP ? 113

6. Summary 120

References 126

List of Tables

Table[1.1] Quark–lepton table implying another spin 1/2 quark may exist 7

Table[1.2] Quarks with their quantum numbers 8

Table[5.1] χ^2 propabilities for the fits of fireball$^+$ and cascade models. 89

Table[5.2] Ξ^-/Λ ratio in E810 Si+Pb data compared with models 109

Table[6.1] Ξ^-/Λ ratio in E810 Si+Pb data compared with models 124

List of Figures

Figure[1.1] An exchange of a pion between two nucleons 3

Figure[1.2] Two quarks interact via exchange of a gluon.....10

Figure[1.3] Gluons interact with each other 11

Figure[2.1] Proposed mechanism of strangeness enhancement 18

Figure[2.2] A pair of strange quarks created in hadron collision 20

Figure[2.3] K/π enhancement in Si+Au collisions at AGS 24

Figure[2.4] a) η distribution of charged particles in Si+Au with RQMD fit. ... 25

Figure[2.4] b) P_t distribution of $K^{\pm}$ and $\pi^{\pm}$ in Si+Au with RQMD fit. 26

Figure[2.5] Rapidity distribution of K^0_s from Si+Si 28

Figure[2.6] Rapidity distribution of Λ from Si+Si 29

Figure[3.1] Front view of a TPC module showing principle components 33

Figure[3.2] Overview of 3 TPC modules in operating position 34

Figure[3.3] A close look of a TPC module's readout electronics.....35

Figure[3.4] Schematic of the electrodes in the TPC end cap 36

Figure[3.5] Schematic of individual channel electronics. 38

Figure[3.6] A 128-channel hybrid printed circuit boards. 40

Figure[3.7] The AGS complex 42

Figure[3.8] Plan view of E810 apparatus 44

Figure[3.9] The MPS DAQ system hardware block diagram 45

Figure[3.10] a) X-Z view of a reconstructed Si+Au events 48

Figure[3.10] b) Y-Z view of a reconstructed Si+Au events 49

Figure[3.10] c) Y-X view of a reconstructed Si+Au events 50

Figure[3.10] d) 3-dimensional view of a reconstructed Si+Au events 51
Figure[4.1] The location of TPC and trigger detector in MPS the magnet 53
Figure[4.2] The MPS DAQ system hardware block diagram 55
Figure[4.3] Effective mass plot of the $\pi^+\pi^-$ hypothesis in Si+Pb 58
Figure[4.4] Effective mass plot of the π^-p hypothesis in Si+Pb 59
Figure[4.5] Effective mass plot of the $\pi^-\Lambda$ hypothesis in Si+Pb 61
Figure[4.6] Z-X view of a Ξ^-s decaying in TPC modules 63
Figure[4.7] Enlarged Z-Y view of the same Ξ^-s decay 64
Figure[4.8] Invariant mass for $\pi^-\Lambda$ from different events. 65
Figure[4.9] Invariant mass for $\pi^-\Lambda$ from different Monte Carlo events. 66
Figure[4.10] The acceptance for V^0 were calculated in grids 68
Figure[5.1] Yield of Λ increases with negative track number. 71
Figure[5.2] K^0_s lifetime detected in Si+Au 73
Figure[5.3] Λ lifetime detected in Si+Au 74
Figure[5.4] Rapidity distribution of K^0_s from Si+Si 75
Figure[5.5] Rapidity distribution of K^0_s from Si+Pb 76
Figure[5.6] Rapidity distribution of Λ from Si+Si 78
Figure[5.7] Rapidity distribution of Λ from Si+Pb 79
Figure[5.8] M_t distribution of K^0_s from Si+Si 80
Figure[5.9] M_t distribution of K^0_s from Si+Pb 81
Figure[5.10] M_t distribution of Λ from Si+Si 83
Figure[5.11] M_t distribution of Λ from Si+Pb 84
Figure[5.12] Inverse exponential slopes for K^0_s from the Si target. 85
Figure[5.13] Inverse exponential slopes for K^0_s from the Pb target. 86
Figure[5.14] Inverse exponential slopes for Λ from the Si target. 87
Figure[5.15] Inverse exponential slopes for Λ from the Pb target. 88
Figure[5.16] N* effective mass spectrum generated by MINBIAS. 92

Figure[5.17] Y distribution of K_s^0 produced by RANDOM for Si+Pb 96
Figure[5.18] Y distribution of Λ produced by RANDOM for Si+Pb 97
Figure[5.19] Lifetime of Ξ^- from Si+Pb 102
Figure[5.20] Ξ^- acceptance (using AGSHIJET+N*) as a function of Y 103
Figure[5.21] Y distribution of Ξ^- (acceptance corrected using AGSHIJET+N*) 104
Figure[5.22] M_t distribution of baryons from Si+Pb 105
Figure[5.23] Ξ^- acceptance (using fireball$^+$) as a function of Y 107
Figure[5.24] Y distribution of Ξ^- (acceptance corrected using Fireball$^+$) 108
Figure[5.25] Number of central events with multi-Λ production 111
Figure[5.26] Primary $\pi^- p$ invariant mass 112
Figure[5.27] Separation of the fireball from the fragmentations 116
Figure[5.28] Σ/Λ ratio as a function of Y 117
Figure[5.29] χ^2 confidence level .vs. α 118

Chapter 1

Introduction

According to Quantum Chromodynamics(QCD), a new phase of matter called the Quark Gluon Plasma(QGP) will be formed under extreme thermodynamic conditions within a relatively large region where quarks and gluons may be conceivably dissolved from the normal confined states. The discovery and understanding of such a phase is of fundamental importance for studying strong interaction.

1.1 The Strong Interaction

When physicists first considered the structure of the atomic nucleus, they confronted a mystery. They knew that the nucleus was composed of nucleons— the protons and neutrons—and that heavy elements have many protons in the nucleus (uranium, for example, has ninety-two). But how can such a large quantity of protons be reconciled with the laws of electrodynamics, which prohibit the existence of so many particles of like charge in such a tiny space? The electric repulsion between these protons is so great that the nucleus should explode. According to the laws of electrodynamics, therefore, atomic nuclei should not be stable. There is only one solution to the problem: there must exist in nature another basic force that keeps the atomic nucleus together. This force indeed exists and is called the strong nuclear force or the strong interaction. It is the force responsible for the formation of atomic nuclei. It is very strong indeed: a naive estimate is that the strong interaction is at least one hundred times stronger than the electromagnetic interaction, whose strength is given by the fine-structure constant α=1/137.

Of course we can not help but ask at once why we do not observe the effects of the strong interaction in every day life the way we observe electromagnetic effects. The answer lies in a special property of the strong interaction: it is active only at very short distances, distances on the order of 10^{-12} cm. As soon as nucleons are removed farther apart from each other than 10^{-12} cm, the strong interaction has scarcely any effect. The dominant force between nucleons at such distances is the electromagnetic force. However, if the nucleons are brought close to each other again, the strong interaction very rapidly dominates. This is why atomic nuclei are stable and do not explode. Nucleons inside a nucleus are indeed very close to each other (10^{-13} cm or less), and their behavior is dictated by the strong nuclear force, which dominates over the electric repulsion between the protons.

Although we cannot see the effects of the strong interaction directly in everyday life, we can at least observe them indirectly. For example, the strong interaction is exceedingly important in nuclear power plants; the energy produced by a nuclear reactor is obtained through rearrangements of nucleons. The same principle applies in atomic and hydrogen bombs.

1.2 The Carrier of the Strong Force

We already knew in quantum electrodynamics that the interaction between charged objects (electric attraction or repulsion) is governed by the exchange of virtual photon quanta between them. The question immediately comes to mind as to whether we can understand the strong interaction between strongly interacting particles by means of a similar exchange principle. The suggestion was made 60 years ago by Hideki Yukawa, who proposed that the strong interaction results from the exchange between nucleons of quanta called mesons (Figure[1.1]).

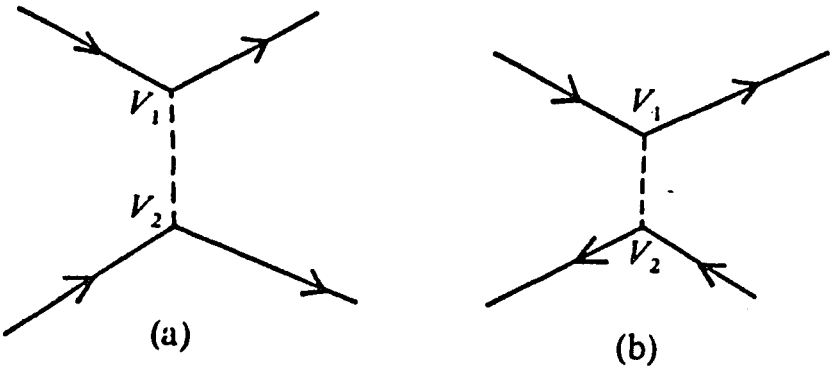

Figure[1.1] (a) $NN \rightarrow NN$, a single exchange of a pion between two nucleons. **Figure[1.1] (b)** $N\bar{N} \rightarrow N\bar{N}$, the arrow direction travelling backward in time on the nucleon line is equivalent to an anti–nucleon travelling forward in time.

Yukawa brilliantly demonstrated that the reason the electromagnetic force was long-range was a consequence of the zero rest mass of the photon, which was the field quantum responsible for the electromagnetic interaction, and that the range of a force was intimately related to the rest mass of the quanta of the field responsible for the interaction.

The equation he considered as the wave equation for a non-zero rest mass particle is just the relativistic Klein-Gordon equation. This equation can easily be obtained by the usual quantum mechanical substitution of operators for observables in the corresponding classical equation, using the well known prescription

$$p = \frac{\hbar}{i}\nabla, \tag{1.1}$$

$$E = i\hbar\frac{\partial}{\partial t}, \tag{1.2}$$

and allowing the operators to operate on the wave function or state vector. The relativistic classical equation is

$$E^2 = p^2c^2 + m_0^2c^4, \tag{1.3}$$

where E is the total energy, p is the momentum, c is the velocity of light, and m_0 is the particle rest mass. With the substitutions (1.1) and (1.2) we obtain

$$(\nabla^2 - \frac{m_0^2c^2}{\hbar^2} - \frac{1}{c^2}\frac{\partial^2}{\partial t^2})\varphi = 0, \tag{1.4}$$

where φ is the particle wave function and is here considered to be a one component wave function. Since we require invariance under Lorentz transformation, φ must be a scalar or a pseudoscalar (a scalar quantity which changes sign upon space inversion or time inversion).

If we regard an infinitely heavy nucleon as the source of the strong field, analogously to the fixed point charge sources of the photon field in electromagnetic theory, the Klein-Gordon equation for scalar quanta with an infinitely heavy nucleon source at the point r_1 , becomes

$$(\nabla^2 - \frac{m_0^2c^2}{\hbar^2} - \frac{1}{c^2}\frac{\partial^2}{\partial t^2})\varphi = -4\pi g_1\delta(\mathbf{r} - \mathbf{r_1}), \tag{1.5}$$

where g_1 is the charge constant analogous to e in the electromagnetic case.

If we look for the static solution by letting $\frac{\partial}{\partial t} = 0$, we find

$$\varphi(\mathbf{r} - \mathbf{r_1}) = -\frac{g_1}{|\mathbf{r} - \mathbf{r_1}|}\exp(\frac{-|\mathbf{r} - \mathbf{r_1}|}{\hbar/m_0c}), \tag{1.6}$$

The potential of a second nucleon located at point r is, again analogously to the electromagnetic case,

$$V = g_2\varphi(\mathbf{r} - \mathbf{r_1}) = \frac{-g_1g_2}{|\mathbf{r} - \mathbf{r_1}|}\exp(\frac{-|\mathbf{r} - \mathbf{r_1}|}{\hbar/m_0c}), \tag{1.7}$$

Since $g_1 = g_2 = g$,

$$V = \frac{-g^2}{|\mathbf{r} - \mathbf{r_1}|} exp(\frac{-|\mathbf{r} - \mathbf{r_1}|}{\hbar/m_0 c}), \tag{1.8}$$

Where m_0 is the rest mass of the exchange quanta (called π meson later) of this strong field.

Eqn (1.8) represents the Yukawa potential. We observe that it's an attractive force and it drops rapidly with separation. From the effective range of the strong interaction, Yukawa predicted that there should be a new kind of particle (he called it meson) mediated strong interaction and having a mass of about 100 MeV. It was later confirmed by experiment that meson π did exist and possessed a mass of 140 MeV.

It is obvious that when $m_0 \rightarrow 0$ in Eqn (1.8), we obtain the ordinary Coulomb potential which is a long range force due to the zero rest mass of photon.

1.3 Baryons, Mesons, and Leptons

The experiments not only confirmed the existence of π meson, but the existence of many π mesons: π^+, π^- and π^0 etc. Eventually, more and more mesons were discovered, such as K^+, K^-, K^0 and ρ, ϕ etc. These mesons spread among a large range of mass, which means that the strong interaction produced by exchanging these mesons could vary drastically.

With the discovery of many mesons, all kinds of baryons were also discovered, they are: Δ^-, Δ^0, Δ^+, Δ^{++}, Σ^-, Σ^0, Σ^+, Λ and Ξ^0, Ξ^- etc.

Besides the mesons and baryons (the strongly interacting particles known collectively as hadrons), there is another group of particles that do not participate in

strong interaction but do have spin$\frac{1}{2}$, they are called leptons. (but photons are not since they have spin 1)

Leptons can be classified into the following three groups:

$$(\nu_e, e^-) \qquad (\nu_\mu, \mu^-) \qquad (\nu_\tau, \tau^-)$$

If we compare the world of hadrons with the world of leptons, we find that there are an abundance of the former but only six leptons observed so far. This situation raise our suspicion that leptons in some sense are more elementary than hadrons and that hadrons are composite systems, consisting of yet smaller and more elementary units. During the past 30 years, physicists have discovered that this supposition is indeed correct, that the hadrons are made up of simpler particles, the quarks.

1.4 The Quarks: Flavors and Colors

The quark model was first proposed in 1964 by Gell-Mann and Zweig, who assumed that all mesons are composed of quark anti-quark pairs ($q\bar{q}$) while all baryons are three quark states (qqq). Where q represents quarks and $\bar{q}$ represents anti-quarks. The different species of quarks are referred as flavors. Most of the world consists of up quarks (u quarks) and down quarks (d quarks), for example, protons are made of uud and neutrons consist of udd while $\pi^+(u\bar{d})$, $\pi^-(\bar{u}d)$ and so on. Some of the unstable mesons and baryons contain heavier quarks such as strange quark (s quark), charmed quark (c quark), bottom quark (b quark). Another quark called top quark (t quark) is expected to exist (predicted by theory) to make the quark—lepton table (Table[1.1]) complete.

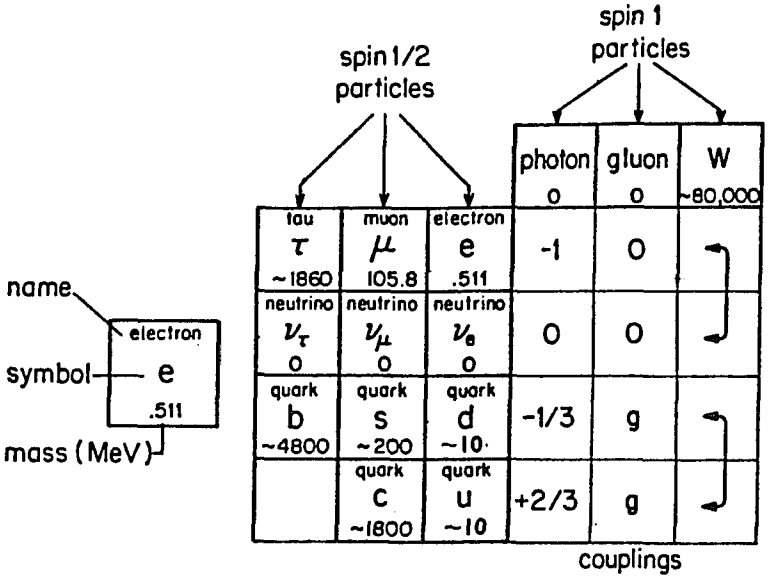

Table[1.1] Quark—lepton table implying that there might exist another spin 1/2 quark.

Another quantum number was introduced in the quark model in order to avoid breaking Pauli exclusion principle (quarks are fermions) when explaining the existence of some ground state baryons made up of the same flavors of quarks, such as $\Delta^{++}(uuu)$ and $\Delta^{-}(ddd)$. This new quantum number we call it color (it has nothing to do with the color we see with our eyes). Three colors are necessary (no more no less) to distinguish these three identical quark. They are green, red, and blue. The real world is colorless because mesons and baryons are color singlets, that means three quarks in a baryon must possess three different colors (or their supplements) and the two quarks in any meson must have supplemental colors.

There are other quantum numbers assigned to each quark to make the quark model self-consistent. Each quark is said to have spin 1/2 and a baryon number 1/3, u quark has electric charge 2/3 and d quark has charge −1/3. Other quarks

and their quantum numbers are shown in Table[1.2] .

Quantum number	d	u	s	c	b	t
Q—electric charge	-1/3	+2/3	-1/3	+2/3	-1/3	+2/3
I_z—isospin z-component	-1/2	+1/2	0	0	0	0
S—strangeness	0	0	-1	0	0	0
C—charm	0	0	0	+1	0	0
B—bottomness	0	0	0	0	-1	0
T—topness	0	0	0	0	0	+1

Table[1.2] Quarks with their quantum numbers.

1.5 The Quantum Chromodynamics(QCD)

For the past 30 years, theorists have worked out a theory called quantum chromodynamics (QCD) which in many ways similar to the well established quantum electrodynamics (QED). As we have shown in Section 1.2, the strong interaction between nucleons are carried out by exchanging virtual mesons. In QCD, the fundamental mechanism of this scheme is the interaction between quarks by exchanging gluons. Gluons also have color and interacting between themselves. By emitting or absorbing a gluon during interaction, a quark may change color.

One major difference between QCD and QED is the magnitude of the coupling constant: α =1/137 in QED, while renormalized QCD coupling is small only at high energies, and it is only in this domain that moderate precision ($\sim$ 10–15%) tests—similar to those in QED (but with high precision)—can be performed using perturbation theory. For example, it turns out from electron and neutrino scattering that $\alpha_s \approx 0.2$, though still much larger than 1/137 in QED, it means that the quarks seen in the experiments behave largely as independent, nearly pointlike objects.

This made the multi-photon exchange cases have cross-sections of smaller value

in QED which is treatable with perturbative calculation to significant precision, while multi-gluon exchange cases are unneglectable (actually represent considerable contributions) in low energy (non-perturbative) QCD so that perturbative calculation is unusable. Since there is nothing relatively easy except perturbative calculations in field theory to calculate results which can be compared with experiments, the test of non-perturbative QCD has been difficult. It should be noted that lattice gauge calculations can in principle handle non-perturbative (i.e. soft QCD) problems, but in practice the difficulty and required massive computer capacity of these calculations has led to limited approximate calculations.

QCD is almost a traditional renormalizable quantum field theory. One feature that separates it from the others and makes it so extraordinarily difficult to test is that the quantum fields–the fundamental dynamical variables– do not correspond to the observed asymptotic particles. Rather than the baryons and mesons, it is the quarks and gluons out of which the theory is constructed. These constituents, as far as we know, are confined to the interior of mesons and baryons by the QCD forces which become strong at distances on the order of one fermi. The fact that the particles we can get our hands on are strongly coupled bound states of the fundamental particles is a major reason that there is yet no decisive test of QCD. Another major reason is the strong coupling in the non-perturbative region.

1.6 The Role of Gluons in QCD

In field theory, interactions are mediated by gauge bosons. In QCD, gluons are the gauge bosons mediating the strong interaction, gluons are assumed to be massless. The particles (quarks and gluons) that interact strongly are said to possess a quantum number called color that occurs in three varieties. Gluons carry color

and couple with things having color. Quarks are the only fundamental fermions that carry color. A quark's color can be changed when the quark emits or absorbs a gluon. The gluons come in eight different types, according to the colors they can carry. For example, if a red quark changes to green, it emits a red-antigreen gluon (antigreen means the gluon is carrying green in the opposite direction). This gluon could be absorbed by a green quark, which changes to red (see Figure[1.2]).

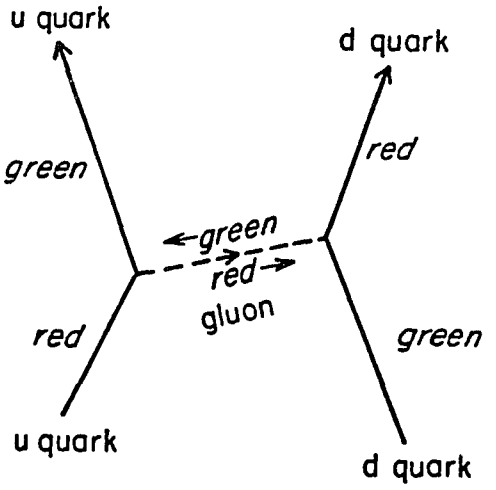

Figure[1.2] Gluon theory differs from electrodynamics in that gluons couple with things that are "colored"(red, green or blue). Here, a red u quark changes to green by emitting a red-antigreen gluon that is absorbed by a green d quark changing to red.(If the "color" is being carried backwards in time, it takes the prefix "anti".)

Because gluons possess color, gluons can interact with other gluons—just follow the colors: for instance, a green-antiblue gluon meeting a red-antigreen gluon results in a red-antiblue gluon, as shown in Figure[1.3].

Colorless particles such as leptons are free of strong interaction. All the ex-

perimentally measurable hadrons(baryons & mesons) are color singlets and consist of colored quarks and gluons. Strong interactions exist within hadrons(between quarks) but not between hadrons when the distance between hadrons is appreciably larger than the effective range of the strong force. When hadrons are close enough (at fermi level), strong interactions do exist between them although they are color singlets, such as the interactions between nuclei within the nucleus.

The coupling of the strong force increases with quark separation (within a certain range), as does their potential energy. When the potential energy is increased high enough to create a $q\bar{q}$ pair, this new quark pair will recombine with the existing quark pair to form two color singlets(hadrons) and this process can continue by creating additional quark, anti-quark pairs which form other hadrons (e.g. jets).

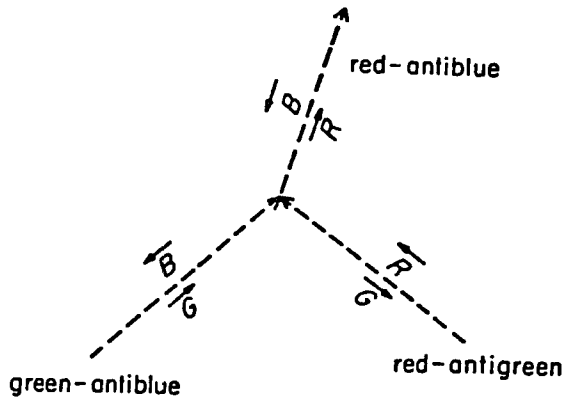

Figure[1.3] Since gluons are themselves "colored", they couple to each other. Here a green-antiblue gluon couples with a red-antigreen gluon to form a red-antiblue gluon.

1.7 Testing QCD

The verification or rejection of QCD will probably only come incrementally. QCD predicted that under extreme conditions of high density(energy) and high temperature created by relativistic heavy ion collisions, a state of unconfined quarks and gluons(QGP) will be formed in the central fireball region. The hot fireball will remain in the quark gluon plasma phase only for a very short time(typically $\tau_p \approx$5–10 fm/c = 1.5–3.0$\times 10^{-23}$ s are expected). After this time, its temperature has dropped below the critical temperature T_c due to expansion and radiation of particles from the surface. Below T_c the fireball matter will return to the hadronic phase with a possible intermediate period of supercooling. Initially, the density of the hadronic phase will still be very high and only drop during expansion. Until the density has become so low that the average inter-particle spacing is larger than the range of strong interactions, the hadrons in the fireball still interact violently. If the fireball would exhibit any characteristic kinematical signature during the time it spends in quark gluon plasma phase, this signature would very likely be destroyed by the hadronic final state interactions. If one were to rely on an analysis of the momentum space distribution of final hadrons to prove the temporary existence of the quark gluon plasma, the experiments might be quite inconclusive. Any analysis promising success must be based on the observation of properties that are not affected by final hadronic state interactions. Two such observables might be: (a) particles that do not interact strongly, and (b) quantum numbers that remain unchanged by strong interactions.

Strangeness production is one of the typical cases of (b). Strange number remains unchanged in strong interactions. On the other hand, since strangeness did not exist before the initial interaction, all the strangeness we detect could only be produced in the initial collisions and in the hadronization processes later on. While

multi-strange hyperons are difficult to be produced in secondary collisions, they may bring much cleaner signals about the temporary quark gluon plasma phase if it ever existed.

1.8 Searching For QGP

While the work of searching for QGP includes many aspects of this field: measurement of energy flow and energy density, multiplicity and their fluctuations, particle spectra and correlations, direct photons and dileptons, suppression of J/ψ's, production and flow of strange particles, this thesis will concentrate only on the role of strange particles as a distinctive probe to observe the formation and properties of the QGP.

The QGP cannot be observed directly except through its confined hadronic decay products. This fact raises the question of background processes, such as the behavior of the highly excited but confined nuclear matter(Hadron Gas) of which a quantitative understanding is a pre-requisite for the confirmation of the existence of QGP.

Thorough investigations of both the QGP decay products and the hadron gas evolution are very crucial for drawing a conclusion in this field. The current data at the available energies will still be extremely valuable in searching for a QGP even though the explanation of current experimental results do not have to employ a QGP scenario.

So it is very important to study strange particle production in collisions at the AGS energy even if no QGP is created, because it helps us understand the backgrounds to the QGP signatures and disentangle the various experimental signals,

at the same time as we learn about the confined nuclear matter.

For the last decade, a number of research groups at BNL and CERN have been actively pursuing experiments in searching for QGP by utilizing the heavy ion beams provided. This thesis studied the strangeness enhancement as a possible signature of QGP formation in Heavy ion collisions at the AGS based on the experimental data of E810.

Chapter 2

Strangeness Production in QGP and Hadron Gas

Nearly all matter around us is built of up (u) and down (d) quarks. However, as soon as adequate excitation energy becomes available in hadronic interactions, it becomes apparent that further quark flavors exist and are easily accessible. The lightest of the heavy flavors of matter is the strangeness. In the laboratory experiments excitation of strange matter is understood in terms of matter–antimatter formation as it is the s–$\bar{s}$ quark pair which is created in reaction processes by strong or electromagnetic interactions. The formation mechanism of strange quarks is highly correlated to the reaction mechanism governing the hadronic collisions—our current understanding of which suggests that the strangeness generation (especially the abundance of multistrange hadrons production) in nuclear collisions may be a very useful signature of the QGP formation.

It is quite imaginable that under extreme conditions of high hadron density and temperature in nuclear collisions, various fundamental properties of strange quark production could be altered. In a relativistic heavy ion collision, a domain in space arises in the center of mass frame of two nuclei in which an important part of the longitudinal energy is transferred to transverse degrees of freedom. Such regions of space we call fireball.

The internal structure of the formed fireball could have two scenarios:

It could consist of individual hadrons with short range correlations between the constituent quarks. The nuclear collision reaction therefore is governed by interactions between individual hadrons and hadronic resonances.

Or it could contain some of the quark-gluon plasma phase, where short range color confinement is broken and in which quarks and gluons roam over several fermi. This is the form of matter that QCD predicts could be created given the right conditions.

The latter scenario is the one we are looking for in order to confirm the theory of QCD, but it has to be unambiguisely distinguished from the first scenario (hadron gas). The major differences between these two phases of matter is that confinement does not occur and numerous highly excited gluons exist in the QGP phase. Gluons are very efficient in generating strange quark-antiquark pairs in quark-gluon plasma. This could result in an anomalously high strange particle abundance which will practically saturate the available strange quark phase space. Since gluons carry the (confined) charge of strong interactions, color, their detection in an experiment can only be indirect. Strangeness abundance provides a unique probe for QGP formation.

2.1 Why Strangeness

We will see later that cascade models show the hadron gas phase could also produce more strangeness as the hadron density of the fireball increases, and it has explained some of the early experimental data. So the problem is to find a signal that is unexplainable by conventional cascade models.

The following factors contribute to the general enhancement of direct strange particle production and the enhancement of strange antibaryons in nuclear collisions involving formation of QGP.

2.1.1 Pauli Blocking Effect

In general, gluons produce light quarks more copiously than strange quarks which have a heavier mass. In a Quark Gluon Plasma, when the fermi sea of light quarks reaches a certain level, creating a pair of light quarks takes as much energy as creating a pair of strange quarks. After that, with an even higher density and temperature, strange quarks and light quarks will be created approximately equally (see Figure[2.1][22]). This increased strange quark production will cause enhanced strangeness with respect to a system of confined hadrons(Hadron Gas) at the same temperature.

As our experimental results confirmed[2,3], the spectra of particles produced in relativistic heavy-ion collisions show the features of the so called fireball, a space-time region containing many particles with small collision length(Mean Free Path), which can be described in terms of thermodynamic variables such as temperature that determines the energy available for strangeness production. Since our experiments measure temperatures of 200±50 MeV, it is easier to create $s\bar{s}$ pairs in QGP fireballs at this temperature than in a Hadron Gas at the same temperature where strange hadrons remain more suppressed.

2.1.2 Higher Strangeness Production Rates

The strangeness production time constant in the QGP is of the order of 10^{-23} s [1], while in a Hadron Gas(HG) it is 10 to 30 times slower[1] at the same temperature and baryochemical potential. An estimation of the timescale for the creation and decay of a fireball would be the time needed for a beam of light to travel a distance of 15 fm(approximately the size of a fireball), that will be about $\approx 5 \times 10^{-23}$ s. We expect the strangeness in a QGP to reach thermal equilibrium during this timescale,

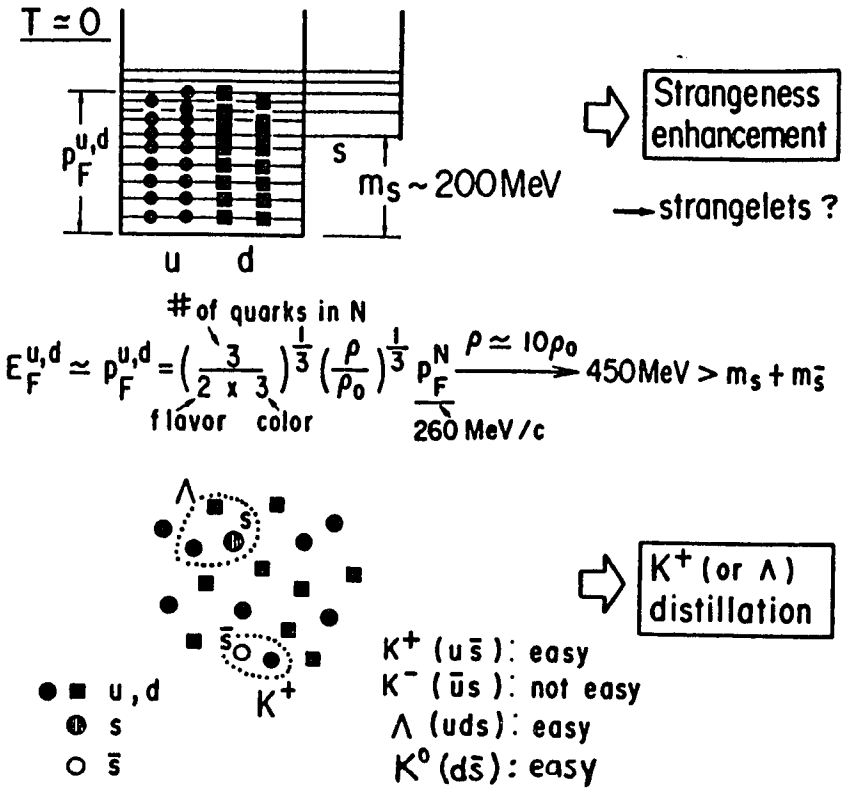

Figure[2.1][22] Fermi levels for different quarks. Proposed mechanism of strangeness enhancement and that of K^+ (or Λ or K^0) distillation for high-density quark matter.

but not in a thermal hadron gas phase. In a QGP, free quarks are available to annihilate and create strange quark pairs as $q\bar{q} \rightarrow s\bar{s}$. This reaction has large cross section because of the large degree of color freedom and high energy each individual quark has. While in a hadron gas phase, the same reaction has to be involved in a direct hadron collision as shown in Figure[2.2] , where all quarks are confined.

2.1.3 High Density of Strangeness in QGP

It was shown in Ref. 4 that an enhanced strangeness in QGP may be diluted by the geometry of the ensemble of collisions, and the production of single strangeness particles in QGP may not be distinguishably higher than that in HG if we assumed a large HG fireball and short formation time. However, the strangeness density is much higher in a QGP than in an HG; consequently multistrange baryons can be created more abundantly by hadronization of the strangeness-rich QGP than directly in hadron-hadron collisions, where they are predominantly made in several successive collisions. On the other hand, during the QGP (Quark Gluon Plasma) phase transition into a HG (Hadron Gas) phase, Ref. 5 demonstrates that a large antistrangeness content will build up in the HG phase while a large strangeness excess will be left in the QGP phase. This excess during hadronization could favor multi-strange hyperon production as well as strangelet formation. An enhancement of multistrange particles over HG-predicted values(by generally known cascade models) should therefore be seen as a signal of the presence of QGP.

2.1.4 The Role of Gluons in QGP

While the QGP and the HG differ in many ways, the crucial distinction between the two phases, as far as strangeness signal is concerned, is the large amount of

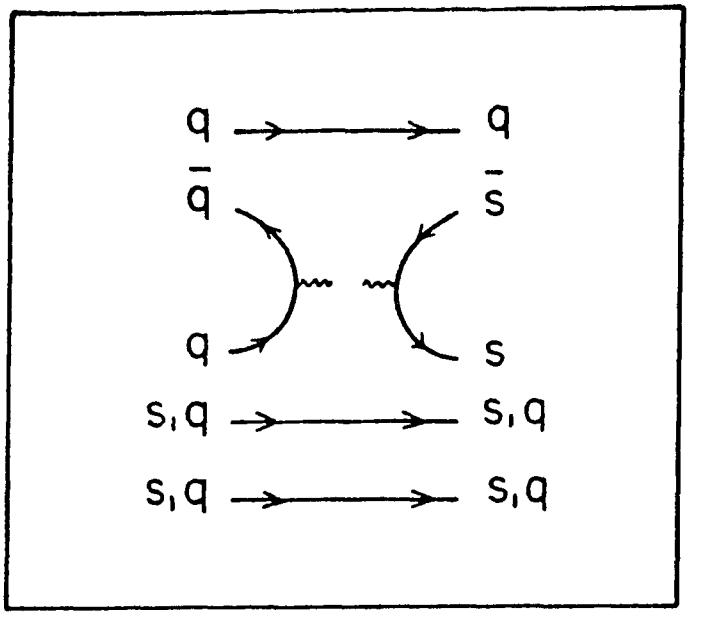

Figure[2.2] A pair of strange quarks created via annihilation of a pair of light quarks in a direct hadron collision.

gluons present in the QGP: it affects both production of $s\bar{s}$ pairs and hadronization at the end of the QGP lifetime.

The enhanced production rate of $s\bar{s}$ pairs relies heavily on gluon-induced processes and therefore on the abundance of gluons. Softer gluon-induced processes in hadron gas have a low cross section for producing $s\bar{s}$ pairs(gluons are all attached to quarks and have lower energy, no free gluons exist). And $s\bar{s}$ pair production in hadron gas is constrained by space and time, it can only be produced when there is collision(No process like $gg \rightarrow s\bar{s}$).

It was argued in Ref. 1 on the basis of perturbative QCD that the $gg \rightarrow gg$ scattering process has a large cross section due to the large number of color degrees of freedom resulting in a short mean free path for gluons. The same argument holds that gluons are very efficient in creating $s\bar{s}$ pairs directly($gg \rightarrow s\bar{s}$) in Quark Gluon Plasma phase where high energy free gluons are abundant(they carry much of the system's total energy[1]).

Gluons also play a major role in the dynamics of the QGP-HG phase transition: they carry much of the QGP entropy which forces the gluons to fragment into quarks.

2.1.5 Stopping Power For Heavy Ions at the AGS

E810 experiment's measurement of rapidity (defined as $y = 0.5ln(\frac{E+P_L}{E-P_L})$) distributions of charged particles affirmed that there is no anomalously high nuclear transparency[6] in relativistic heavy ion collisions with 14.6 $\times$ A GeV/c Si beam at the AGS. This actually means that nearly full baryon stopping has been achieved at the AGS energy. A significant amount of baryon stopping will result in a baryon rich fireball with maximum energy deposition. It will help the fireball formation with nearly the highest temperature and baryon density possible at the AGS energy.

The temperature measured at AGS is about $\approx 200 \pm 50 MeV$ which is comparable to the temperature measured at higher energy(200 GeV) in CERN experiments where much higher transverse energy was observed. We will see later that concerning strangeness (except antistrangeness) enhancement, heavy ion collisions at the AGS energy (baryon rich environment) give similar results as those at CERN energy. This tells us that heavy ion collision experiments at the AGS may not have much disadvantage compared to those same kind of experiments at CERN.

2.1.6 MPS TPC With Wide Rapidity Coverage

As will be discussed in detail in the next chapter, experiment E810 utilized 14.6 $\times$ A GeV/c Si beam at the AGS and the MPS facility where a large magnetic field of 5-10 kilogauss and 3 TPC(Time Projection Chamber) modules are the main parts of the experiment.

E810 was designed to cover a large rapidity range and record as much information as possible on an event by event basis. The detector covered the forward hemisphere in the center-of-mass of the nucleon-nucleon system. In a symmetric situation, such as $Si+Si$ collision, a 2π coverage is equivalent to a 4π solid angle coverage by reflection. Since each charged track was recorded individually, virtually everything has been recorded on tape for later analysis. This experimental arrangement gives us the unique opportunity to study in heavy ion collisions the production and decay of strange hyperons whose decay lengths correspond to our measurement range.

2.2 Previous Data on Strangeness Production

There were relevant reports on hadron collision experiments in the 70's. Blobel *et al* reported[8] production rates of different hadrons from *pp* collision at 12 to 24 GeV/c, including single strangeness hyperons (Λ and Σ's). It was initially proposed that for heavy ion collisions the hadron production rate could be calculated as a superposition of nucleon-nucleon collisions. When heavy ion sources became available at AGS and CERN recently, it became clear that more sophisticated approaches were necessary.

2.2.1 K/π Ratio and the RQMD Model

The first round of AGS experiment E802 reported striking results of enhanced strangeness production in heavy ion collisions with respect to the naive superposition of NN collision results—consistent with what was expected from a quark gluon plasma scenario. As shown in Figure[2.3][9], while π production remains more or less the same, the gradual K^+ enhancement per projectile nucleon from p+Be to p+Au to central Si+Au is clearly seen. The K^- yield seems to stay the same from p+Be to p+Au, but from p+Au to central Si+Au an enhancement is seen which may imply the secondary production of kaons via $\pi\pi \rightarrow K^+K^-$ in the central Si+Au collisions.

Ref. 10 demonstrated that the observed enhancement of the K/π ratios can be understood without requiring the formation of a quark-gluon plasma (Figure[2.4][10]). In a relativistic-quantum-molecular-dynamics (RQMD) approach, the calculated pseudorapidity (defined as $\eta = 0.5ln(\frac{P_{total}+P_L}{P_{total}-P_L})$) distribution for central collisions

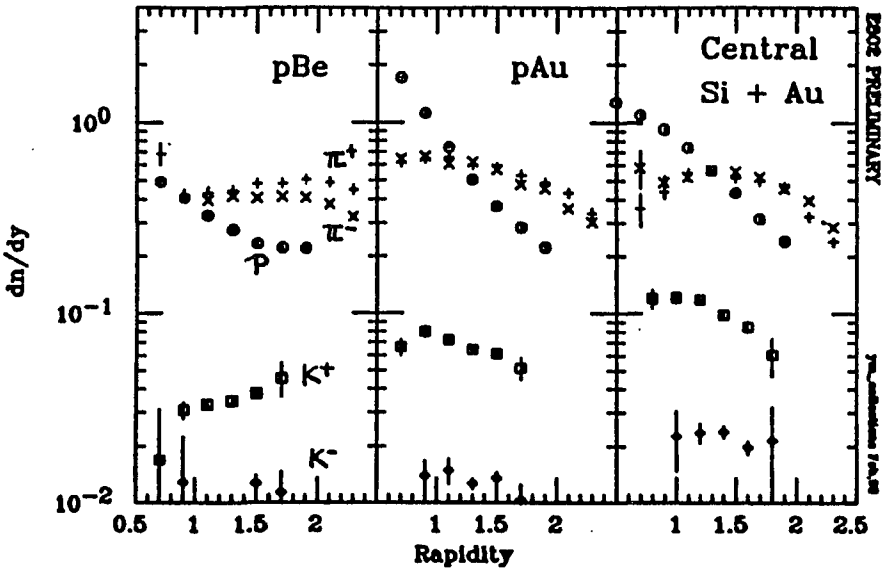

Figure[2.3][9] Rapidity distribution, dn/dy for $\pi^{\pm}$, $K^{\pm}$, and protons in p+Be, p+Au, and central Si+Au collisions. The central Si+Au data are plotted as $(\frac{dn}{dy})/28$.

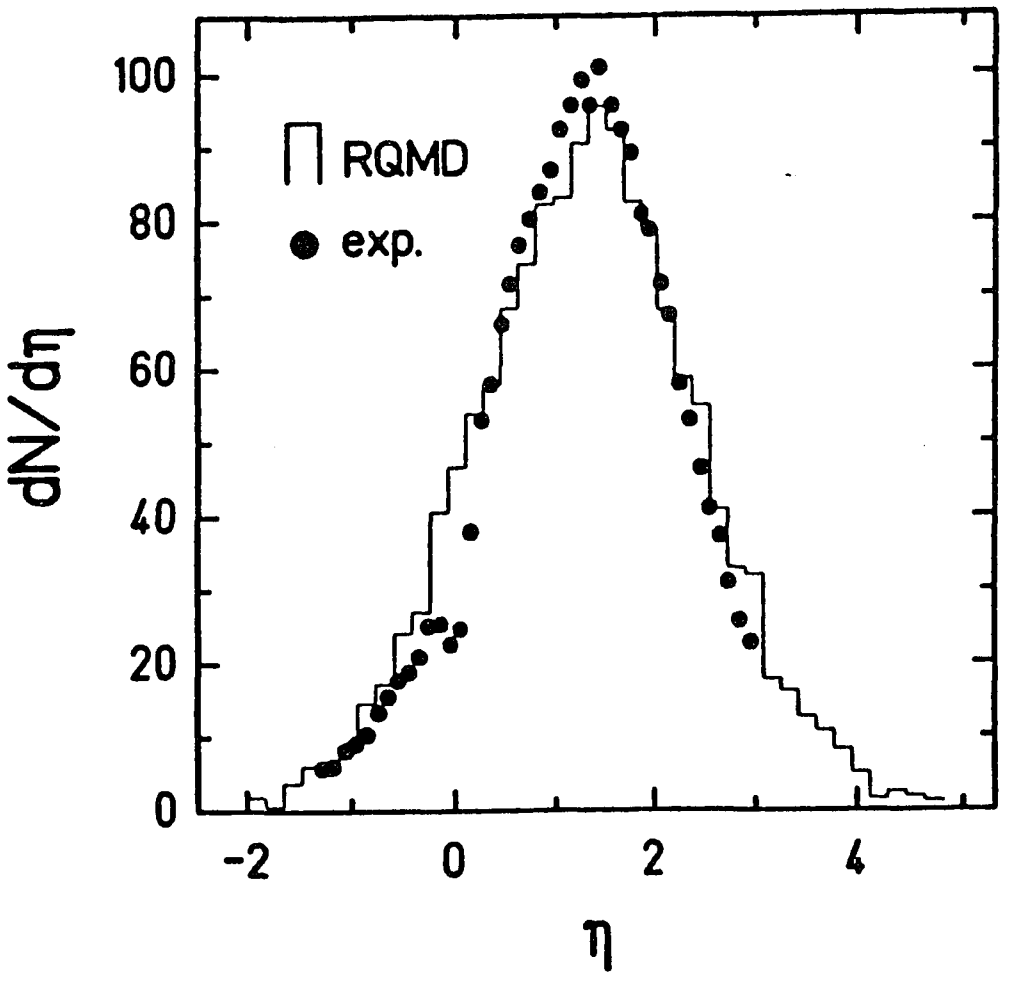

Figure[2.4][10] a). Charged-particle pseudorapidity distribution in Si(14.5A GeV) on Au: comparison between the RQMD results (histogram) at impact parameter $b = 1$ fm and the preliminary data from the E802 Collaboration[9] for central events. Pseudorapidity is defined as $\eta = 0.5ln(\frac{P_{total}+P_L}{P_{total}-P_L})$.

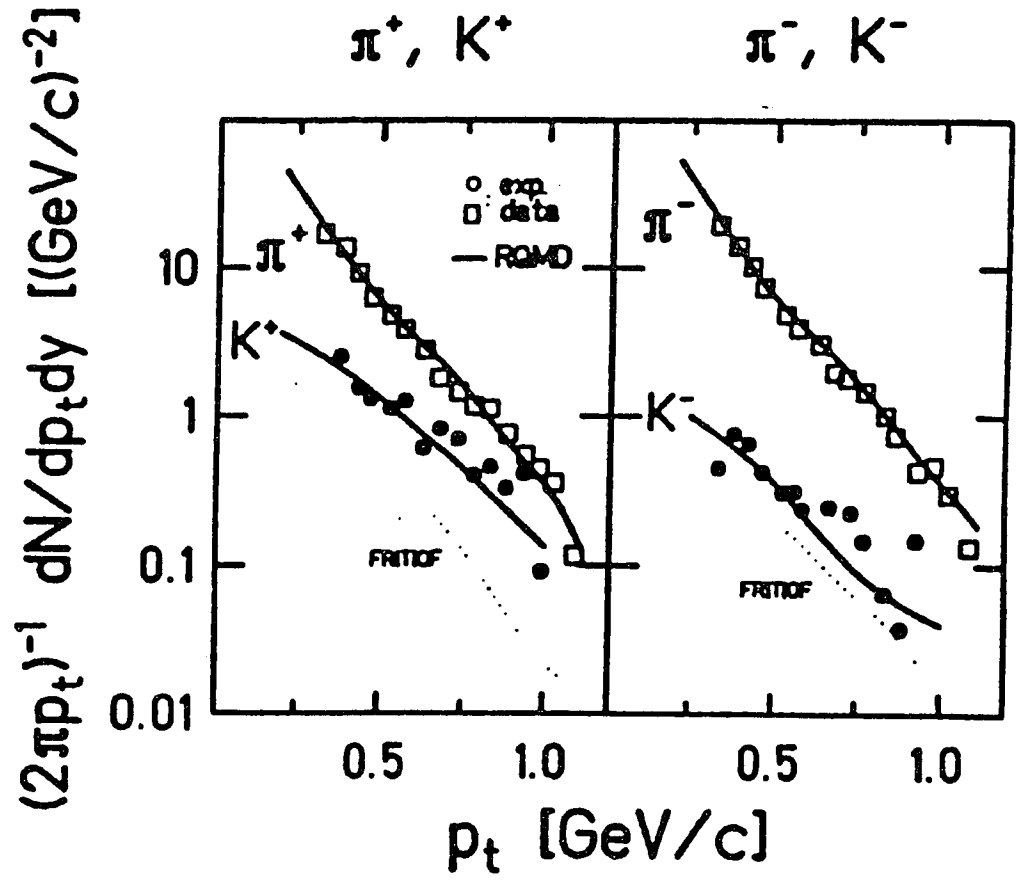

Figure[2.4][10] b). Transverse-momentum spectra of π^+, K^+ (left-hand side) and π^-, K^- (right-hand side). The preliminary data from E802 Collaboration[9] for the rapidity interval $1.2 < y_{lab} < 1.5$ are given by the open squares ($\pi^{\pm}$) and filled dots ($K^{\pm}$). The solid lines represent the RQMD results ($1.0 < y_{lab} < 1.5$) and the dotted lines the FRITIOF results. Absolute normalization of the cross section is to the π^+ spectra at $p_t = 300$ MeV/c.

indicated a large degree of nuclear stopping and thermalization. However, nonequilibrium effects play an important role in leading to the strong enhancement of the total kaon production cross section. RQMD studied the kaon production without the simplifying assumptions of thermal equilibrium or independent fragmentation. Instead, it follows the time evolution of all hadrons—initially present and especially subsequently created that is responsible for most of the kaons produced via secondary scattering (meson baryon and meson meson collision).

2.2.2 K_s^0, Λ Production and Models (ARC and AGSHIJET+N*)

E810 also reported[2] a significantly enhanced K_s^0 and Λ production in heavy ion collisions with Si beam at the AGS energy. In Figure[2.5] and Figure[2.6] we have plotted the rapidity distributions of K_s^0's and Λ's from the Si target. The curves shown in the figures are the predictions of several models. Also shown in the figures are the measured rapidity distributions for $p + p \rightarrow K_s^0 + X$ or $\Lambda + X$ at 12 GeV/c scaled up by a factor of 28. In the Si data, E810 only measured the forward rapidities, but reflected about $y = 1.7$ (corresponds to $\sim y = 0$ in the nucleon–nucleon CMS) because of the symmetry of the reaction.

The first thing to be noted is that our Si data can not be described by the naive assumption that we can scale up the pp cross section by 28. Nuclear rescattering needs to be invoked in order to try to explain the excess cross section for K_s^0 and Λ production.

Similarly, both ARC (a relativistic cascade) and AGSHIJET+N* (a modified heavy ion jet) models reproduced the E810 Si data fairly well. We can see that AGSHIJET+N* underpredicted both K_s^0 and Λ, especially for Λ, it underproduced

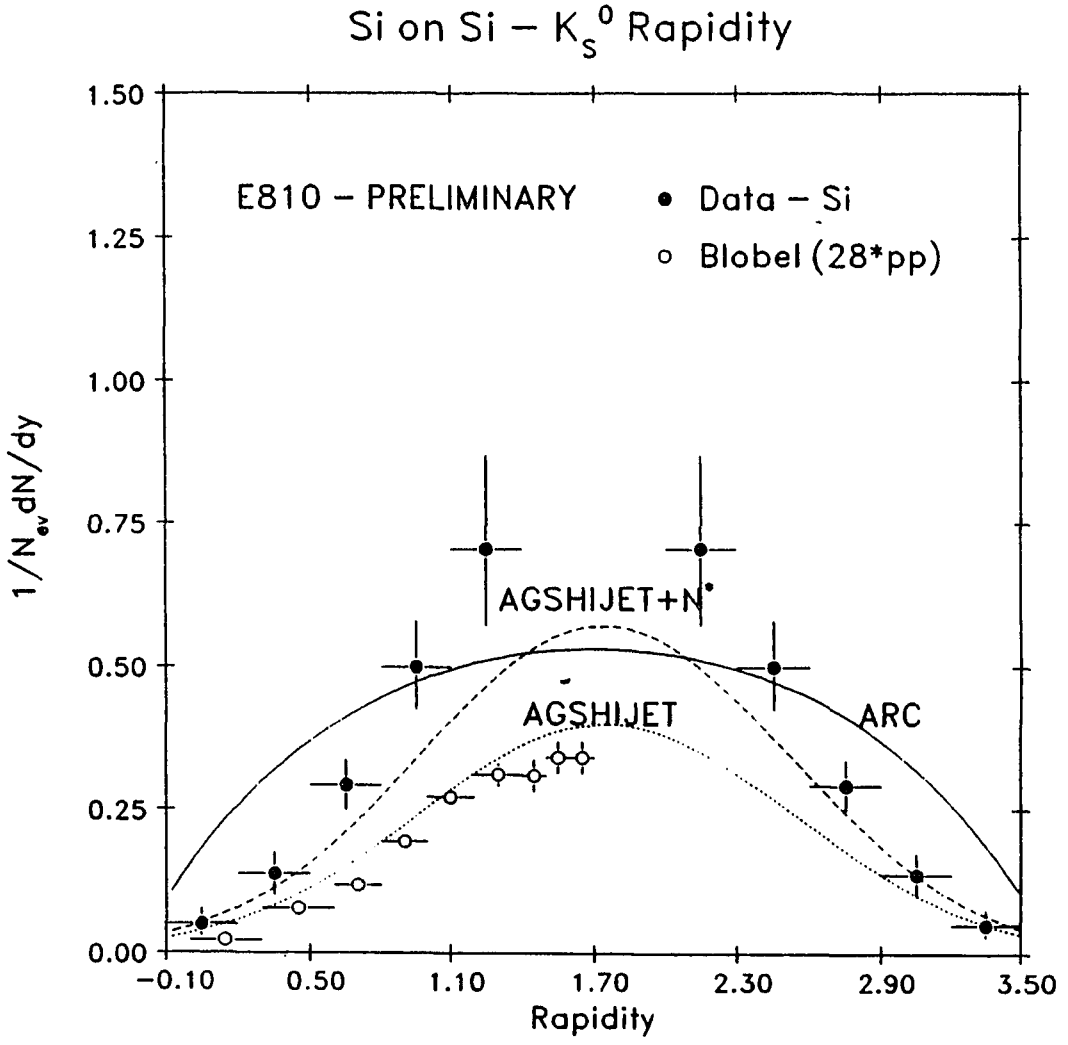

Figure[2.5] Rapidity distribution for K_s^0's from the *Si* target. The solid points above a rapidity of 1.7 are our measurements. Errors shown are statistical only. The solid points below rapidity of 1.7 are our measurements reflected about 1.7 . The open circles represent the measurements of Ref.8 scaled up by 28. The solid curve is the prediction of the ARC model.

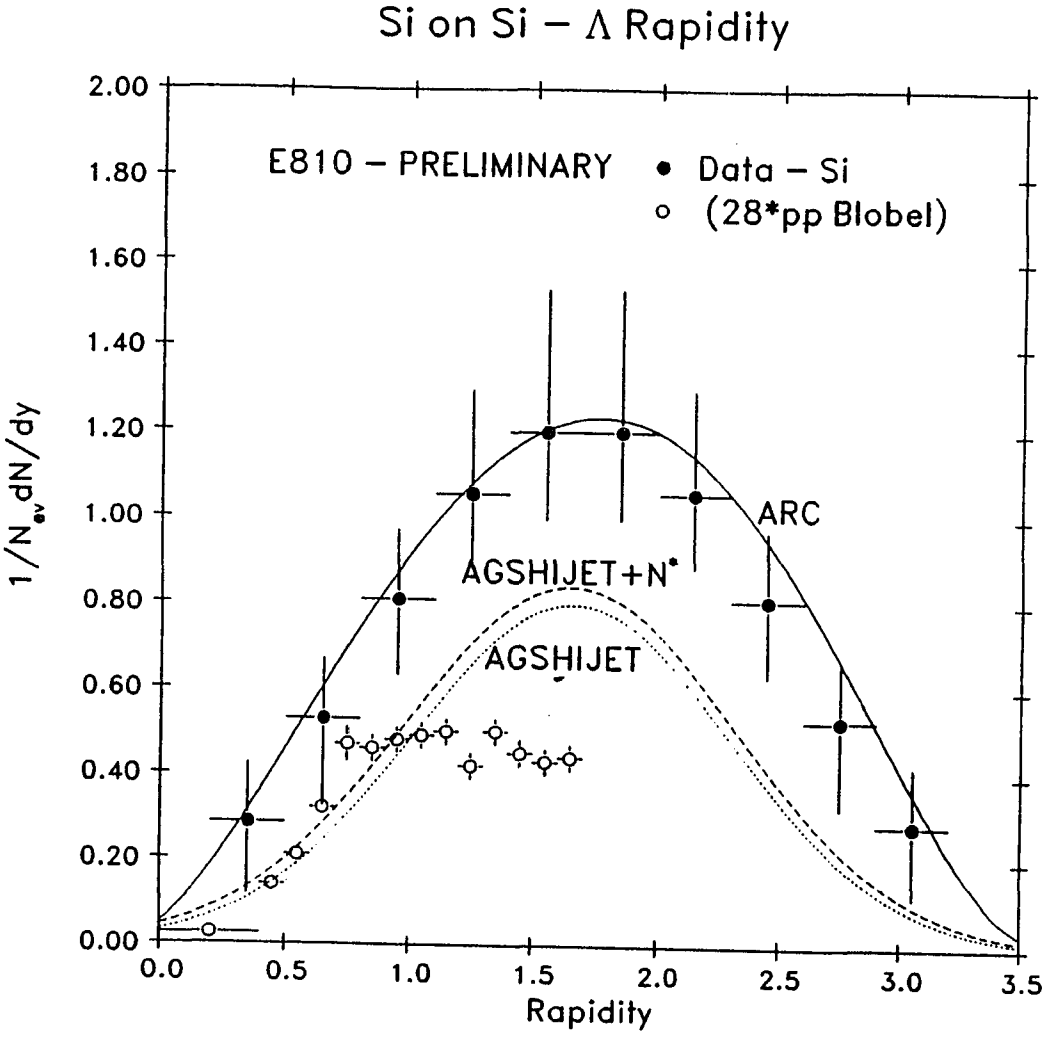

Figure[2.6] Rapidity distribution for Λ's from the *Si* target. The solid points above a rapidity of 1.7 are our measurements. Errors shown are statistical only. The solid points below rapidity of 1.7 are our measurements reflected about 1.7 . The open circles represent the measurements of Ref.8 scaled up by 28. The solid curve is the prediction of the ARC model.

Λ by a factor of 2. While ARC did extremely well in the Λ case, it gives a much wider rapidity distribution for K_s^0 than we observed although the total yield is about right. The good news is obvious, both these two models give predictions far greater than a naive scale up of *pp* data. We'll see in later chapters that both models did very well with the *Pb* target data.

Since both models don't invoke the QGP scenario and explain the data to a reasonable degree, no QGP is necessary in order to explain the current heavy ion data for single strangeness productions.

Both of these models employed the rescattering of resonant states such as Δ and N* as a major source of strangeness production.

In AGSHIJET+N*, when nucleons interact at a few GeV energies they become excited into N*'s which decay into ΛK about 2.5% of the time, and the N^*'s are also allowed to propagate to the next collision. This procedure does not increase the number of N*'s, but does create more higher energy collisions, thus increasing the number of K pairs produced.

In the ARC model, N*'s are not included in the dynamics. Instead, production of strangeness occurs in direct channels, both for associated and pair production. The increased amount of strangeness in baryon–baryon channels is due to rescattering of Δ's which have higher collision energy than if they had decayed to a proton and pion and then rescattered. Strangeness production also occurs in πN and $\pi\pi$ rescattering. Resonances continue to scatter until they decay.

Chapter 3

Experimental Apparatus:

A TPC (time projection chamber) system has been built for the BNL experiment 810, which is a study of particle production in relativistic heavy ion collisions. The events of interest have very high multiplicity (>100 tracks). TPCs were chosen as the tracking detectors because they measure true three-dimensional points along the tracks, a very significant advantage for track reconstruction.

The E810 experiment used the 14.6 $\times$ A GeV/c *Si* beam provided by the AGS(Alternating Gradient Synchrotron) in BNL (Brookhaven National Laboratory) to bombard various targets (Al, Si, W, Pb, Au etc). The particles produced passed through our main detector (the three TPC modules) placed in the strong magnetic field(5 kilogauss) of MPS magnet. The trajectories are curved by the magnetic field. The TPC modules record every track that passes through by the hits it caused in the TPC. A pattern recognition program does the tracking later by connecting the hits that belong to the same track. The momentum of each charged track is calculated from its curvature.

3.1 The MPS Magnet

The MPS magnet is a very large magnet which was previously used for elementary particle experiments. The field volume between the poles is 4.60 meters long $\times$ 1.80 meters wide $\times$ 1.20 meters high, the maximum magnetic field is 10 kilogauss and the weight of the magnet is 700 tons. Two megawatts of electric power are needed to generate the field. The magnet rests on hydraulic pads which allow a 30°

rotation about a pivot near the forward end.

The large field volume permits experimenters to place detectors in the field and near the target, thereby enhancing the probability that most of the products of an interaction will be detected. Event reconstruction via high speed computers is an essential part of understanding the phenomena taking place.

3.2 The TPC Modules

The TPC system consists of three separate modules with a spare which improves the system's useable time. Readout electronics uses custom hybrids to produce a very compact, cost–effective system. In order to maximize the acceptance the ion beam is incident on the middle of the chamber, which limits the maximum useful ion beam.

The front view of a module is shown in Figure[3.1]. In the vertical drift region(the TPC is 60cm high $\times$65cm wide $\times$47 cm long) a field cage with double-sided printed circuit boards on the sides and a double row of wire electrodes at each end shapes the electric field. The TPC operates under an electric field of 330 V/cm in the drift region. The read out is achieved by 36 rows(12/module spaced 3.8cm apart) of 256 short anode wires(2.54mm spacing), with the wire number giving the (x, z) coordinates and the drift time giving the y coordinate for unambiguous 3D points along the tracks. Figure[3.2] is an overview of the three TPC modules in the center of the MPS magnet (looking downstream). Figure[3.3] is a close look at the three TPC modules with electronic readout cables on one side. Electrons produced by charged particles in the drift region must pass through a gating grid and a wire cathode in order to reach the anode. A second, solid copper, cathode below the anodes helps to achieve high gain. The arrangement is shown in Figure[3.4].

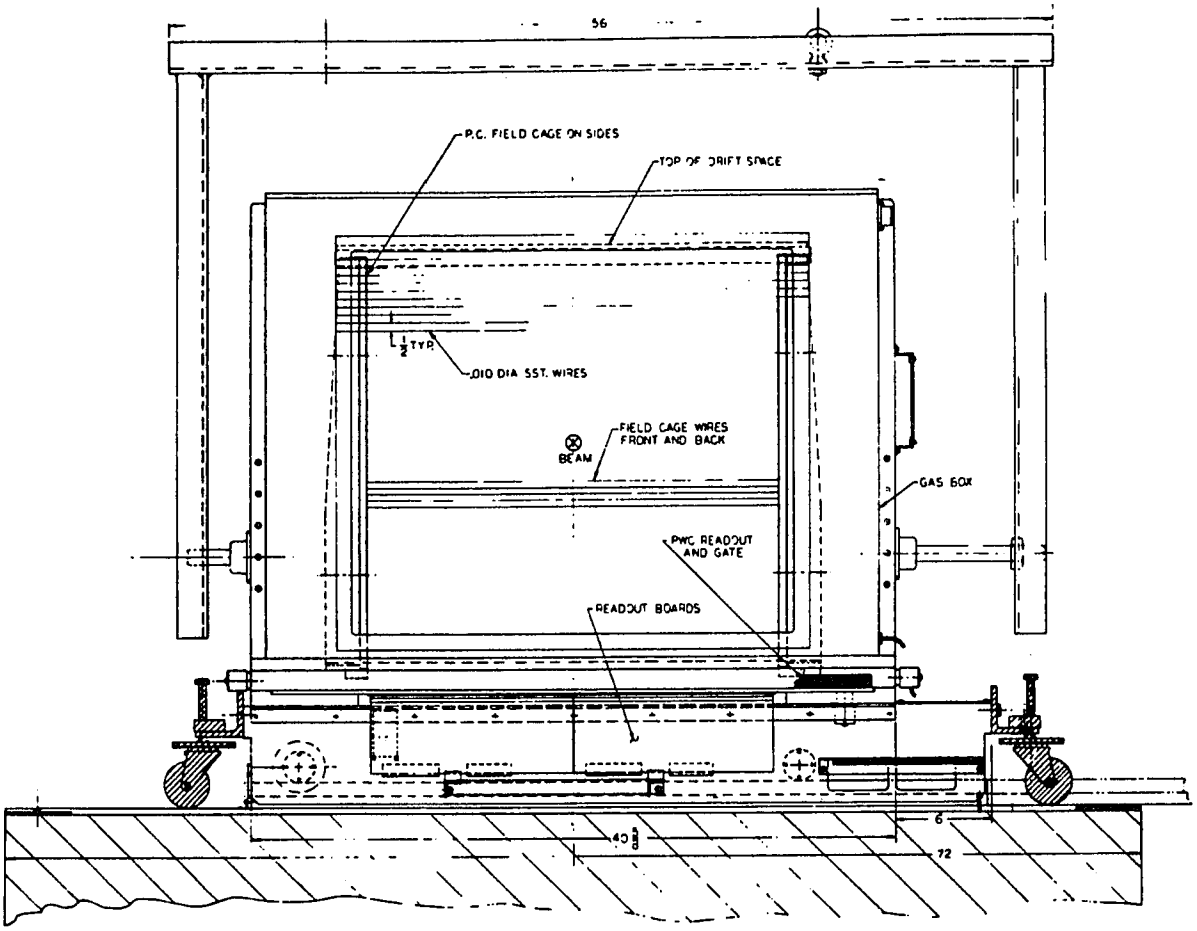

Figure[3.1] Front view of a TPC module showing principle components.

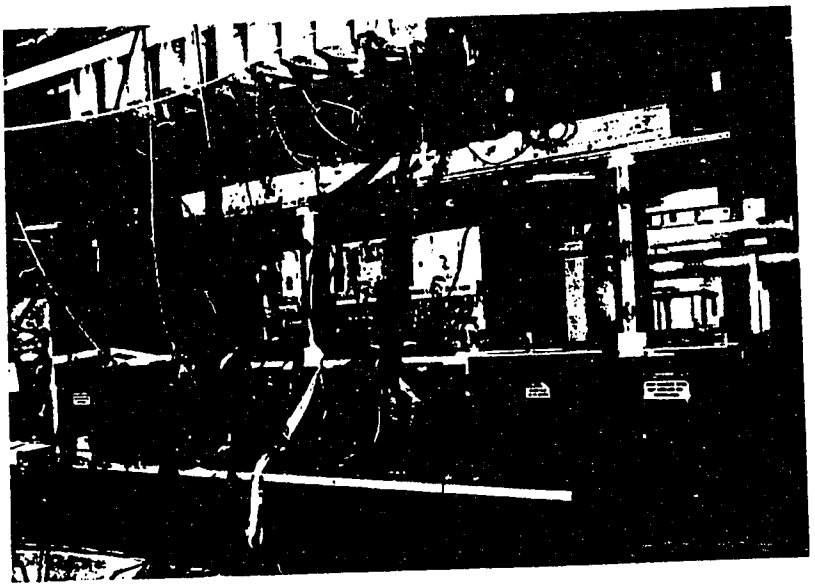

Figure[3.2] An overview of the three TPC modules in operating position as viewed from the upstream end of the MPS magnet(looking downstream).

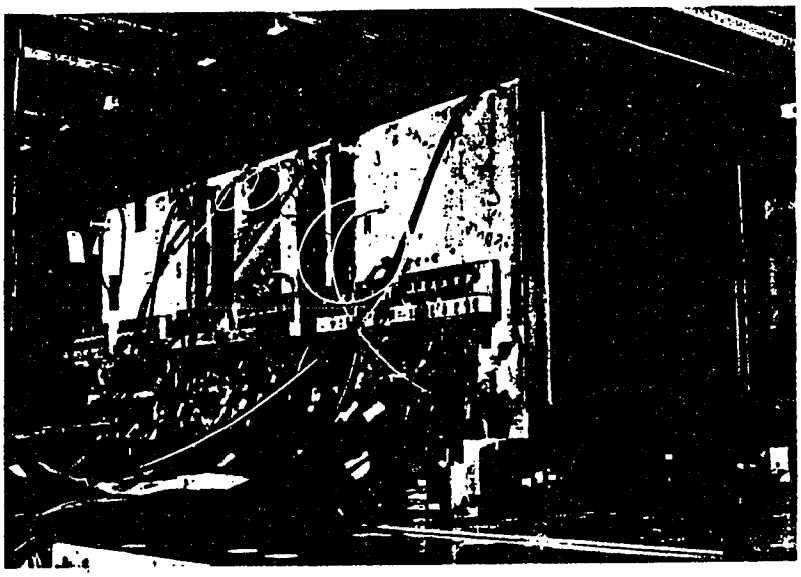

Figure[3.3] A closeup look at the three TPC modules with electronic readout cables connected on one side.

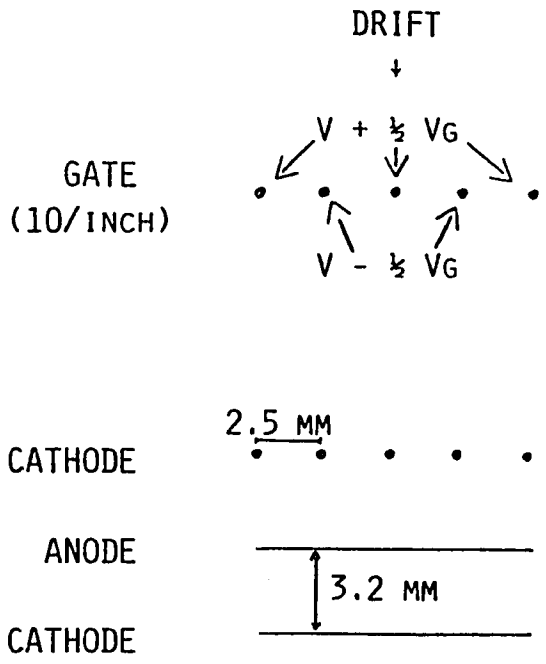

Figure[3.4] Schematic of the arrangement of the electrodes in the detector end cap.

In TPCs the maximum beam rate is limited by field distortion due to positive ion buildup in the drift region. A major source of positive ions are ions produced in the gas amplification process at the readout anodes that leak into the drift volume. A gating grid is used to prevent the transfer of drifting electrons from the drift region to the detector region and that of positive ions in the reverse direction except for selected events. Gating is achieved by applying different potentials to adjacent wires as indicated in Figure[3.4], collecting the electrons on the more positive wires. When the trigger system indicates that an event of interest has occurred the gate wires are shorted together for 30μs, a little longer than the maximum drift time (the drift velocity of e^- is 2.3 cm/μs), allowing ionization from the tracks to reach the amplification region. Because of their slower drift velocity, positive ions from amplification at the anode do not reach the gating grid before the gate is closed, further improving the gating of the TPC.

3.3 The Electronics

Since dE/dx is not measured in this system the electronics is only required to give time information. In order to read out the many closely spaced short anodes at minimum cost, a circuit was designed that allows each individual channel to be mounted directly on the chamber and to occupy only the anode wire spacing. The circuit for each channel is shown in Figure[3.5]. Sixteen channels are assembled in a hybrid package (LeCroy HTD 161S,M.) with inputs spaced 2.54 mm apart. Shaping–time constants were selected to match the anode waveform. An integration time constant of 50 ns and a differentiation time constant of 200 ns were chosen to minimize noise and maximize two-track separation. Time information is recorded with a memory driven by a counter to serve the function of a shift register. Each hybrid contains memory capable of recording 1024 time samples from each channel.

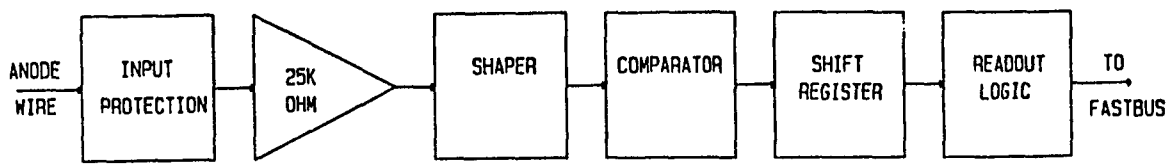

Figure[3.5] Schematic of individual channel electronics.

To reduce possible local noise pickup, all logic levels are ECL (Emitter Control Logic to quickly release the charges accumulated in the base). The clock and address lines are terminated differential ECL.

To minimize the control circuitry two kinds of hybrids are used. One type is called a master and in addition to the amplifier–shaper–comparator and memory for 16 channels has the counter used to address the memory plus the control logic necessary to read out itself plus seven slave hybrids. The slave hybrids contain only the amplifier–shaper–comparator and memory required for 16 channels. The printed circuit boards are assembled with one master and seven slaves (Figure[3.6]) which is sufficient for 128 anode readouts and is externally accessed by one clock line, one data line and 14 control lines. The data line is common to the two hybrid cards in a row and the other lines are common to the whole TPC. Thus only 27 line are used to connect over 3072 channels per module to the external electronics. The time samples are obtained at 50 MHz and the data is sequentially read from each channel's memory at 25 MHz. This serial string of data bits is encoded into wire number, drift time and cluster size by FASTBUS modules in which all rows are encoded simultaneously. Consequently the entire readout is completed in 10 ms (dead time). This amount of dead time is acceptable because of other limitations on trigger rate.

The on-chamber performance of the hybrid allows input sensitivity of less than 1 μA. Thus the chamber gas gain can be as little as a few 10^4.

3.4 The Gas System

In order to have good event reconstruction in these high–multiplicity events it is important to optimize the two–track resolution by having a large number of independent readout elements. We have used rows of short ($\sim$ 1 cm) anode wires

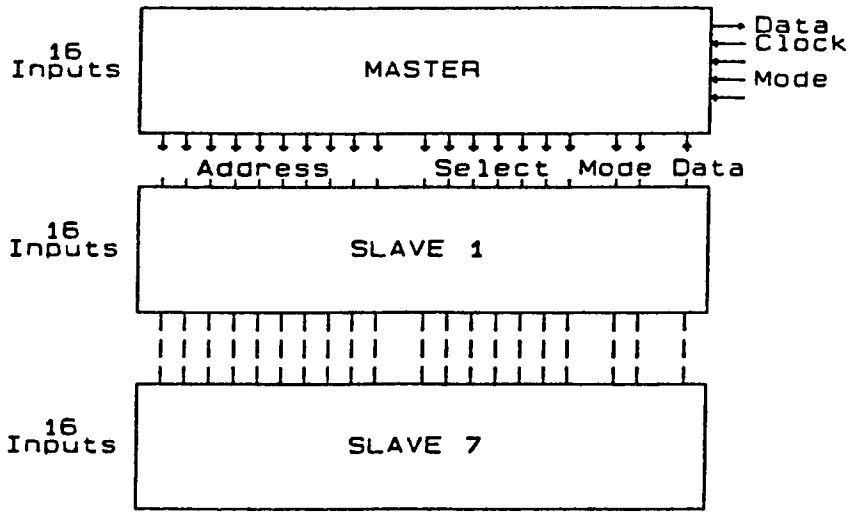

Figure[3.6] The Layout of a 128-channel hybrid printed circuit boards (one master and seven slaves).

parallel to the beam direction. On the other hand, use of the short anode wires precludes using dE/dx for particle identification, which in the kinematic region of interest and at the particle densities in these events is a very expensive and extremely difficult task, and probably would have limited effectiveness.

It is also essential that the gas used in the chambers be chosen to give stable operation, safety and long chamber life. Various gas mixtures have been studied for this purpose. We chose a mixture of a low–diffusion gas † (79% argon, 16% isobutane and 5% dimethoxymethane) known to be stable at high gain in order to achieve this fine segmentation.

Tests made on these gases give good efficiency characteristics and linearity of drift time .vs. drift distance. In addition, this gas mixture has the further advantage of not being able to sustain combustion by itself — a very important consideration for a system this large. However, the high argon content will result in a high rate of multiple scattering.

3.5 The *Si* Beam

E810 experiment utilized the 14.6 ×A GeV/c *Si* beam provided by the AGS as shown in Figure[3.7]. *Si* ions are prepared by Tandem Van De Graaff Heavy Ion Source and accelerated through the Heavy Ion Transfer Line(HITL) before being injected into AGS. The *Si* ion beam is transported to the experimental area after it was accelerated to the momentum of 14.6 ×A GeV/c. The beam intensity used is ~5000 *Si* ions per second.

---

† Considerable experience was gained with this gas in the MPSII drift chamber system used for high energy physics experiments.

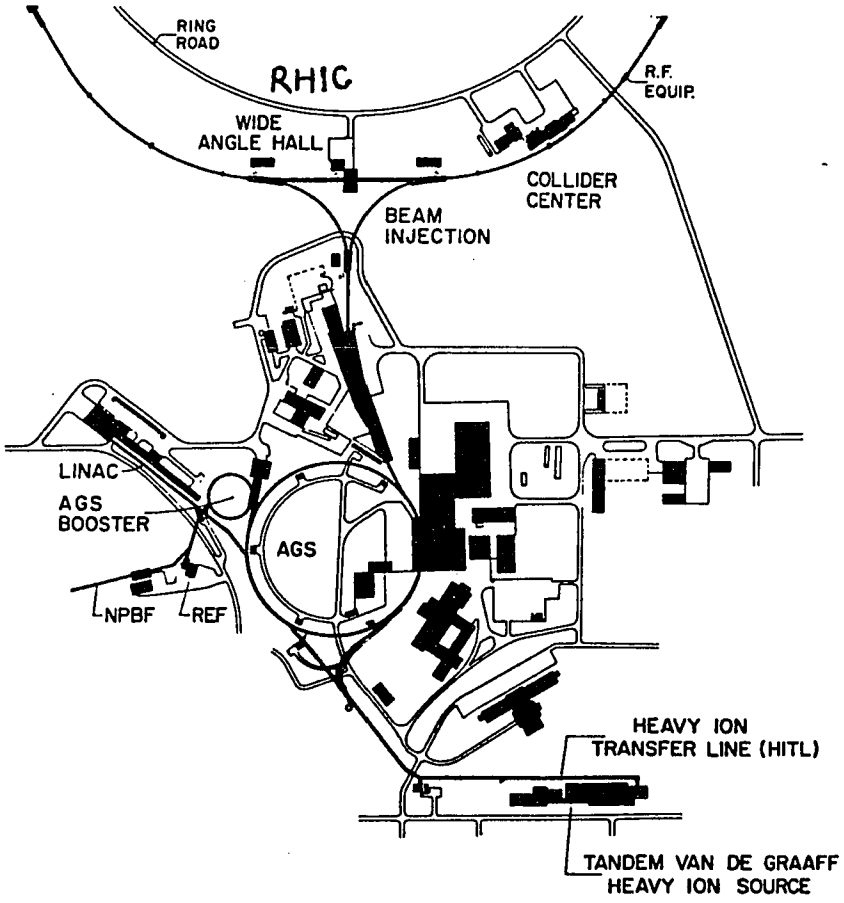

Figure[3.7] The AGS complex.

3.6 The Trigger

A plan view of the E810 apparatus is shown in Figure[3.8]. A *Si* beam at 14.6 $\times$A GeV/c is incident on a target just upstream of a set of three TPC modules. *Si* beam is identified by a plastic Čerenkov counter upstream of the target (the particle momentum is known, Čerenkov counter finds out the velocity, so the mass can be known). The beam passes through the middle of the TPC's, which are used to reconstruct the angles and momenta of charged particles produced in the forward hemisphere of NN center of mass system(0 to 20° Lab). The main trigger element is a scintillation counter(S9) in the beam downstream of the MPS magnet, which is used to reject events in which fragments with Z>6 remain in the beam region (the pulse height in a scintillation counter is proportional to the energy deposited $dE/dx \sim Z^2$). The pulse height in the veto counter is recorded for every event so that tighter cuts can be applied by software. Two counters just upstream of the TPC, slightly above and below the beam are used to select interactions from the region of the target. Multiplicities of reconstructed tracks often exceed 100, with an estimated reconstruction efficiency >90% for long tracks. There are no dE/dX measurements in the TPC.

3.7 The data acquisition(DAQ) system

The data-acquisition system used in the MPS is a FASTBUS based system which reads out CAMAC based devices as well by the use of a FASTBUS branch driver (STRUCK 320 module). The host computer is a VAX-750 and it is interfaced to the FASTBUS by means of a computer interface module(STRUCK 300 module, CFI) to VAX UNIBUS.

As shown in Figure[3.9], data reading and formatting is done by the SLAC

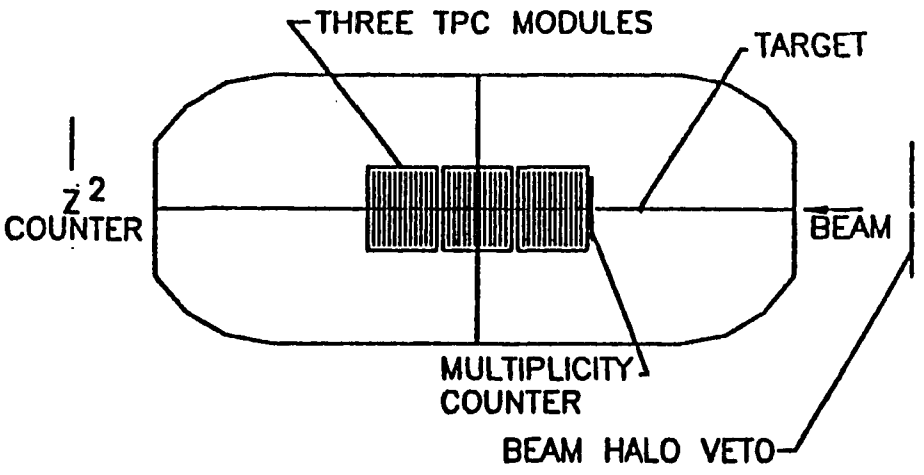

Figure[3.8] Plan view of E810 apparatus.

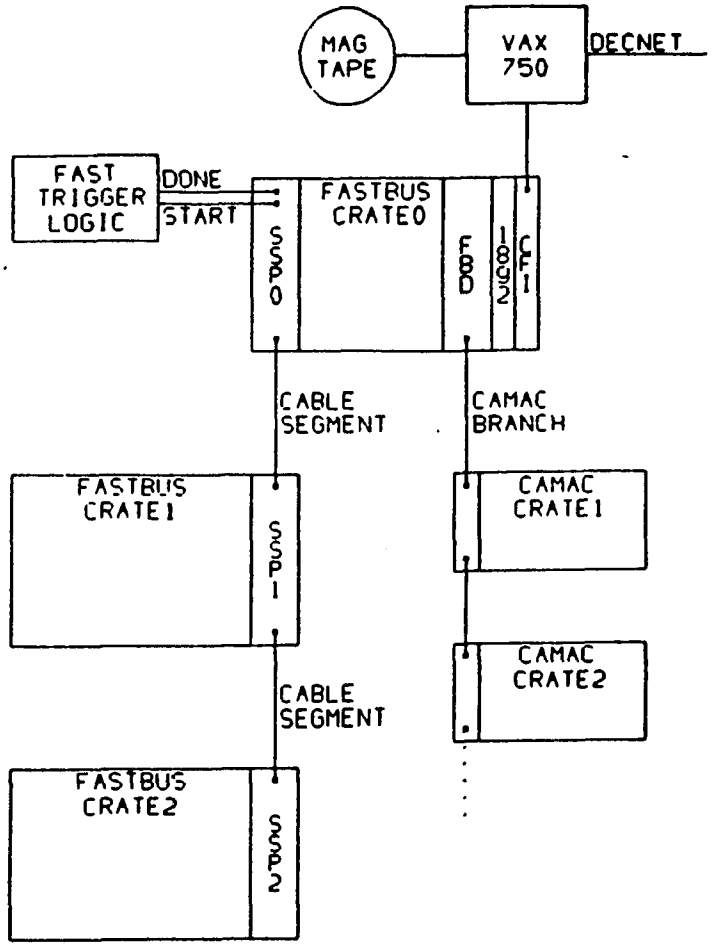

Figure[3.9] The MPS data-acquisition (DAQ) system hardware block diagram.

scanner processors(SSP's) resident in the FASTBUS system. A multiprocess software system on VAX computers is used to communicate with the SSP's, record the data, and monitor on-line the progress of high energy and heavy ion experiments.

Each spill of data is stored by SSP0 to the FASTBUS memory which is a LeCroy 1892 with 4 Mega bytes capability before being read written to magnetic tape by the host VAX. The magnetic tape used to record the data is 6250 bpi tape capable of 125 inches/second. The system has been timed to record $\approx$ 450 kilobytes/second within 2 seconds between spills (beam spill time 1 second, AGS cycle time 3 second).

3.8 The Track Reconstruction

A TPC track recognition program has been developed for the E810 experiment. The track reconstruction program consists of three parts: a local pattern recognition which associates contiguous readouts on adjacent readout wires to form a single hit, a subroutine which partitions the hits into slices in the yz-view (the vertical plane containing the beam and the vertical magnetic field) and the track reconstruction section.

From the alignment run (center beam track only, without magnetic field), the TPC could be calibrated to 100 μm, and the drift velocity to 1% (accuracy for v_d = 2.3 cm/μs). For regular tracks, the rms position resolution is: 0.9 mm–x, 0.75 mm–y, and sagitta error $\sim$ 0.32 mm.

The pattern recognition program separates 2 tracks at 2.5 mm in the x–direction, but merges hits at this distance (from 2 adjacent wires) if the signal in drift direction (y–direction) overlaps— this means: within a 5 mm $\times$ 5 mm area in the x-y plane, 50% of the time two tracks will be separated.

Multiplicities of reconstructed tracks often exceed 100, with an estimated reconstruction efficiency >90% for long tracks. Figure[3.10] is one of the reconstructed central events. For the final data sample, we selected only the most central events using a cut on the highest multiplicity of the negatively charged tracks within our region of good acceptance.

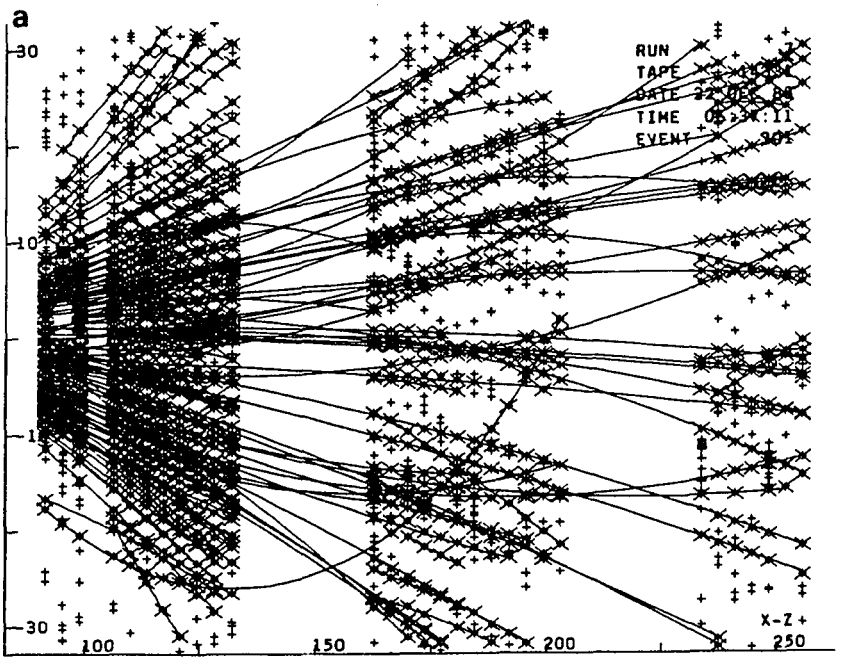

Figure[3.10] a). One of the reconstructed heavy ion collision events (view a: X-Z).

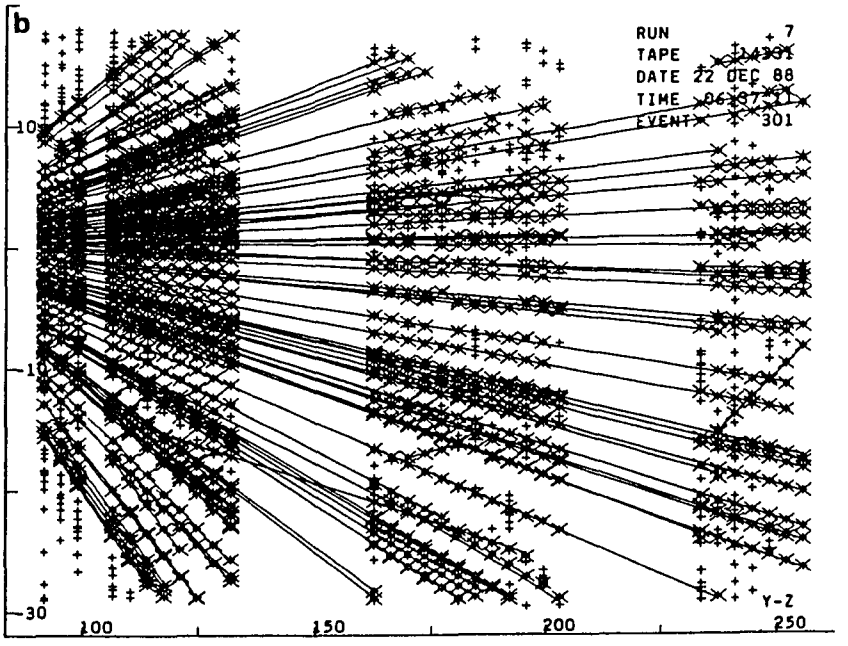

Figure[3.10] b). One of the reconstructed heavy ion collision events (view b: Y-Z).

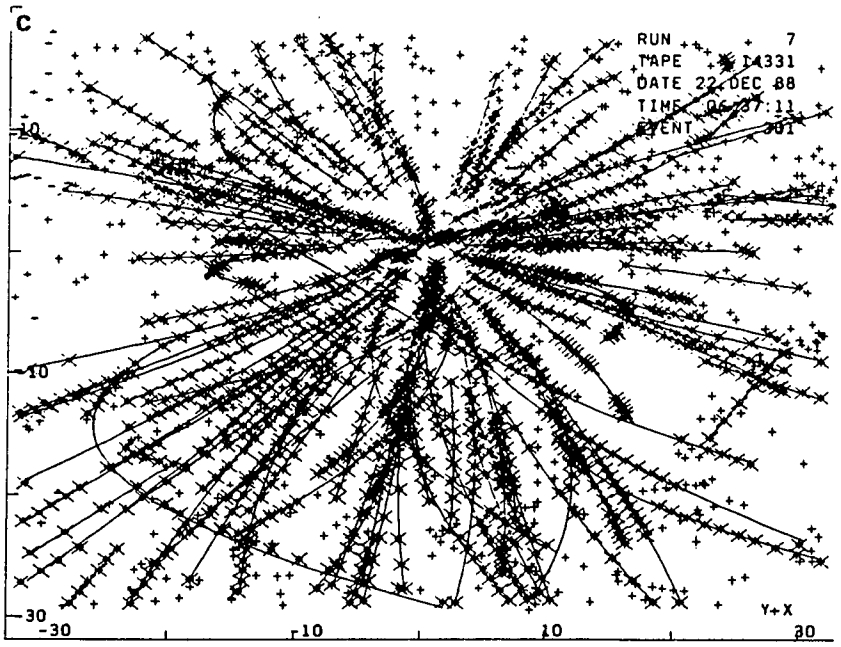

Figure[3.10] c). One of the reconstructed heavy ion collision events (view c: Y-X).

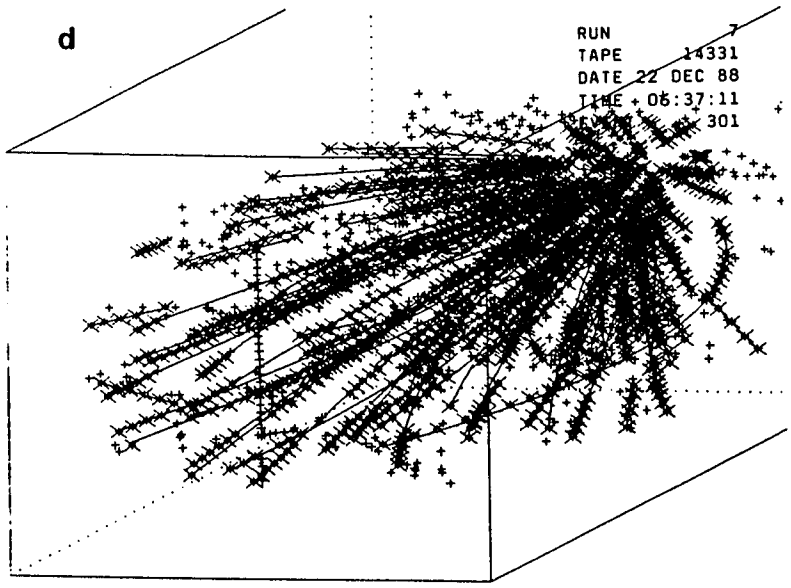

Figure[3.10] d). One of the reconstructed heavy ion collision events (view d: 3-dimension).

Chapter 4

The Experimental Procedure

The E810 was designed to cover a large rapidity† range, record as much information as possible and allow the data analysis to be done on an event by event basis.

We utilized the E810 data that we took in 1991 to study the yield of strangeness production in heavy ion collisions.

4.1 Experimental Method

The experiment used three TPC modules in a 5 kG magnetic field to measure charged particles in the forward hemisphere in the center-of-mass, or from 0° to 20° in the laboratory. The experimental arrangement is shown in Figure[4.1]. The incident silicon ions were identified by a plastic Čerenkov counter. The trigger was based on a scintillation counter 8 meters downstream of the target to veto on high Z fragments in the beam region and a pair of counters just behind the target slightly above and below the beam to select interactions from the target. This pair of counters was ~20 cm behind the target and ~2.5 cm above and below the ion beam line.

Events were recorded requiring signals in both counters behind the target and a veto counter trigger level corresponding to $Z \leq 6$ (the pulse height in a scintillation counter is proportional to the energy deposited therefore proportional to Z^2, -dE/dx $\propto Z^2/v^2$ for low energy heavy particles). The veto counter pulse height,

† defined as $y = 0.5ln(\frac{E+P_L}{E-P_L})$

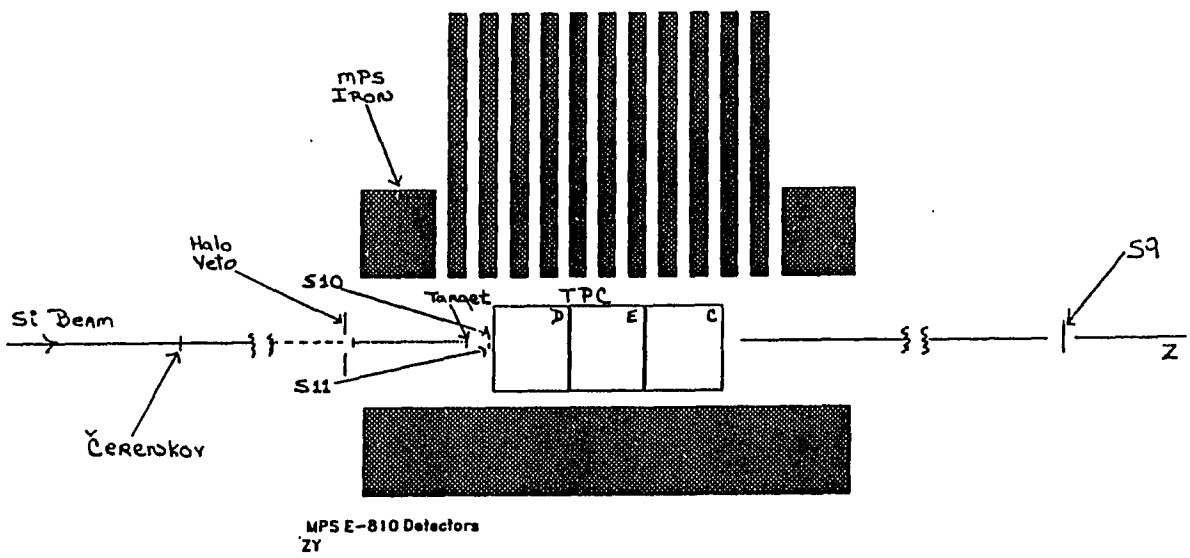

Figure[4.1]The location of the three TPC modules in the MPS magnet and of the trigger detectors. The beam Čerenkov and the veto scintillator are considerably further from the MPS than indicated.

which was recorded for further event selection, was found to correlate with the multiplicity of the events as determined by the TPC. To obtain a sample of centrally enriched events, triggers were selected which had a signal in the veto counter of less than 2 times minimum ionization. These events are referred as 'central' events.

Target thicknesses were selected to be ~1–3% radiation lengths in order to minimize gamma ray conversions that would give incorrect multiplicities. We used a 0.122 cm thick Si target (1.3% radiation length) and a 0.02 cm thick Pb target (3.5% radiation length). Other targets were also chosen for data taking in 1989 as: Au 0.025 mm, Cu 0.15mm and Al 0.8 mm. Results were published in Ref.11. Since the beam passed directly through the center of the TPCs, the beam rate was chosen to be $\sim$ 5000 ion/s, in order to limit the amount of ionization deposited in the TPCs.

System Operation:

As shown in Figure[4.2], the system operates as follows.

(1). When an interesting event is detected by fast trigger logic, a trigger pulse is sent to the main SSP (SSP0)

(2). SSP0 disables any further triggers and reads a module in a CAMAC crate to obtain a trigger classification.

(3). SSP0 passes trigger class information to other SSP's and issues commands to start up the other SSP's on the cable segment.

(4). Each SSP reads out the modules specified in its own DEVICE LIST loaded in at the beginning of the run for various trigger classes, data from each module is organized by the SSP's into a buffer with a header.

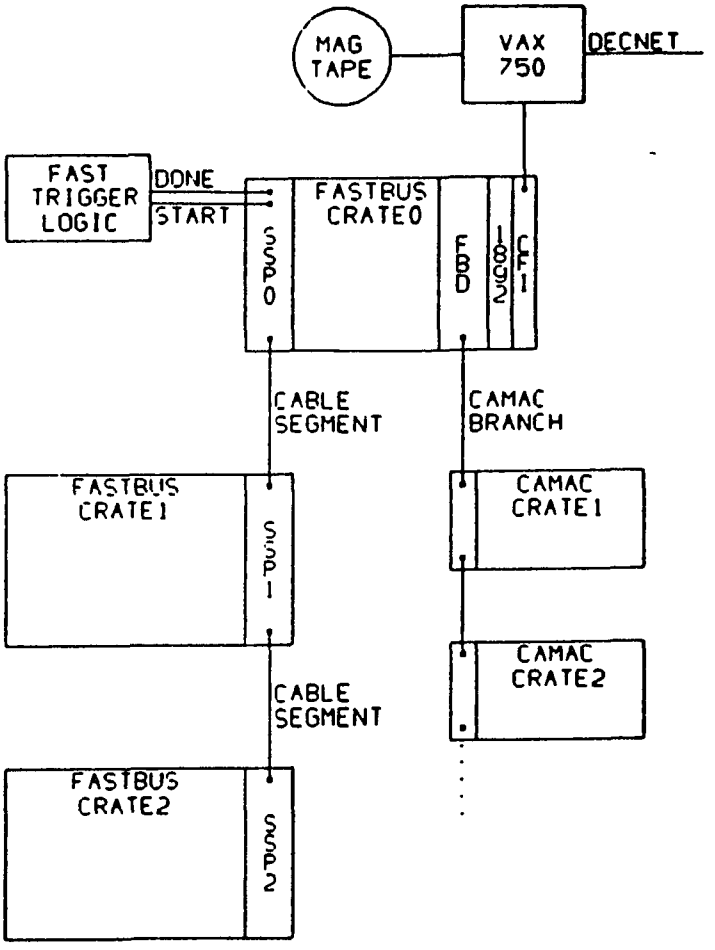

Figure[4.2] The MPS data-acquisition (DAQ) system hardware block diagram.

(5). When all SSP's on the cable segment have completed their device readouts, SSP0 reads their formatted data and appends this data to its own buffer with an additional header. Several events are formed into a bigger buffer and written to the FASTBUS memory, and when it is the end of the spill, SSP0 sets up a flag to let the host VAX read it. When the host VAX reads the whole spill, it checks with the online computer to see if it wants a data sample. If yes, it will send a few events to the online computer through DECNET.

(6). End of event, SSP0 re-enables triggers from fast trigger logic, and the sequence repeats from step (1).

4.2 Event Selection—Centrality Cuts

Events were reconstructed, with multiplicities of charged tracks ranging up to 100, using a three-dimensional tracking program. For the final data sample we selected the most central events using the multiplicity of the negatively charged tracks within our good acceptance. We found this to be a reasonably good measure of the centrality from both the increased yield of K_s^0's and Λ's[11] as a function of this multiplicity and from Monte Carlo studies of the correlation of impact parameter with this multiplicity. We selected central events (see Chapter 5) from the Si target by requiring this multiplicity to be >11, corresponding to a cross section of approximately 120 mb, and for Pb target we required this multiplicity to be >13, corresponding to a cross section of approximately 280 mb ($\approx$ 10% of the geometric cross section). This selection criterion resulted in 12679 central events from the Si target and 15438 events from the Pb target (13308 of them have at least one good Λ candidate).

4.3 Data Analysis

In order to reconstruct the decay vertices of neutral V^0's. The tracks which missed the interaction point by more than 7 mm were selected as candidates for decay vertices. To reduce combinatorial background for V^0's, we required the decay point to be more than 10 cm downstream of the interaction point and the reconstructed momentum vector had to point back to the production point within 2.5 mm. When there are vertices (V^0 candidates) with reconstructed momentum which do not point back to the production point, we saved them for further investigation of possible secondary V^0 decay from multi-strange hyperons (Ξ^- or Ω^-), even strangelets.

The (V^0) vertex size was required to be <3 mm.

In addition, in order to select tracks which had good momentum resolution, we required the sagitta of the measured tracks to be > 0.375 cm. The effective masses for K^0_s's and Λ's were calculated by kinematic hypothesis only by assigning a pion or a proton mass to the positively charged tracks and a pion mass to the negatively charged tracks which form a vertex.

Figure[4.3] shows the result of the effective mass calculation for the $\pi^+\pi^-$ hypothesis and Figure[4.4] shows the result of the effective mass calculation for the proton π^- hypothesis for our final selected sample from the Pb target. Decay vertices with effective masses in the range of 0.475–0.525 GeV/c^2 were selected as K^0_s's and those in the range of 1.106–1.126 GeV/c^2 were selected as Λ's. As can be seen, the K^0_s and Λ signals are quite evident and the backgrounds are relatively small ($< 10\%$). In all cases the tails of the effective mass distributions were used for background subtractions. Since there is considerable kinematic overlap between

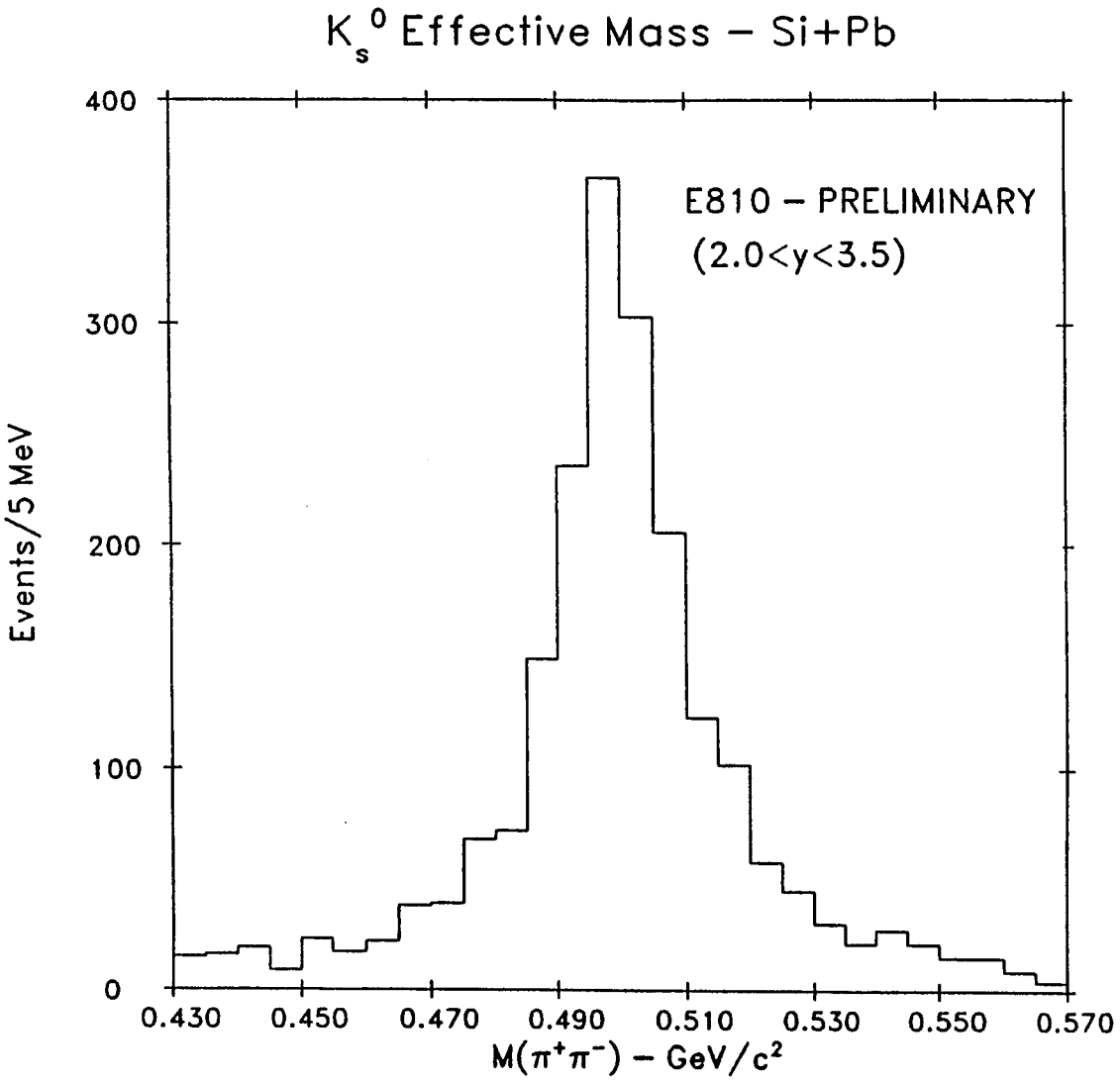

Figure[4.3] Effective mass plot of the $\pi^+\pi^-$ hypothesis for decay vertices from a *Pb* target with vertices removed if they satisfy the Λ effective mass cuts.

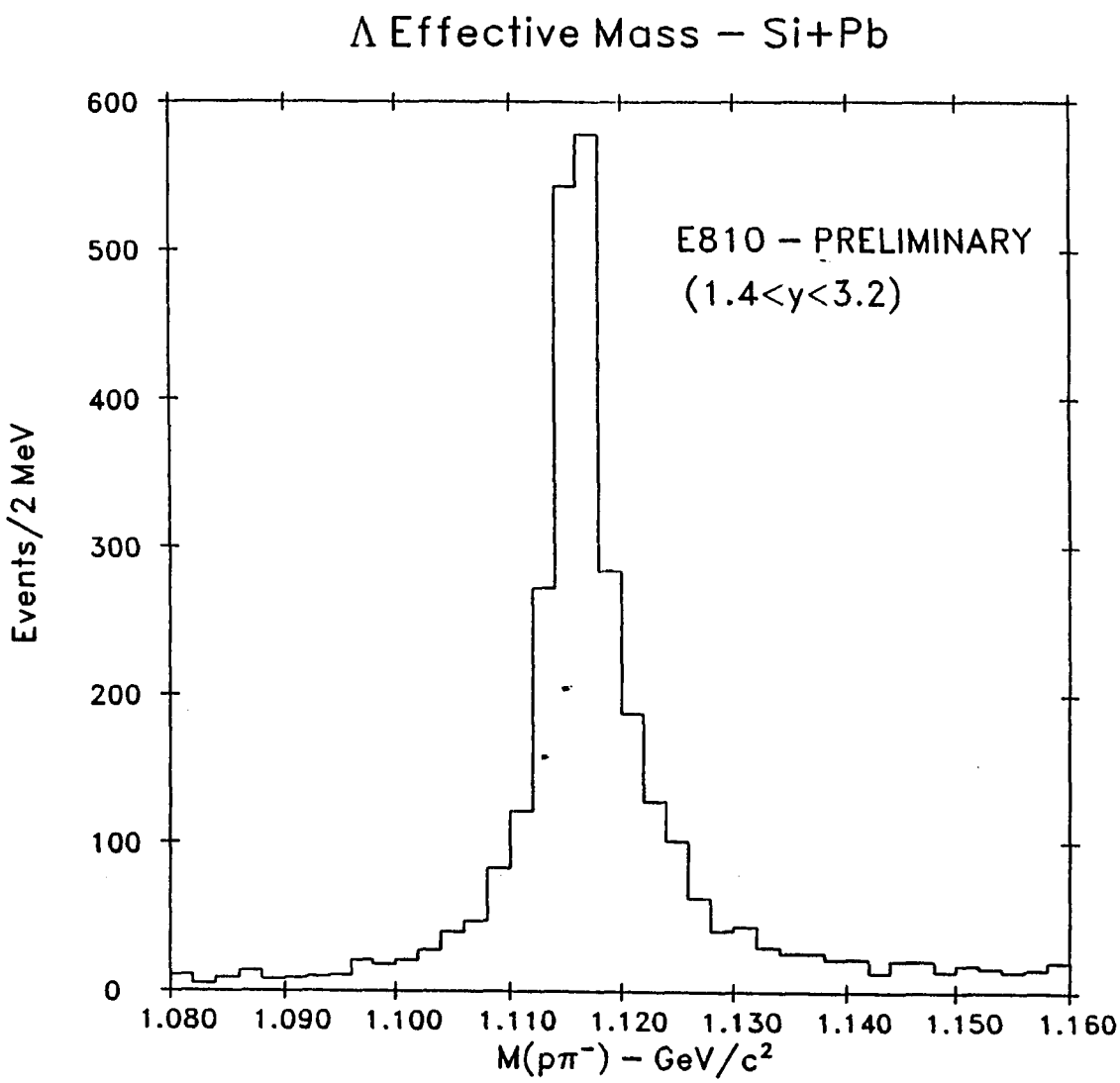

Figure[4.4] Effective mass plot of the proton π^- hypothesis for decay vertices from a *Pb* target.

K_s^0's and Λ's, Figure[4.3], our final K_s^0 data sample has decay vertices removed if they satisfy the Λ mass hypothesis. Because of phase space considerations, there is no significant background for Λ's due to K_s^0's, so no K_s^0 candidates were removed for Figure[4.4] (and the final data sample).

With 4894 (include background) well defined Λ's (1.106 GeV$\leq M\{\pi^- p\} <$ 1.126 GeV) from the Pb target, we successfully found a Ξ^- signal with the following procedures:

a). In all cases, we only use tracks that are well measured, which means that they all have sagittas larger than 0.375 cm, for better momentum resolution.

b). With each Λ we found from the π^-p hypothesis, we project the Λ backward to the target plane where it has to miss the primary vertex by at least 0.25 cm

c). Then we search in the upstream area of the Λ vertex for negative tracks which are not from the primary vertex, but come close to the Λ trajectory within 0.4 cm

d). We then take this as a possible Ξ^- decay vertex and extrapolate it backward as a helix with the momentum of $\vec{P}(\Xi^-) = \vec{P}(\Lambda) + \vec{P}(\pi^-)$ to the target plane (at 44 cm). It has to end up within 0.6 cm of the primary vertex if the Ξ^- decayed between 50-60 cm. We loosen this cut to 0.975 cm if Ξ^- decayed after 60 cm.

For all the vertices that survived the above cuts, we calculated their effective mass with the $\pi^-\Lambda$ hypothesis as plotted in Figure[4.5]. We selected those 99 candidates that lie in the range of 1.306-1.336 GeV/c^2 as our Ξ^- signal. Those 22 which lie in the range of 1.280-1.294 GeV/c^2 and 1.348-1.364 GeV/c^2 are treated as backgrounds.

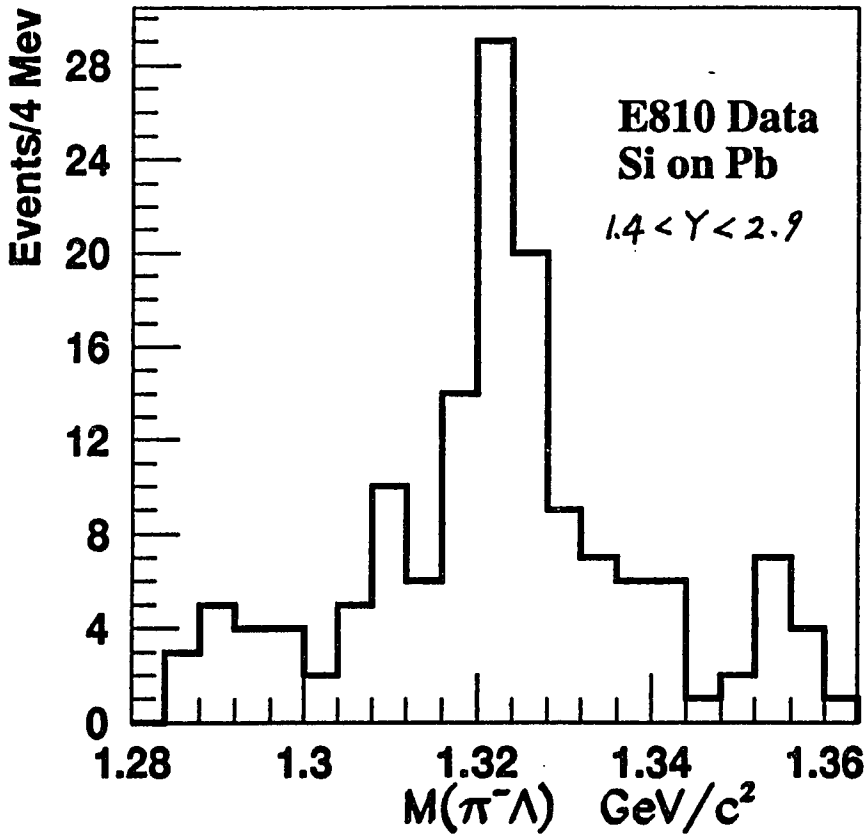

Figure[4.5] Effective mass plot of the $\pi^-\Lambda$ hypothesis for decay (into a negative and a neutral) vertices from a *Pb* target.

A typical, reconstructed Ξ^- decaying in our TPC module is shown in Figure[4.6] and Figure[4.7].

In order to optimize the Ξ^- mass peak, we studied the sensitivity of the cuts applied. We found that the existence of the Ξ^- mass peak is not sensitive to the cuts applied. However, the signal to background ratio showed a certain dependency on the cuts, as it should. The most obvious effect comes from the cuts on the decay length (6cm–16cm) of Ξ^- and the primary vertex size (0.6cm–0.975cm) for the reconstructed Ξ^- candidates.

The longer the decay length cut, the cleaner the signal is. The larger the primary vertex size, the more background we get. At 16 cm decay length and 0.6 cm primary vertex size we have the cleanest signal ($\approx$65 Ξ^- candidate and $\approx$6:1 signal to background). By loosening up the cuts we introduce more background. With the purpose of maximizing the number of Ξ^- candidates at an acceptable level of signal to background ratio ($\approx$5:1), we settled down on the final cuts as listed above. All other cuts are even less sensitive.

We used another method to convince ourselves that the Ξ^- mass peak was not purely due to some kind of mysterious cuts. We applied the same cuts as listed above to the same data sample, but with Λ's looking for partner π^-'s from a different event. This way we can have a sense of the background signals that came from a purely accidental match. Figure[4.8] shows the mixed track combination study with the same 13308 E810 central Si on Pb events with Λ candidates that yielded the Ξ^- mass peak. Figure[4.9] shows the similar study with 38809 Monte Carlo events. In both cases, no sign of enhancement at Ξ^- mass was found and very little background was seen.

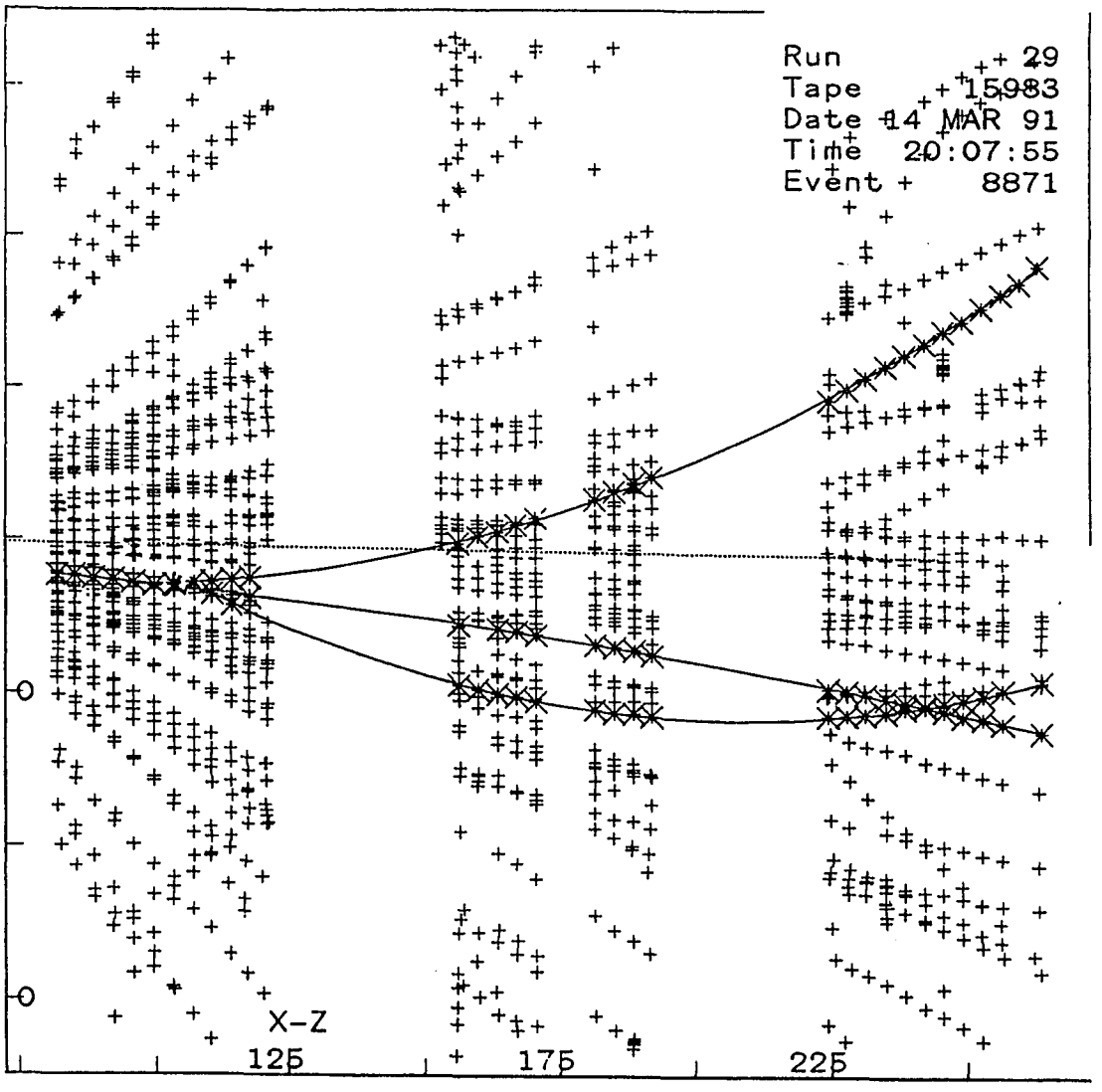

Figure[4.6] The Z-X view of a Ξ^- decaying in our TPC modules

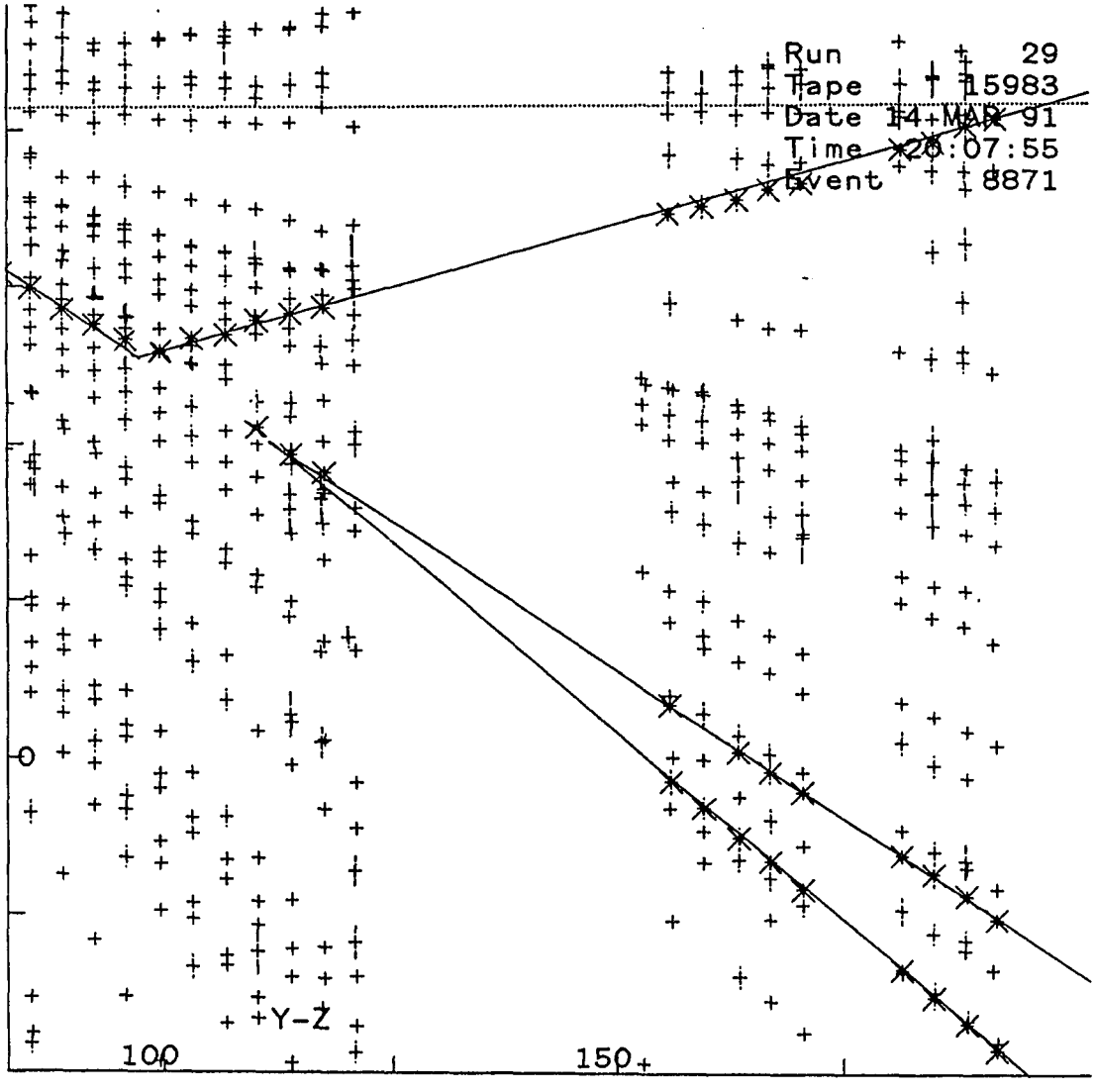

Figure[4.7] The enlarged Z-Y view of a Ξ^- decaying in our TPC modules

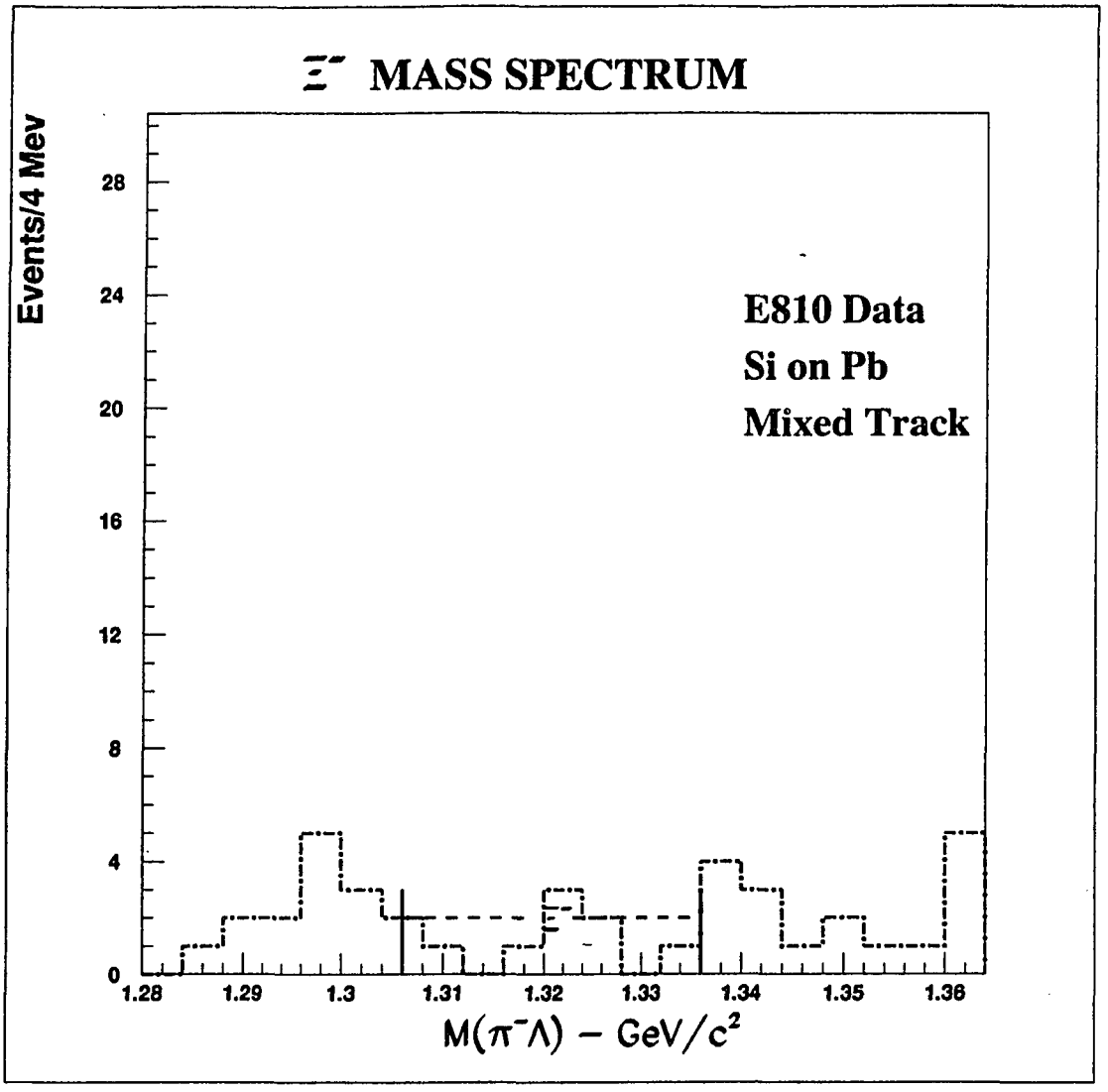

Figure[4.8] The $\pi^-\Lambda$ (from 13308 central *Si* on *Pb* events) effective mass plot with π^-'s and Λ's from different events.

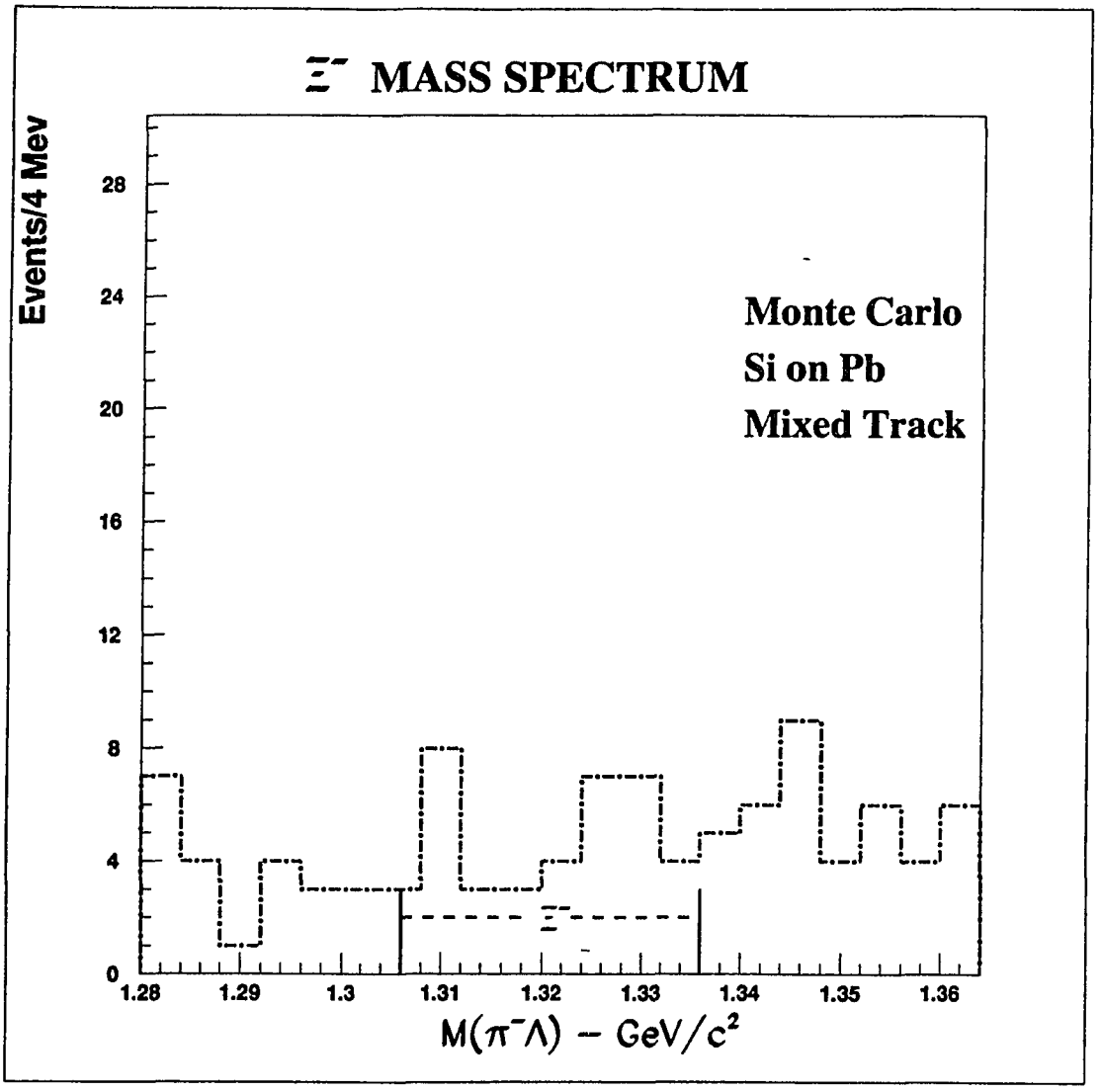

Figure[4.9] The $\pi^-\Lambda$ (from 38809 central *Si* on *Pb* Monte Carlo events) effective mass plot with π^-'s and Λ's from different events.

4.4 Acceptance Calculation

As indicated in Ref. 11, the acceptances for the V^0's (satisfying the various cuts) were calculated by performing a complete Monte Carlo simulation of events using GEANT3. Events were generated using a modified HIJET[12] model (we call it AGSHIJET). The resultant four-momenta of the generated tracks were used as input to the GEANT3 program, which did the tracking in a magnetic field. The generated hits included all the known effects of detector apertures, efficiencies, resolutions and distortions. The model parameters were adjusted to approximate the data in order to minimize any systematic errors in acceptance calculations when an integration was performed over a kinematic variable. The output of the GEANT3 program was in identical format to the actual raw data format. The results of this simulation were then analyzed by the same program used to analyze the actual data. The output of this analysis provided the numerator for the acceptance calculation, while the input provided the denominator. The momentum space has been cut into small grids as shown in Figure[4.10]. The acceptance was calculated for each small grid in the Y—P_t plane. This makes the final rapidity distribution after acceptance correction to be independent of the model (used to generating these V^0's for simulation) within our estimated systematic error of 20%.

The K^0_s acceptance (within our measured region of $2.0 \leq Y < 3.5$ and $P_t \leq$ 1.0 GeV) was in the range of 5%–20%. The Λ acceptance (within our measured region of $1.4 \leq Y < 2.9$ and $P_t \leq 1.0$ GeV) was in the range of 3%–12% including the correction for neutral decays.

The acceptance for the Ξ^- was done in a similar way. Events were also generated by using the AGSHIJET model.

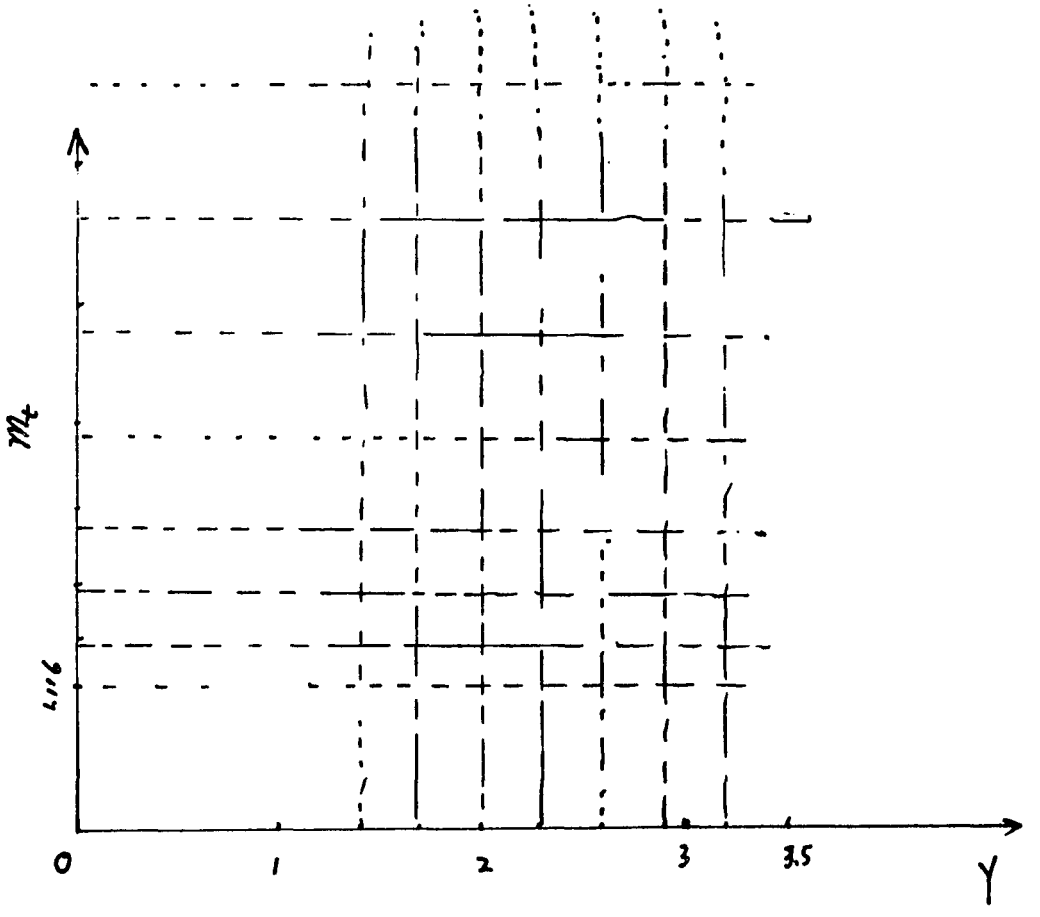

Figure[4.10] The acceptance for V^0s was calculated in each of these individual small grid in Y–P_t plane to avoid any bias.

However, because AGSHIJET generated very few Ξ^-'s and the detector's acceptance for Ξ^- was very low, it will take years to compute. We created a large amount of Ξ^- with two different models (AGSHIJET+N* and Fireball$^+$), and carefully embedded them into the AGSHIJET events. Ten Ξ^-'s of different rapidity (defined as $y = 0.5ln(\frac{E+P_L}{E-P_L})$) were embedded in each event, they were distributed evenly according to φ angle. Due to the low efficiency of the upper half TPC, basically the whole upper half of the TPC was blind to Ξ^- (almost zero acceptance). This is due to the higher requirement to reconstruct a Ξ^-—all of the three tracks has to be well measured and pass the track length and sagitta cut. This also made it justifiable that we embed ten (effectively five) Ξ^- in one event. We did careful studies and made sure that these Ξ^- didn't interfere with each other, and especially their decay products didn't group together to make fake Ξ^-'s. The Ξ^-'s were distributed in different φ bins and 10000 events were studied. No fakes due to the number of overlapping Ξ^-'s were generated.

Half a million Ξ^- from the fireball$^+$ model were used for the acceptance calculation, while 400000 Ξ^- from AGSHIJET model were used for another set of acceptance calculations.

The Ξ^- acceptance was in the range of 0.59%—3.6% using the fireball$^+$ model, and in the range of 1.8%—4.8% for using the AGSHIJET model.

Chapter 5

The Results and Discussions

5.1 The Rapidity[‡] Distributions of K^0_s's and Λ's

As mentioned in Chapter 4, a large number of K^0_s and Λ has been reconstructed from the Si+Pb data by hypothetically assuming that the charged tracks from a decay vertex posses proton or $\pi^{\pm}$ masses. The acceptance calculation for K^0_s and Λ were done by cutting the Y–P_t plane into grids. At each grid which is a very small phase space region, the acceptance was calculated for each kind of particle and they are independent (within the 20% estimated systematic error) of the model used to generate the events.

We estimate an overall systematic error of 20%. This error is due to the centrality cut we applied when selecting central collision events. As discussed in Reference 11, negative particles that went through at least the first TPC module and have a π^- rapidity >1.7 have a good acceptance in our apparatus, thus we have chosen the multiplicity of these negative particles as a measure of the energy deposited in the interaction. It is important to note that the highest multiplicities very probably correspond to the most central events. The Λ yield per event, corrected for the neutral branching ratio, is shown as a function of this negative multiplicity in Figure[5.1] for Si on Cu and Au events. The yields show a monotonic increase with increasing multiplicity, hence the largest yield very probably correspond to the most central events.

It is clearly shown in Figure[5.1] that the Monte Carlo (HIJET) events have

---

‡ Rapidity is defined as $y = 0.5ln(\frac{E+P_L}{E-P_L})$

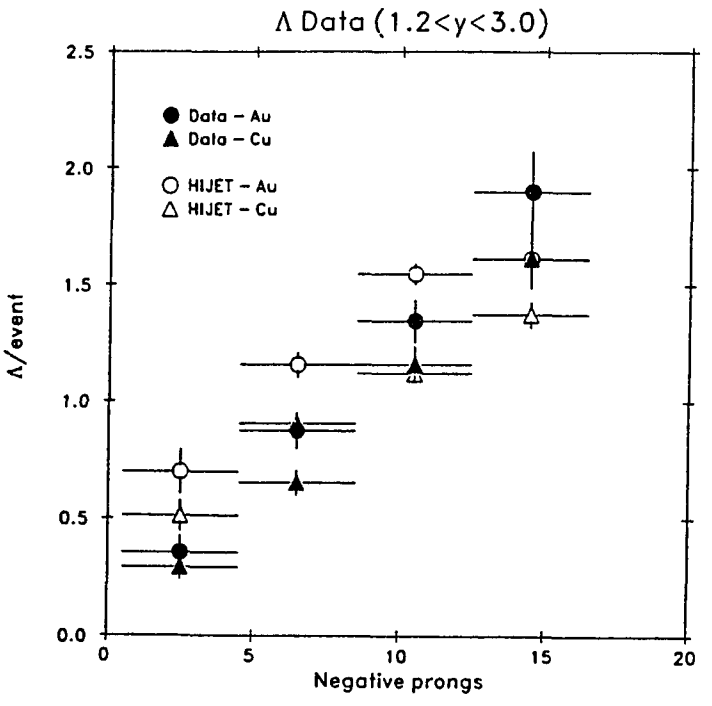

Figure[5.1] Λ yield in the rapidity region 1.2< y <3.0 as a function of negative track multiplicity as described in the text. The errors shown are statistical only.

yields which deviate from the monotonic increase. This indicates that the proportional relation between the Λ yield and the negative multiplicity may not be that simple at the most central collisions. One of the most obvious reasons is that in general the number of particles produced is inversely proportional to the impact parameter b, and one expects more particles at smaller impact parameter b's. However, at smaller b's the average rapidities of produced particles become smaller. Therefore our acceptance is falling with impact parameter b. Another important reason is that Λ's and π^-'s with the same rapidity (Lorentz invariant) end up with different pseudorapidities ($e^\eta = ctg\frac{\theta}{2}$) and may fall in ($\Lambda$'s) or out ($\pi^-$'s) of our apparatus. As a result of HIJET acceptance studies[11], we estimate an additional systematic error of about 20% for our choice of centrality cut, which is >13 well measured negative tracks for Si on Pb and >11 for Si on Si (see section 4.2).

The acceptance corrected lifetime (proper time) distribution for K^0_s and Λ are shown in Figure[5.2] and Figure[5.3] . The solid lines in figures are not fits, they are the known lifetimes of the particles given by the Particle Data Group Value. The agreements are obvious, and demonstrates that we have indeed observed K^0_s and Λ events, and also gives us confidence in the acceptance calculations.

The acceptance corrected rapidity distribution for K^0_s's from Si and Pb targets are plotted in Figure[5.4] and Figure[5.5], respectively.

The errors shown in the figures are statistical only, they were obtained by mapping a χ^2 contour of 1 σ away from the best fit, since the integration of an exponential involves folding errors of two correlated variables—the intercept and slope of the exponential.

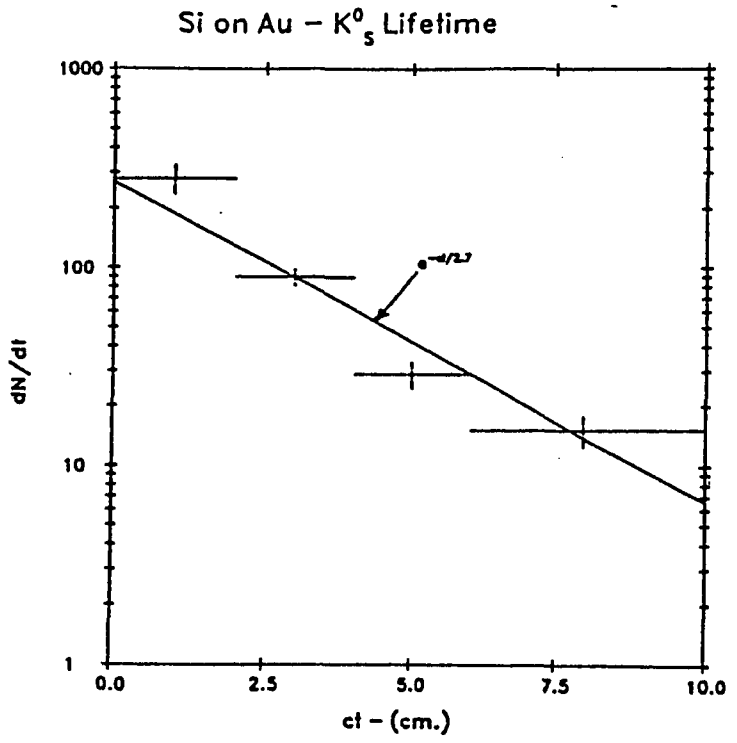

Figure[5.2] The acceptance corrected lifetime (proper time) distribution for K^0_s. The solid line in the figure is not a fit, it is the known lifetime of K^0_s given by Particle Data Group value.

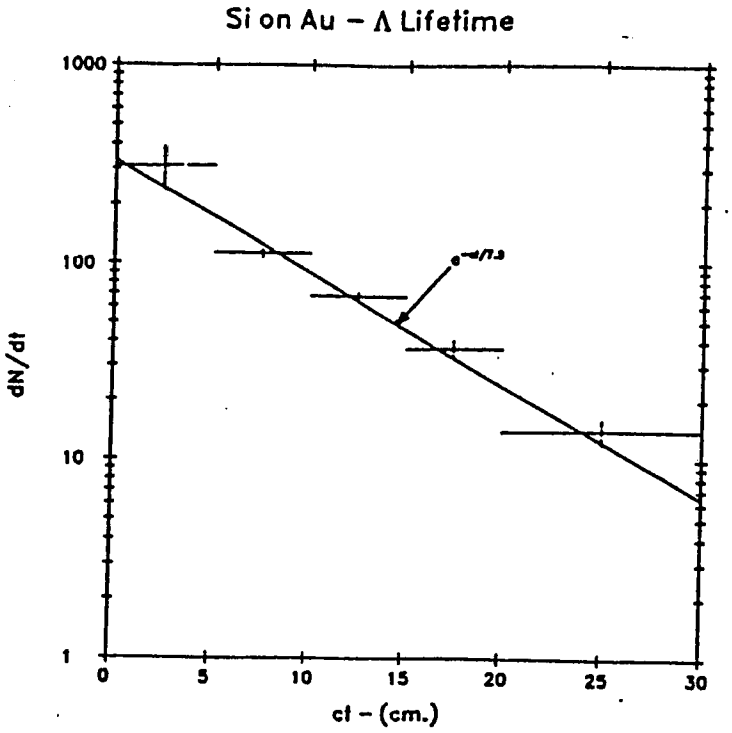

Figure[5.3] The acceptance corrected lifetime (proper time) distribution for Λ. The solid line in the figure is not a fit, it is the known lifetime of Λ given by Particle Data Group value.

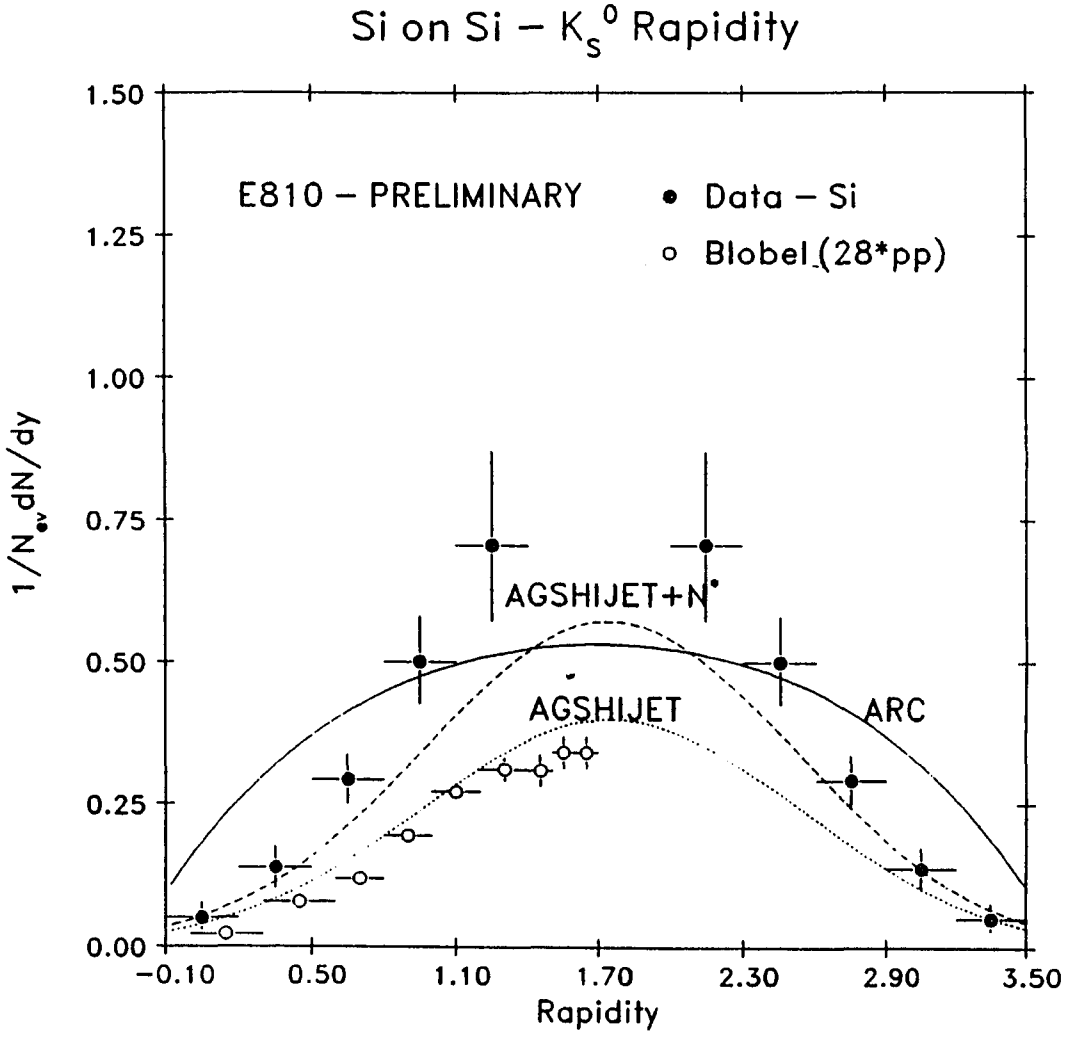

Figure[5.4] The acceptance corrected rapidity distribution for K_s^0 from *Si* on *Si* data.

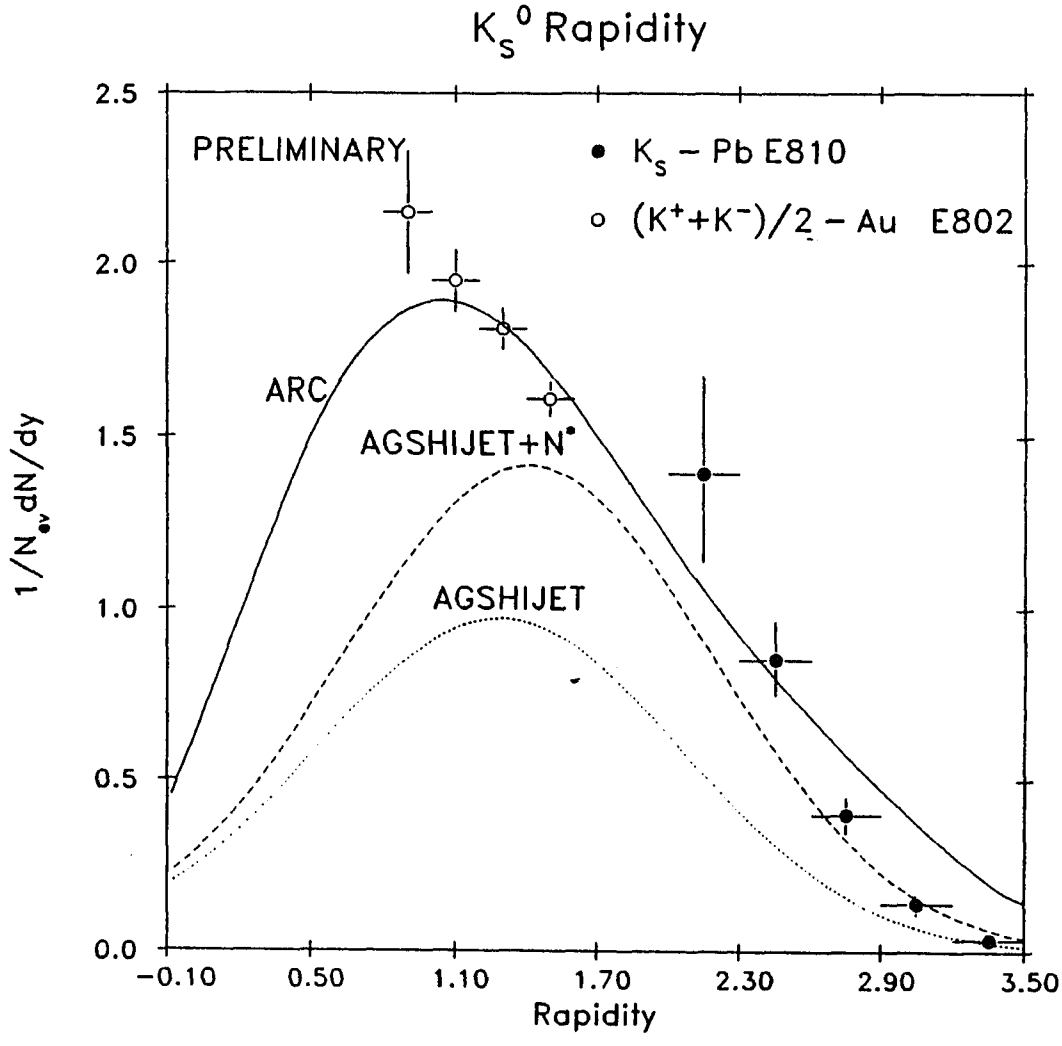

Figure[5.5] The acceptance corrected rapidity distribution for K_s^0 from Si on Pb data.

The solid curves shown in the figures are predictions from ARC (A Relativistic Cascade) model. The dashed curves shown in the figures are predictions of the AGSHIJET+N* model, which has a higher yield of K_s^0 than AGSHIJET without N*'s involved (dotted lines). In Figure[5.4] only the solid points above the rapidity of 1.7 are our measurements. The open circles below the rapidity of 1.7 are the reflection of our measurements about 1.7 (which corresponds to y≈0 in the nucleon–nucleon center-of-mass system) because of the symmetry of the reaction. In this way we obtain a measurement of the whole rapidity distribution. The open squares represent the measurement of the rapidity distributions for $p + p \rightarrow K_s^0 + X$ at 12 GeV/c (by Blobel *et al.*)[8] scaled up by a factor of 28. In Figure[5.5] the open circles are the average values of K^+ and K^- measurements of E802[9,13] for the $Si + Au$ interactions. We expect, from isospin conservation, that this average K^+, K^- cross section should be the same as $dN/dy(K_s^0)$. Considering that the measurements were on a lighter target and are at a different rapidity, we observe good agreement with the results of E802[13].

Figure[5.6] and Figure[5.7] show the acceptance corrected rapidity distributions for Λ's from Si and Pb target respectively. Predictions from the same models (ARC, AGSHIJET+N*) are plotted together with our data. In Figure[5.6] the open circles are the reflections of our measurement about rapidity 1.7 because of the symmetry of the reaction $Si + Si$ about 1.7 . And the open squares represent the measurement of rapidity distributions for $p + p \rightarrow \Lambda + X$ at 12 GeV/c (by Blobel *et al.*)[8] scaled up by a factor of 28.

5.2 The Transverse Mass Distributions of K_s^0's and Λ's[3,14]

Our data are consistent with an exponential dependence in transverse mass ($m_t = \sqrt{m_0^2 + p_t^2}$). In Figure[5.8] and Figure[5.9] we present the differential cross

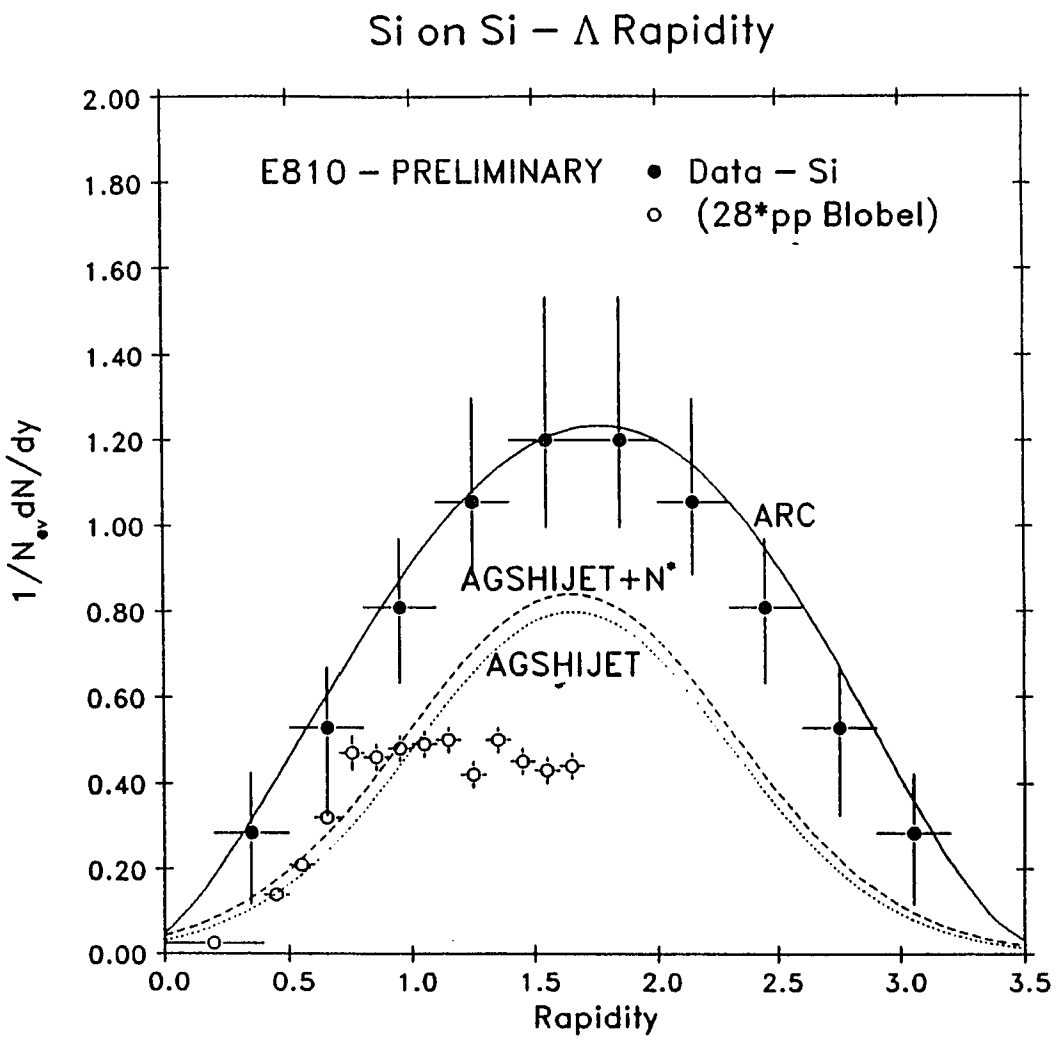

Figure[5.6] The acceptance corrected rapidity distribution for Λ from *Si* on *Si* data.

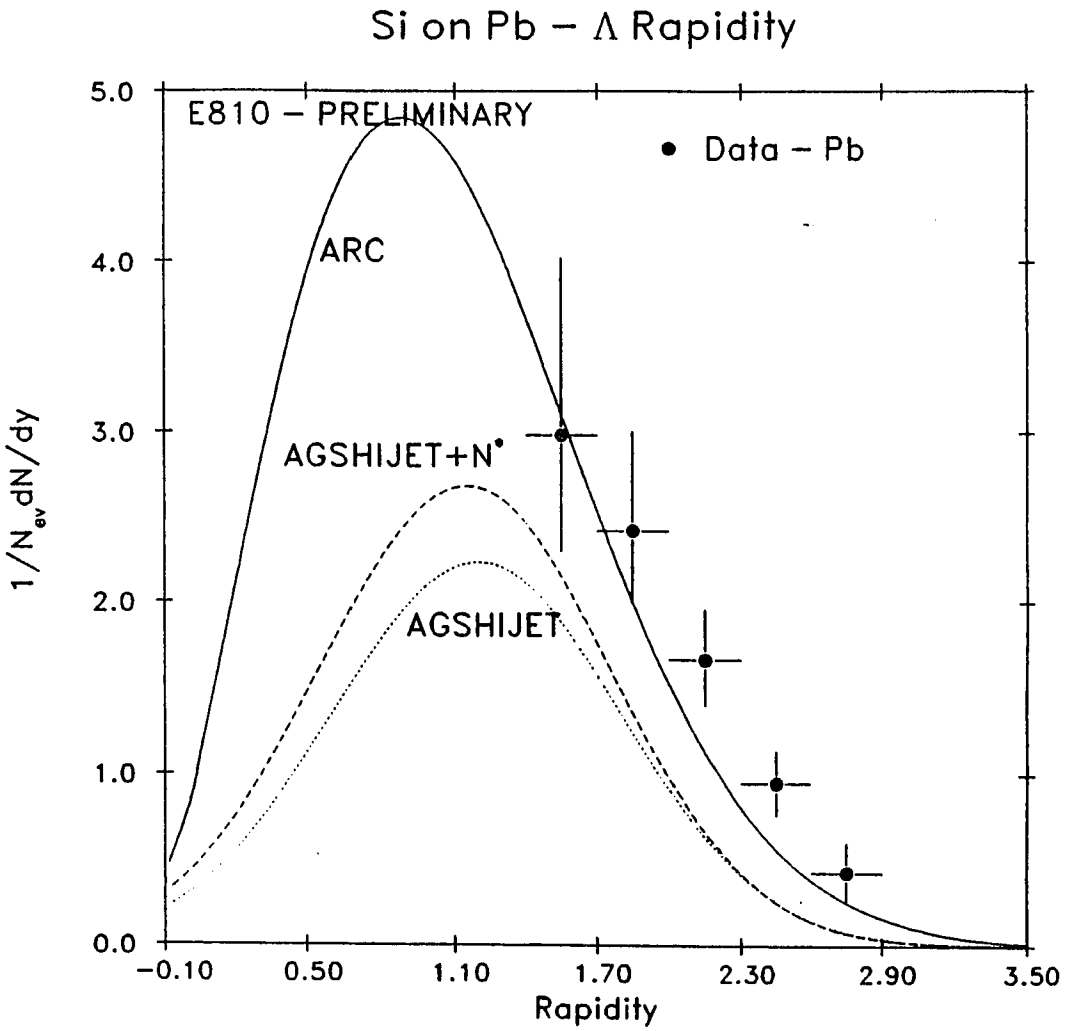

Figure[5.7] The acceptance corrected rapidity distribution for Λ from Si on Pb data.

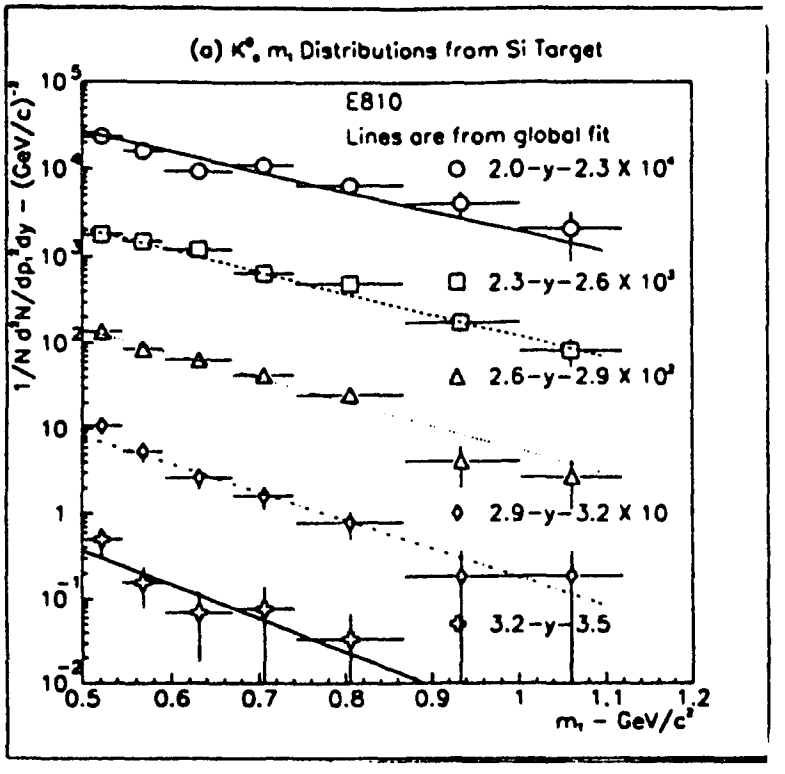

Figure[5.8] The differential cross section for K^0_s produced from Si on Si data.

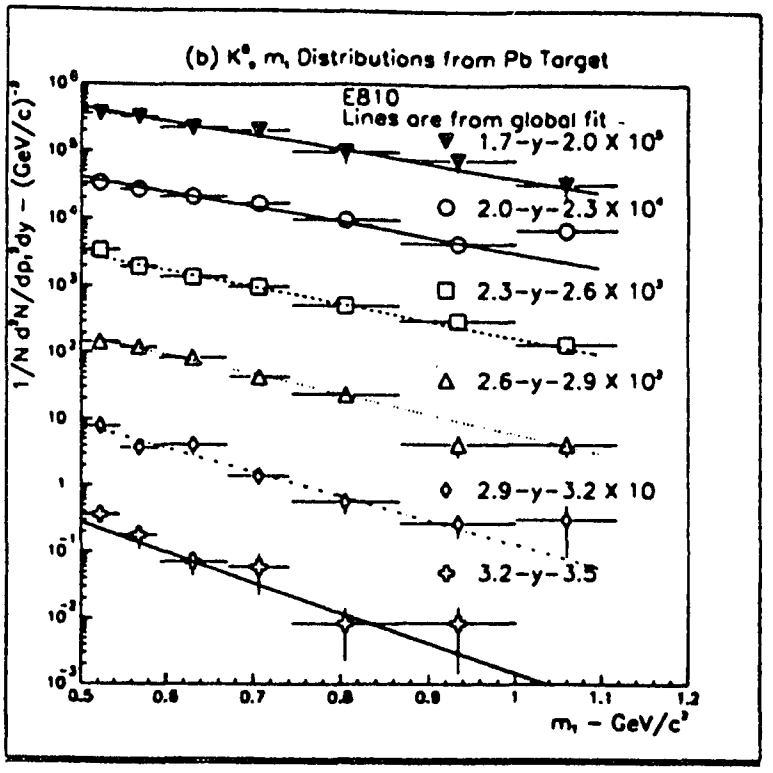

Figure[5.9] The differential cross section for K_s^0 produced from Si on Pb data.

section, $1/m_t d^2N/dydm_t$, where $m_t = \sqrt{p_t^2 + m_0^2}$, for K_s^0 production from Si and Pb targets. In order to extrapolate to unmeasured regions of the transverse momentum p_t we have fitted our acceptance corrected data to $Aexp(-Bm_t)$ where A is an arbitrary constant independent of rapidity and $B = a + b \times cosh(y - y_0)$, with a and b independent of rapidity to represent a cascade term plus a fireball respectively. The inverse slope of the exponential is usually called the temperature of the fireball. With the addition of the cosh(y) term we obtained a significantly better χ^2 probability in fitting the K_s^0 data. The K_s^0 temperatures at midrapidity were in the range of 200–240 MeV with errors of $\sim$ 40 MeV. The K_s^0 temperatures drop off to $\sim$ 100 MeV at high rapidities for both Si and Pb targets.

In Figure[5.10] and Figure[5.11] we have plotted the differential cross sections for Λ production from Si and Pb targets. The Λ temperatures at midrapidity were in the range of 200–260 MeV with errors of $\sim$ 70MeV. The Λ temperatures decrease to $\sim$ 100–150 MeV for both Si and Pb targets at high rapidities.

In Figure[5.12] and Figure[5.13] we have plotted the inverse slopes of K_s^0 as a function of rapidity for Si and Pb targets. In Figure[5.14] and Figure[5.15] we have plotted the inverse slopes of Λ as a function of rapidity for Si and Pb targets. In all four cases, the AGSHIJET+N* have failed to describe our data while predictions from other models are not available. However, with a cosh(y) term representing a fireball, the global fit (fireball$^+$ model) has acceptably explained our data.

In Table[5.1] we compare the χ^2 probabilities for the constant slope (temperature) assumption and the fireball$^+$ model with a cosh(y) term. It clearly shows that the fireball$^+$ model is necessary to provide an acceptable fit to all the above data. One should note that the fireball term is essential to fit the K_s^0 data. The fireball term actually came from Boltzmann distribution (since E = m_t cosh(y)) which

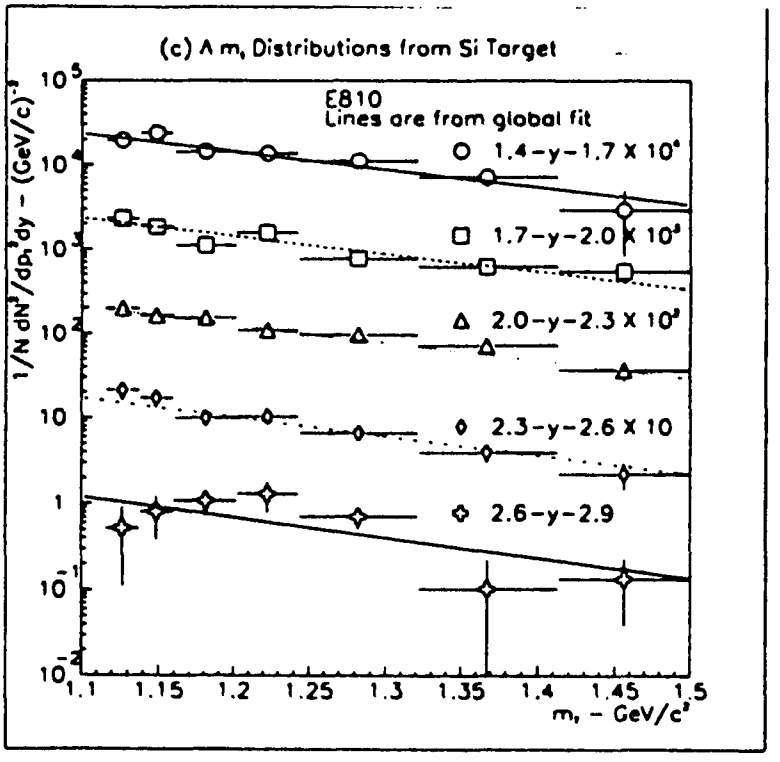

Figure[5.10] The differential cross section for Λ produced from Si on Si data.

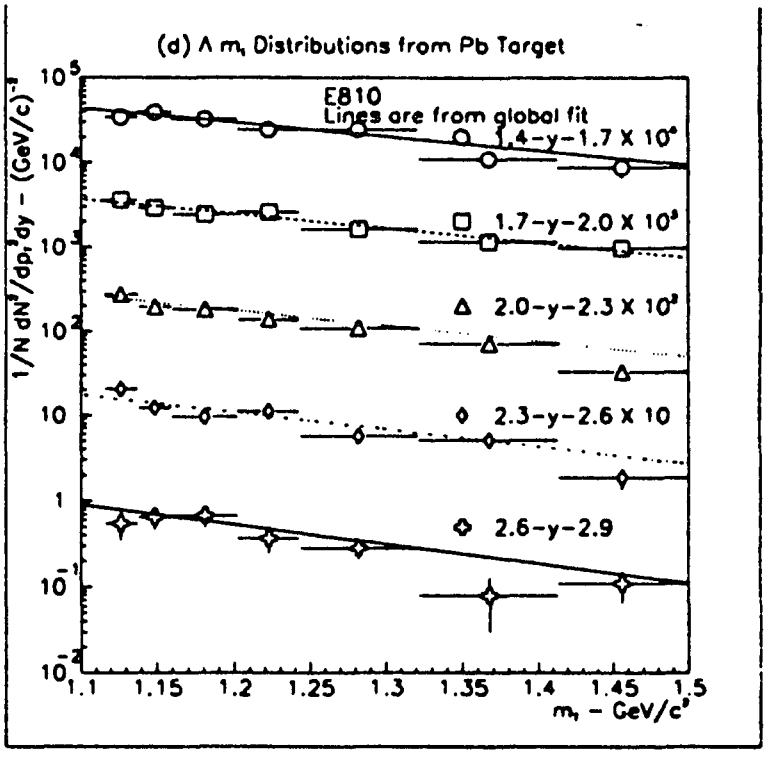

Figure[5.11] The differential cross section for Λ produced from Si on Pb data.

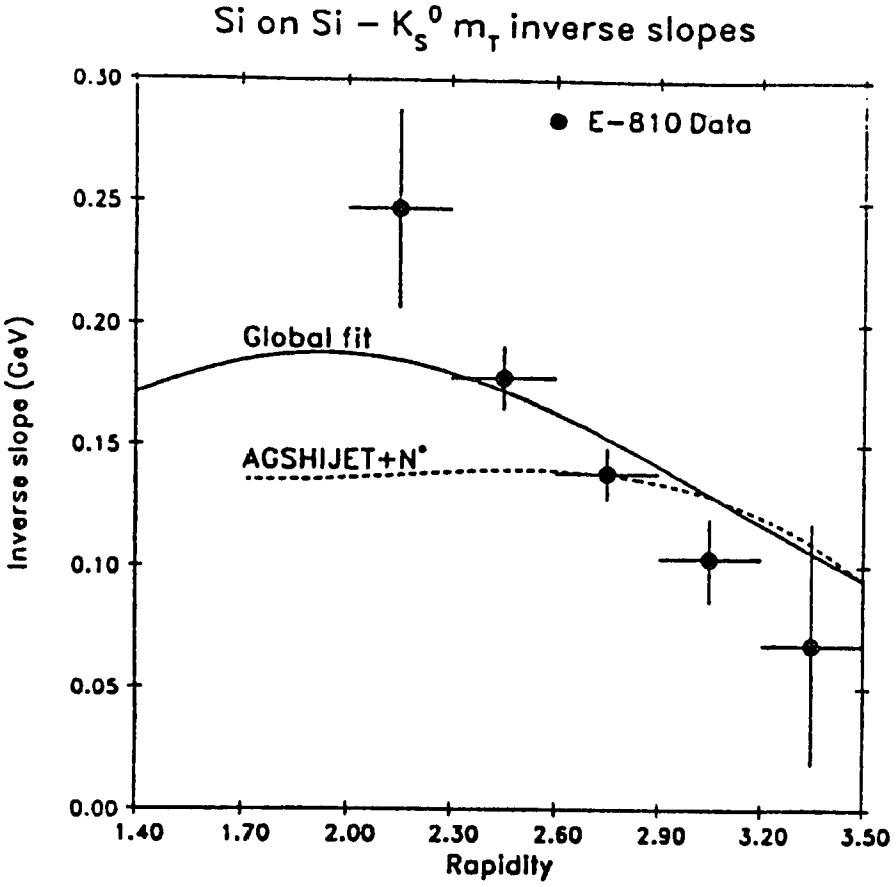

Figure[5.12] Inverse exponential slopes for K_s^0's from the *Si* target. The points are fits to an exponential in each rapidity bin. The solid curve is the result of our global fit (fireball$^+$ model), not a fit to the points. The statistical error on the curve representation is similar to that shown on the individual points. The dashed curve is the prediction of AGSHIJET+N*.

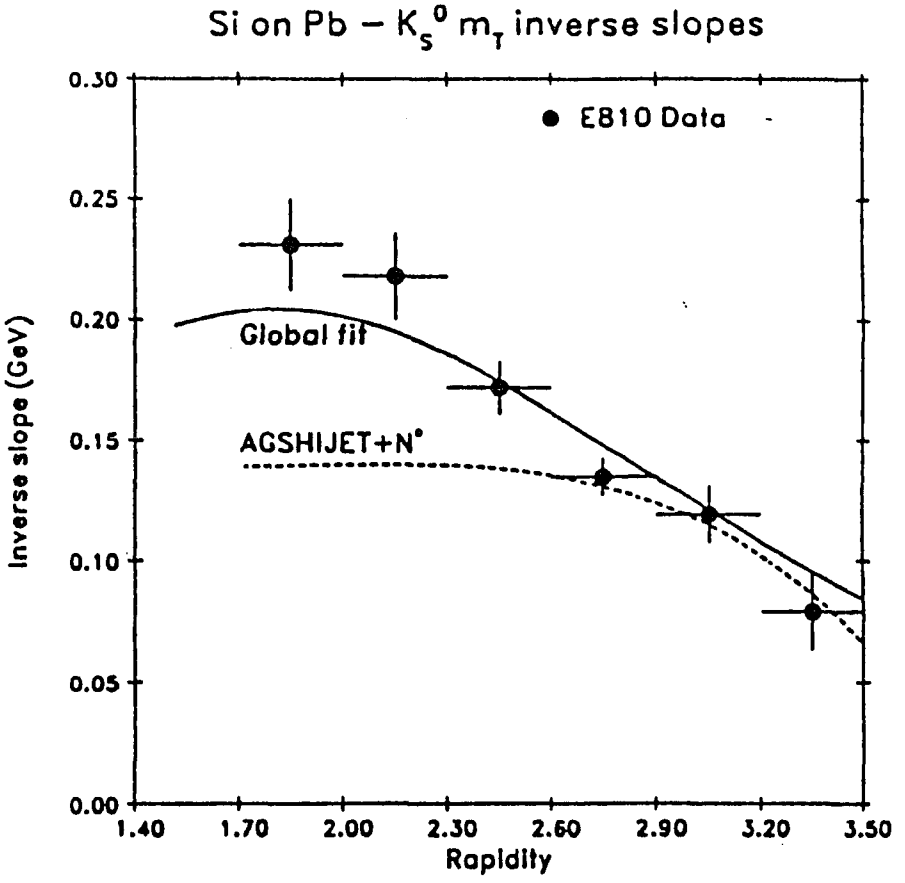

Figure[5.13] Inverse exponential slopes for K_s^0's from the *Pb* target. The points are fits to an exponential in each rapidity bin. The solid curve is the result of our global fit (fireball$^+$ model), not a fit to the points. The statistical error on the curve representation is similar to that shown on the individual points. The dashed curve is the prediction of AGSHIJET+N*.

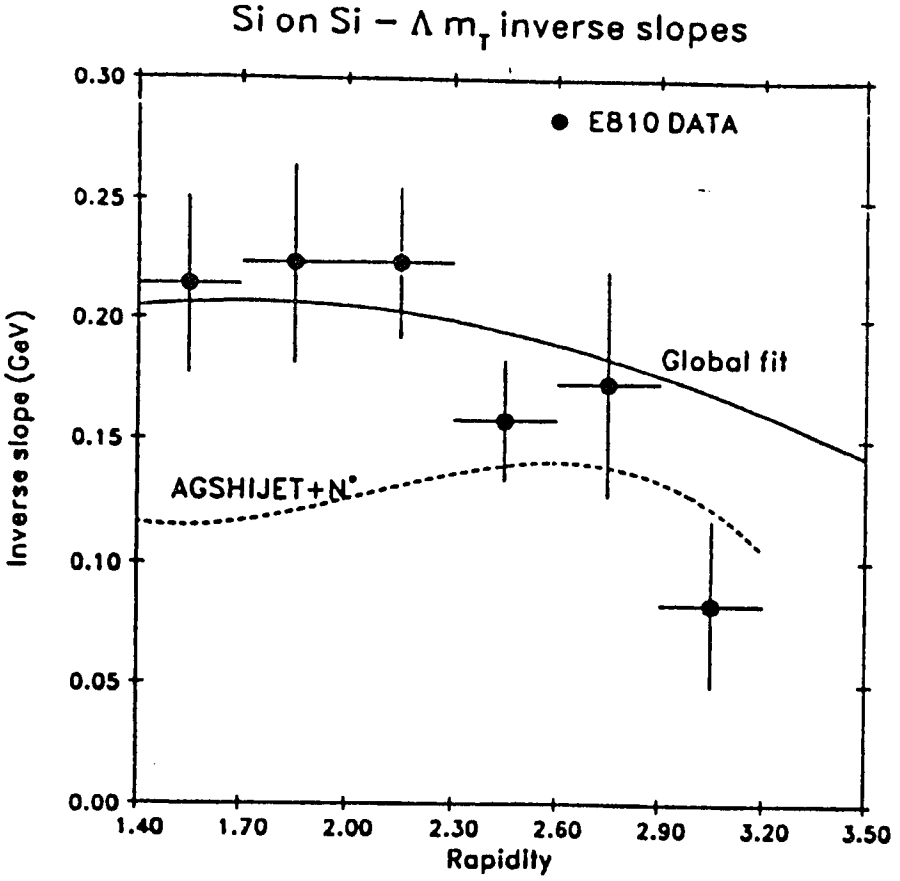

Figure[5.14] Inverse exponential slopes for Λ's from the *Si* target. The points are fits to an exponential in each rapidity bin. The solid curve is the result of our global fit (fireball$^+$ model), not a fit to the points. The statistical error on the curve representation is similar to that shown on the individual points. The dashed curve is the prediction of AGSHIJET+N*.

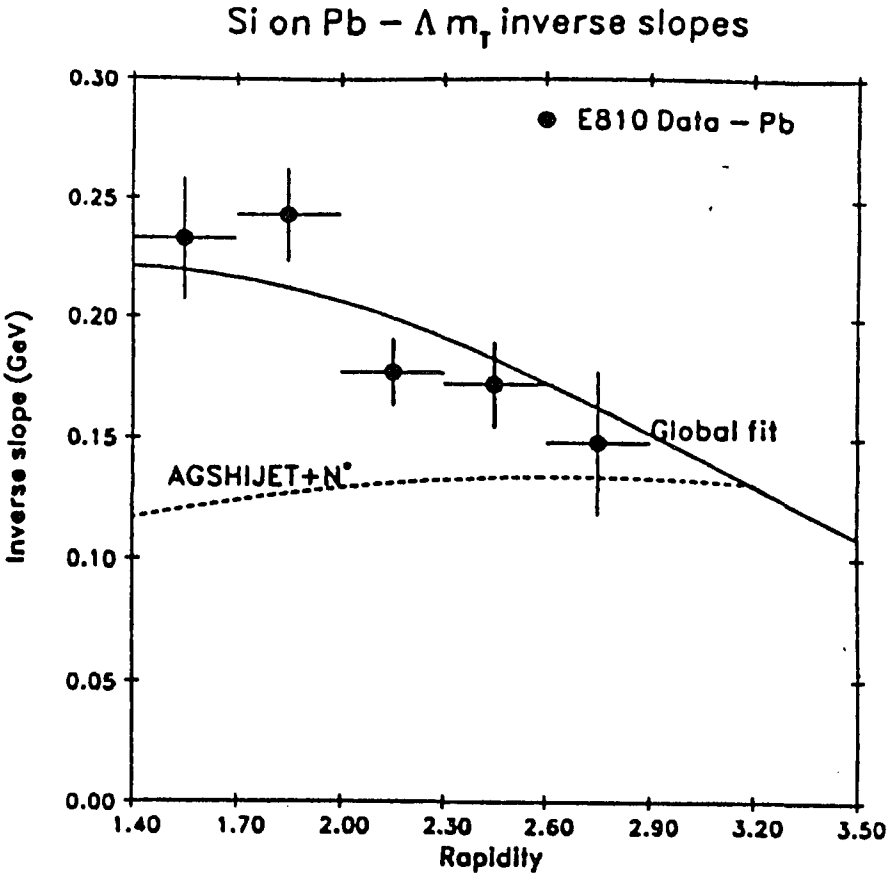

Figure[5.15] Inverse exponential slopes for Λ's from the *Pb* target. The points are fits to an exponential in each rapidity bin. The solid curve is the result of our global fit (fireball$^+$ model), not a fit to the points. The statistical error on the curve representation is similar to that shown on the individual points. The dashed curve is the prediction of AGSHIJET+N*.

describes a thermal equilibrated system. This tells us that mesons are closer to thermal equilibrium than baryons (lighter meson mass is one reason) and this is one of the reasons that we expect heavier multistrange hyperons to bring us cleaner (with less background from HG phase) information of QGP phase before it hadronizes if it were ever created.

Particle	Target	Constant slope $P(\chi^2)$	cosh(y) added $P(\chi^2)$
K^0_s	Si	8%	57%
K^0_s	Pb	$< 0.01\%$	52%
Λ	Si	67%	66%
Λ	Pb	4%	22%

Table[5.1] χ^2 probabilities for the two fit hypotheses as explained in text.

5.3 The Cascade Models' Predictions of Strangeness Production

The first thing to be noted is that our Si data cannot be described by the naive assumption that we can scale up the pp cross sections by 28. Of course a simple cascade of NN collisions cannot explain our data either.

We have modified the old HIJET event generator[12] for AGS energies as described in Ref. 15. We call this model AGSHIJET. The dotted curves in figures [5.4]—[5.7] represent AGSHIJET predictions (with zero formation time) ‡ which under predicted the K^0_s and Λ yield by a factor of two in each case.

The HIJET generator considers p-A and A-A collisions to be a sum of independent N-N collisions, with the N-N cross section and scattering dynamics not depen-

‡ This is not a physically justifiable result, but was used to merely indicate that even in this extreme best attempt case we could not get enough K^0_s and Λ.

dent on whether the nucleon has previously participated in an interaction. For each primary N-N interaction, a call is made to the MINBIAS routine which computes the energy loss of the colliding nucleons and the production of particles. MINBIAS is based on inclusive high energy N-N interactions forming multi-pomeron chains, with each chain fragmenting according to the Field-Feynman algorithm[16]. At beam momentum below 50 GeV/c MINBIAS had to be modified in order to agree with p-p data[8].

HIJET takes account of the geometry of the A-A collision, it populates nucleons in the target and the projectile systems according to a Woods-Saxon distribution. Each nucleon is given a Fermi momentum which has a gaussian distribution with a σ of 200 MeV/c. The nucleons are off the mass shell, with the average binding energy being 8 MeV. An interaction between a projectile and a target nucleon occurs when the distance of the closest approach is less than $\sqrt{\frac{\sigma}{\pi}}$ with $\sigma = 33$ mb (this distance is 1.025 Fermi the approximate size of a proton). When N*'s are colliding, this distance is taken to be 20% larger representing their size†.

Secondaries produced in the collisions or produced by N* decay have a finite formation time given by the distribution:

$$F(\tau) \propto exp\Big[-\Big(\frac{\tau - \tau_0 cosh(y)}{\sigma cosh(y)}\Big)^2\Big], \tag{5.1}$$

where τ_0 (the proper formation time) and σ (the width of the gaussian) are variable parameters which are adjusted to obtain the best fit. In our case a formation time of zero gave the best fit showing that we did not produce enough K^0_s's and Λ's.

The secondary particles materialize along the trajectory of the CM system of

† This is because N*'s are the angular momentum excited states having larger sizes than s wave states. However, the 20% was determined phenomenologically from experimental data of p+Au. (see Ref. 20)

the parent particles. If a secondary is formed within the volume of either the target or projectile nucleus, it may interact with nucleons in its path if the closest approach is $< \sqrt{\frac{\sigma}{\pi}}$, where σ is the total cross section of the meson-baryon system. Near the threshold region of the π-nucleon and K-nucleon, an energy dependent cross section is used. An important peak in π-nucleon cross section is Δ formation ($\pi N \rightarrow \Delta$), which is important for the mechanism of pion absorption. After a secondary interacts, the forward leading meson continues to interact while the backward leading baryon is placed in either the target or projectile arrays.

When a secondary interaction occurs, a routine is called (SECINT) which combines a low energy parameterization of meson-meson, meson-baryon, and baryon-baryon interaction which smoothly interfaces with a high energy modified version of MINBIAS which handles mesons as well as baryons. All low energy scattering has been made to agree with data or derivable data through simple isospin relations and factorizable assumptions or directly through T-matrices parameterized by phase shifts or resonances. It should be noted that HIJET never considers a meson-meson collision (this was later estimated not to affect the results on strangeness production).

N*'s were added to HIJET through purely empirical observation[20]. When MINBIAS is called from an initial N-N collision, baryons and mesons are returned. If one combines the forward going non-strange baryon with the forward going non-strange meson and the backward going pair, for a $Si+Au$ collision, one obtains the effective mass spectrum shown in Figure[5.16]. Each pair shown in Figure[5.16] can then become an isobar that will propagate to the next collision. By this mechanism, energy that would ordinarily be expelled is carried on to the next collision. N*'s may collide with other particles to create new particles or they may decay into what they were formed from.

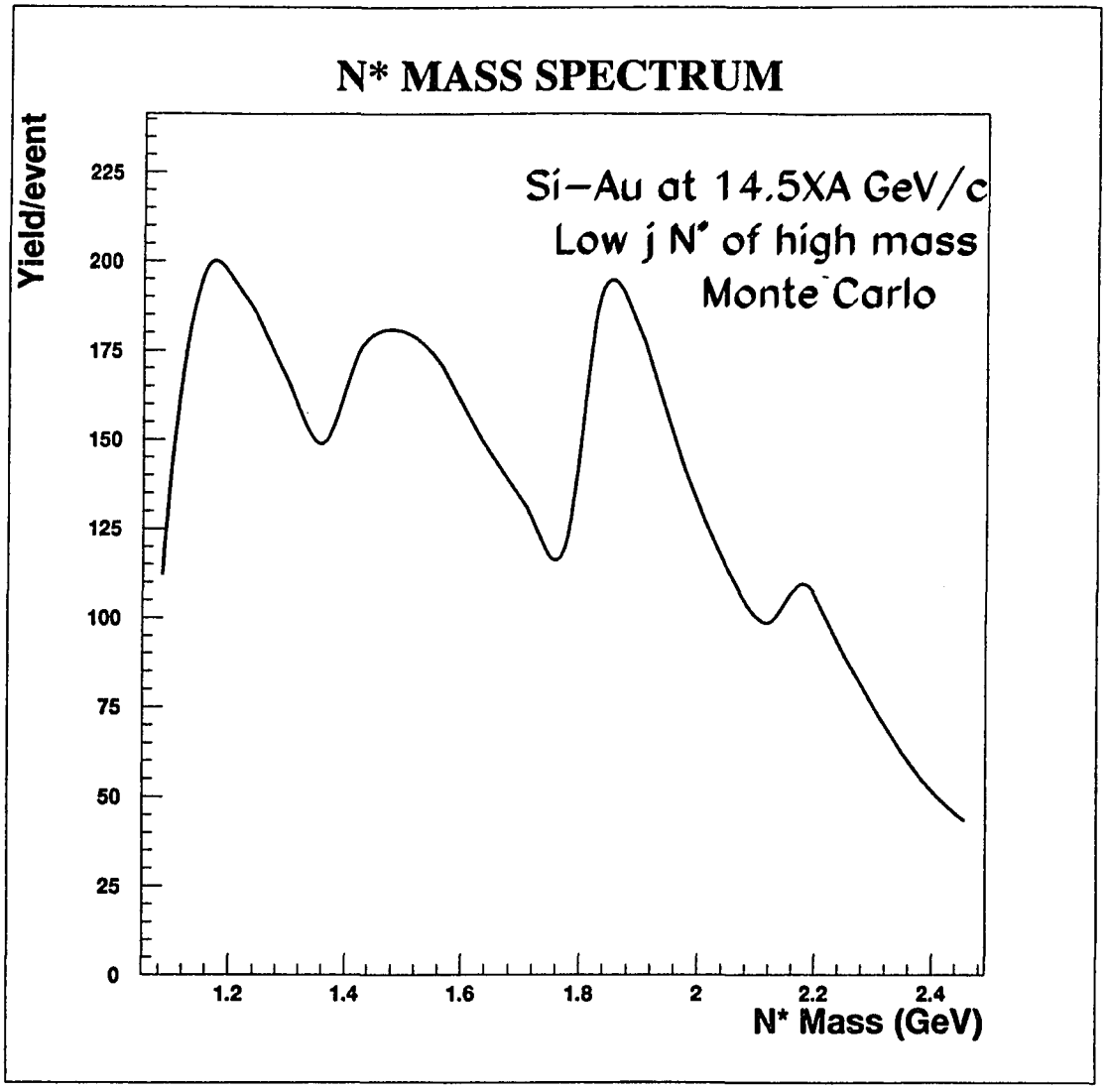

Figure[5.16] N* effective mass spectrum (yield per GeV) generated by MINBIAS routine for a non-strange baryon with a non-strange meson produced in one central $Si+Au$ collision.

N*'s are formed by the initial collisions of nucleons (the produced particles stick together temporarily) and are propagated to the next collision which takes place on a very short time scale. We then decay all of the N*'s and let their secondaries interact in either the target or the projectile depending on their origin. This method has created more higher energy scatterings. N*'s decay by associated production, and 2% of N*'s were formed out of strange pairs ($K\Lambda$ etc). The branching ratio of N*'s decay into strange pairs depend strongly on the spin of the N*'s. Since the total spin of $K\Lambda$ tends to be low, higher spin N*'s have smaller branching ratios of decaying into strange pairs. The $j = \frac{1}{2}$ and $\frac{3}{2}$ have $\sim 6\%$ branch to strange particles while the $j = \frac{5}{2}$ and $\frac{7}{2}$ have $\sim 0.5\%$. One would naturally expect that all spin states should be formed and be weighted by $2j + 1$. In other words the branching ratio of N*'s to strange particles should be the same as the corresponding ratio for πN scattering at a given N* energy ($\sim$2.5% at 1.7 GeV for instance).

The procedure of making a strange pair via N* decay is illustrated as the following:

To form an N*

$$NN \rightarrow N^*N \tag{5.2}$$

$$N\pi \rightarrow N^* \tag{5.3}$$

then into strange, anti-strange particles:

$$N^* \rightarrow \Lambda K \tag{5.4}$$

$$N^*\bar{K} \rightarrow \Lambda M \tag{5.5}$$

$$N\bar{K} \rightarrow \Lambda M \tag{5.6}$$

$$N^*N \rightarrow \Lambda NK \tag{5.7}$$

Where $\bar{K}$ on the left includes resonances of strange mesons with s=−1, K on the right includes resonances of strange mesons with s=1, and M includes resonances of non-strange mesons.

With the above mechanism, we let all the initial participant nucleons (56 for Si+Si and $\sim$ 146 for Si+Pb) be excited into N*'s, and each successive collision of the initial nucleons in AGSHIJET simulation is based on nucleon–nucleon data. When nucleons interact at these energies they become excited into N*'s which decay into ΛK about 2.5% of the time. For a central Si-Si collision one would expect that all 56 nucleons would be excited into N*'s, thus leading to the AGSHIJET yield of around 1.5 Λ's per event. Production of pairs of K's increases sharply with collision energy and it is only a minor source of K_s^0's in pp collisions at this energy. AGSHIJET+N* makes N*'s a propagation mode in the system by allowing N*'s to propagate to the next collision. This procedure did not increase the number of N*'s, but did create more higher energy collisions, thus increasing the number of ΛK (also $K\bar{K}$) pairs produced. The results are shown in figures[5.4]—[5.7] as a dashed curve and the improved K_s^0 yield is not in bad agreement with the data. The Λ yield in Si+Si collision has underpredicted the data by a factor of two. The Λ yield in Si+Pb collision is increased in the target rapidity region ($0 < y < 1.0$) due to the fact that pions can also produce N*'s by scattering off the initially unstruck nucleons in the Pb nucleus, but the yield in our measured rapidity region ($1.4 < y < 2.9$) also underpredicted our data.

A few other currently used cascade models(e.g. ARC, RQMD, RANDOM), without employing a QGP scenario, have reproduced[2,3,17–20] some of the early heavy ion experimental results on strangeness production which were enhanced over that of a naive cascade of NN collisions. The solid curves in figures[5.4]–[5.7] represent the predictions of the ARC (a relativistic cascade) model[19]. The

calculations for the curves were based on events generated for impact parameter $b < 1$ fm for the Si target and $b < 2$ fm for the Pb target. As can be seen, the ARC model represents the Λ rapidity data well. It seems to have too wide a spread in rapidity for K^0_s, although the total predicted number of K^0_s per event is approximately correct. This discrepancy is a direct result of the pp data input into the cascade which at present achieves the correct overall level of strangeness production with too wide a rapidity distribution. This will be suitably adjusted in future versions of ARC (private communication from the authors of ref.[19]).

N*'s are not included in the dynamics of the ARC model. Instead, production of strangeness occurs in direct channels, both for associated and pair production. The increased amount of strangeness in baryon-baryon channels is due to rescattering of Δ's which have higher collision energy than if they had decayed to a proton and pion and then rescattered. Strangeness production also occurs in πN and $\pi\pi$ rescattering. Resonances continue to scatter until they decay.

We have also worked out a simplified model called RANDOM which uses the same cross section routine (RSIGMA) and scattering routine (SECINT) as in AGSHIJET+N*. The RANDOM model treats mesons and baryons equally and randomly. All the hadrons are placed in one of the three arrays, projectile, target and fireball array. All collisions are allowed except for two incident hadrons from the same fragmentation array. Hadrons are randomly selected to collide with a cross section provided by RSIGMA. The number of collisions was the only adjustable parameter. Another adjustable parameter B was added later to represent the lifetime of N*'s before they decay ($B = 0$ means no decay until the end). Figure[5.17] and Figure[5.18] have shown the reproduction of our K^0_s and Λ data (Si+Pb) by the RANDOM model. We can see that the random model works pretty well despite its lacking of geometrical configuration. It reveals some basic criteria of heavy ion

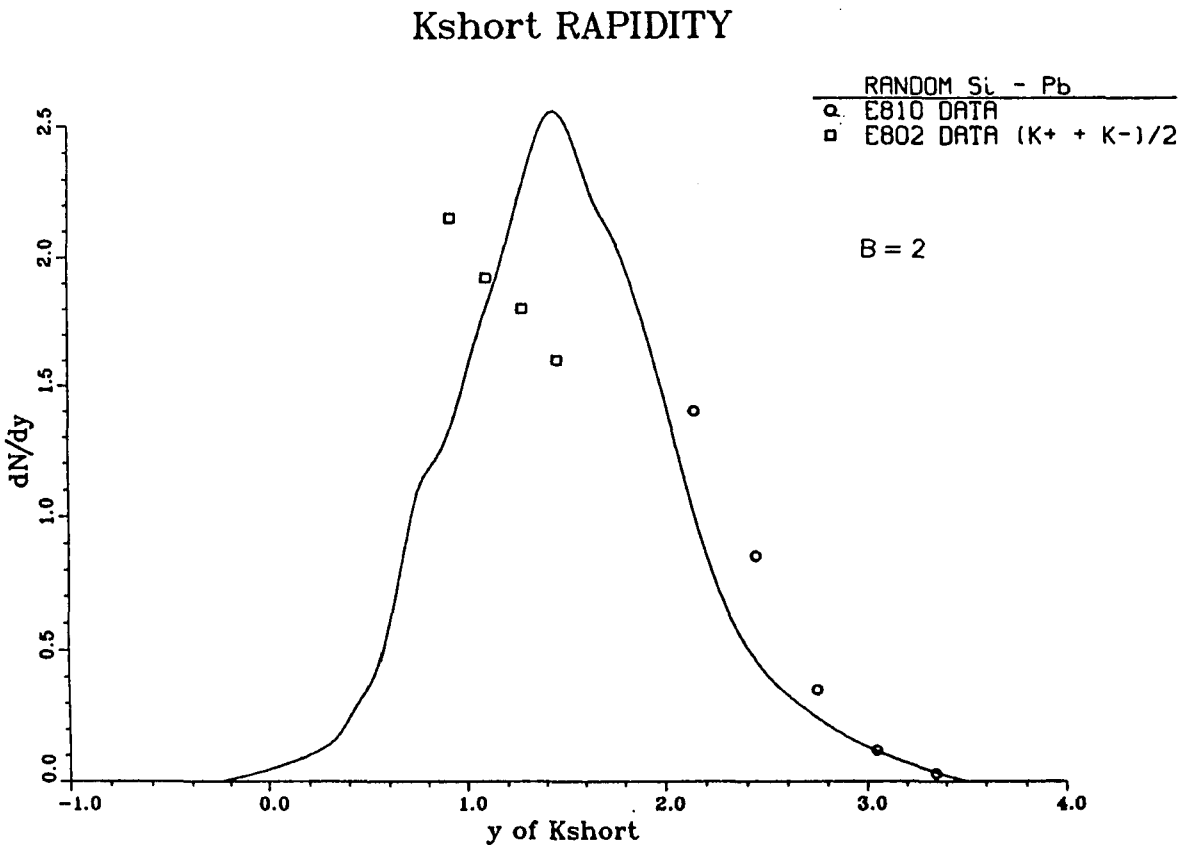

Figure[5.17] The K^0_s produced by our RANDOM model for Si on Pb plotted along with E810 data.

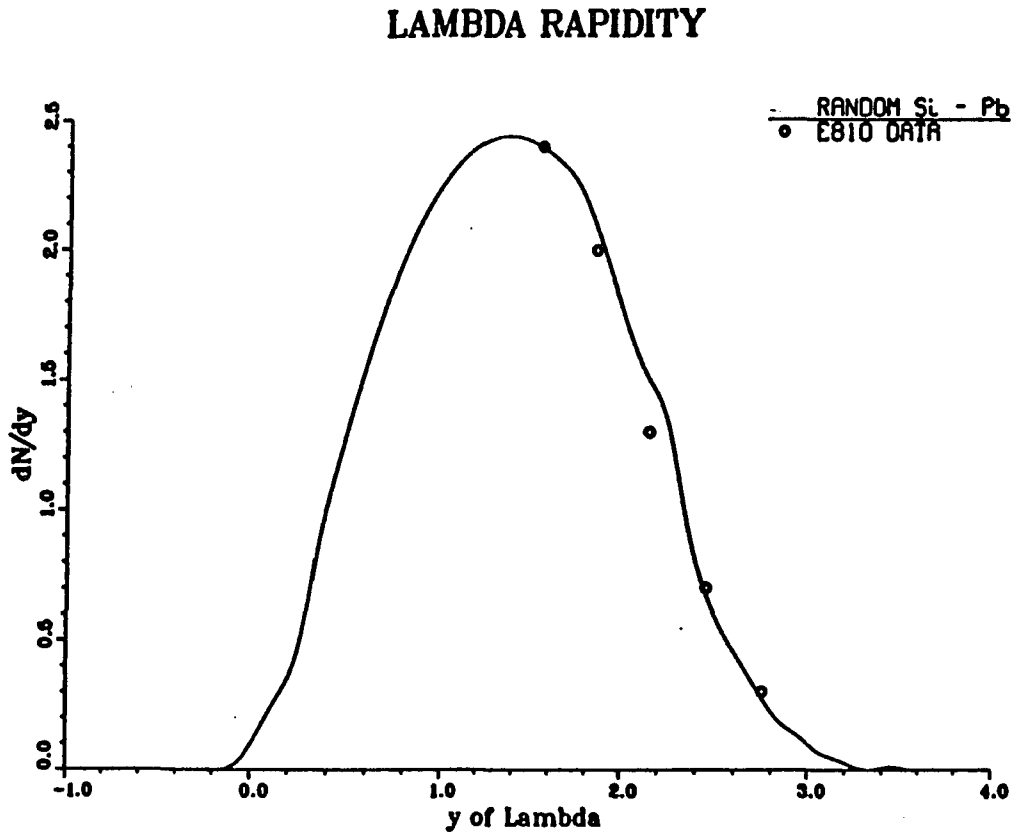

Figure[5.18] The Λ produced by our RANDOM model for Si on Pb plotted along with E810 data.

collisions, such as number of collisions (320 collisions/event for Si+Si) and the temperature range (~250 MeV for Si+Si) etc. With the help of our RANDOM model, we find that for the same number of baryon-baryon and meson-baryon collisions as HIJET for central Si+Pb scattering at the AGS energies one should have 7% additional meson-meson collisions, and it's not enough collisions to affect any of the results coming from AGSHIJET+N*.

5.4 The Ξ^- Production

From the above discussions in section 5.2 and section 5.3, we conclude that we find our measured rapidity distributions of K^0_s and Λs produced by Si beams on Si and Pb targets cannot be accounted for by superposition of nucleon-nucleon interactions, but nuclear cascade models including nuclear isobar production, can be tuned to account for most of the strangeness.

One should have noticed at this point that all the early results of strangeness production in heavy ion collisions have been explained by the currently used cascade models rather well without introducing the QGP scenario. And one common aspect in those early results and model predictions is that they are all single strangeness particle productions. The conventional cascade models reproduced their enhancement by involving rescattering of resonant states like N*'s and Δ's which then decay into a pair of strange particles(e.g. ΛK etc) as we have already discussed in the previous two sections.

As pointed out in Ref.4, the enhancement of particles with single strangeness can not serve as a clean signature of the QGP formation, since it carries too much background information of the hadronized state. However, the theory of strangeness enhancement as a signature of QGP still may be important; the question is how to

observe it!

A multi-strangeness hyperon enhancement could be difficult for conventional cascade models to account for with the same mechanism as they accounted for the single-strangeness productions, because there has to be series of multi-rescatterings of resonant states or rescattering of strange hyperons.

For example, to make a Ξ^- via Y*
(Y=Λ,Σ)

$$YN \rightarrow Y^*N \tag{5.8}$$

$$Y\pi \rightarrow Y^* \tag{5.9}$$

$$N\bar{K} \rightarrow Y^* \tag{5.10}$$

secondly it follows:

$$Y^*\bar{K} \rightarrow \Xi^- M \tag{5.11}$$

$$Y\bar{K} \rightarrow \Xi^- M \tag{5.12}$$

$$Y^*N \rightarrow \Xi^- NK \tag{5.13}$$

$$Y^* \rightarrow \Xi^- K \tag{5.14}$$

Where $\bar{K}$ on the left includes resonances of strange mesons with s=−1, K on the right includes resonances of strange mesons with s=1, and M includes resonances of non-strange mesons.

Since in collisions of non-strange baryons with ordinary valence quarks (u,d quarks), there are less strange quarks than light quarks, Y*'s are harder to form than N*'s. In addition, the strange quark mass is larger than the u, d quark masses

leading to the well known suppression of strangeness production. It makes the production of multi-strange hyperons via conventional ways(as mentioned above) much more difficult than single-strange hyperon production. While in a QGP they will be formed more easily due to the abundance of strange quarks.

During the QGP (Quark Gluon Plasma) phase transition into a HG (Hadron Gas) phase, Ref.5 demonstrates that a large anti-strangeness content will build up in the HG phase while a large strangeness excess will be left in the QGP phase. This excess during hadronization could favor multi-strange hyperon production as well as strangelet formation. With strangelet searches still not successful, hyperons of multiple strangeness is a much better probe for QGP than single strangeness searches. We may conclude that multi-strange hyperons will be more likely to bring us direct information of a QGP if it was formed.

With the procedures described in Chapter 4, we were able to report the first observation of Ξ^- (Figure[4.5]—[4.7]) in heavy ion collisions at the AGS. But due to the limited statistics, we chose to do a model dependent acceptance correction to our Ξ^- data, since as we shall see later important conclusions can be reached within the errors due to model dependence.

In order to calculate acceptances, a complete Monte Carlo simulation of events was performed using GEANT. Since AGSHIJET+N* is the only conventional model that has been tuned for Ξ^- production (special attention has been paid to all the processes we know of that could produce Ξ^- in a hadron gas environment), we first generated events using the AGSHIJET+N* model. These events were processed using GEANT simulating our TPC detector. The generated TPC's hits included all the known effects of the detectors apertures,efficiencies, resolutions, and distortions. The same code has been used to calculate the acceptance of Λ data and

proved successful[3,11]. The lifetime of the Ξ^- is $c\tau = 4.92$ cm as given by Particle Data Group. We measured the acceptance corrected decay distribution for our Ξ^- candidates as a function of proper time as shown in Figure[5.19], which is in good agreement with the known value. This demonstrates that we have indeed observed Ξ^- events, and also gives us confidence in our acceptance calculations.

The acceptance for Ξ^- at different rapidity bins using the AGSHIJET+N* model is shown in Figure[5.20]. The acceptance corrected rapidity spectrum using the AGSHIJET+N* model for the Ξ^- is shown in Figure[5.21] along with AGSHIJET+N*'s prediction scaled up by a factor of 4. This production is equal to 0.15 Ξ^- per central event in the measured rapidity region(1.4-2.9). For $Si + Si$ HIJET underestimated the observed production of single strange particles by a factor of (almost)2. HIJET's factor of 4 underestimation of Ξ^- for $Si + Pb$ leads us to suspect that for some reason, HIJET might have a factor of 2 underestimation for each strange quark.

Due to HIJET's poor job at representing the transverse mass distribution of the Λ's,as shown in Figure[5.22] where data are from Ref.14 and Ref.21, we have reason to believe that HIJET also underproduced Ξ^- in the region of high transverse momentum. Comparing different baryons' m_t distribution in Figure[5.22], we find that the heavier the mass of the particles, the smaller the slope of the m_t spectrum (heavier particles have flatter m_t spectrum[22]). Since neither a satisfactory model prediction nor NN data were available for Ξ^-, we assumed that Ξ^-'s obey the same transverse mass distribution as Λ's and used the fireball$^+$ model (a good fit to our Λ data[3,11]) to do another acceptance study in our measured rapidity region(1.4-2.9). These assumptions yield conservative estimates for Ξ^- production, since this model

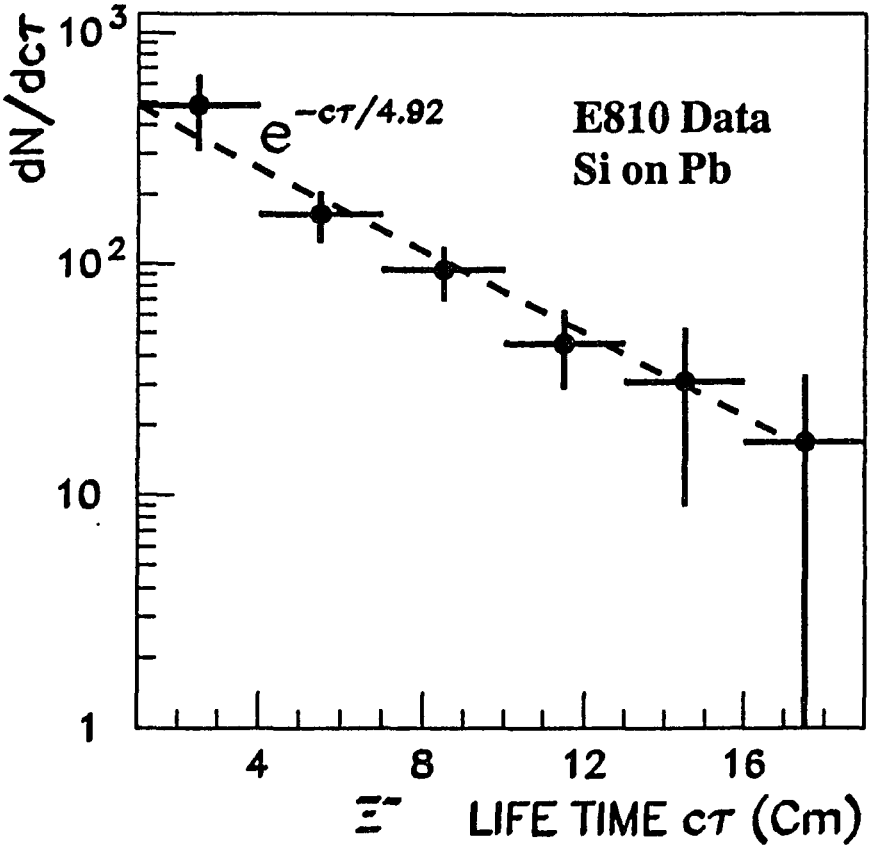

Figure[5.19] The acceptance corrected lifetime (proper time) distribution of the $\pi^-\Lambda$ hypothesis. The dashed line is not a fit, but is the given Particle Data Group value of Ξ^- lifetime.

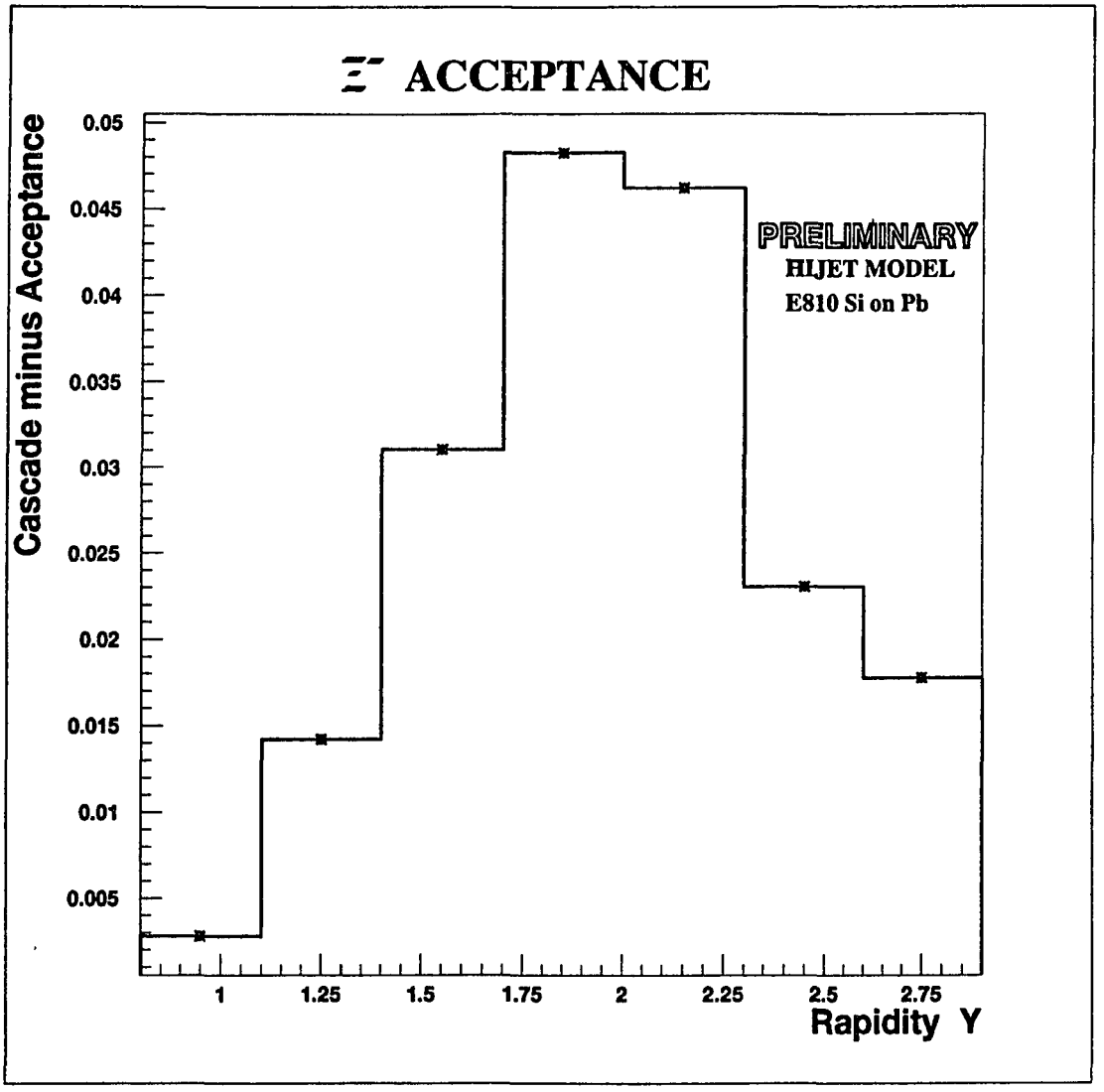

Figure[5.20] The acceptance for Ξ^- at various rapidity bins obtained by using the AGSHIJET+N* model.

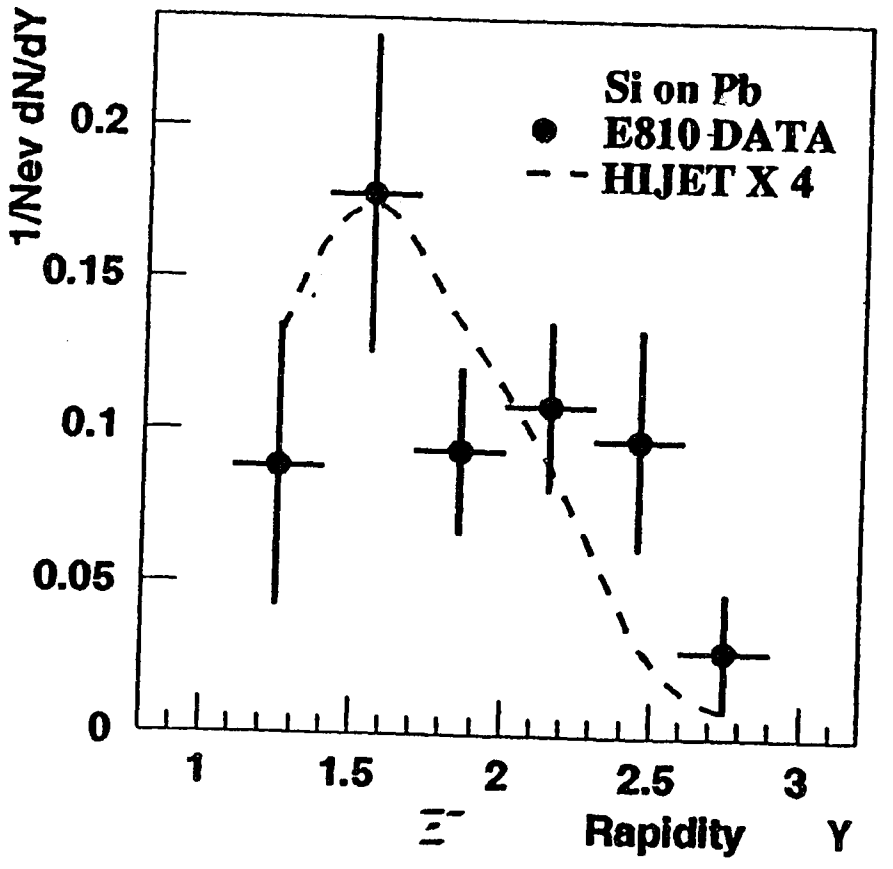

Figure[5.21] The rapidity distribution of Ξ^- after acceptance corrected using the model AGSHIJET+N*.

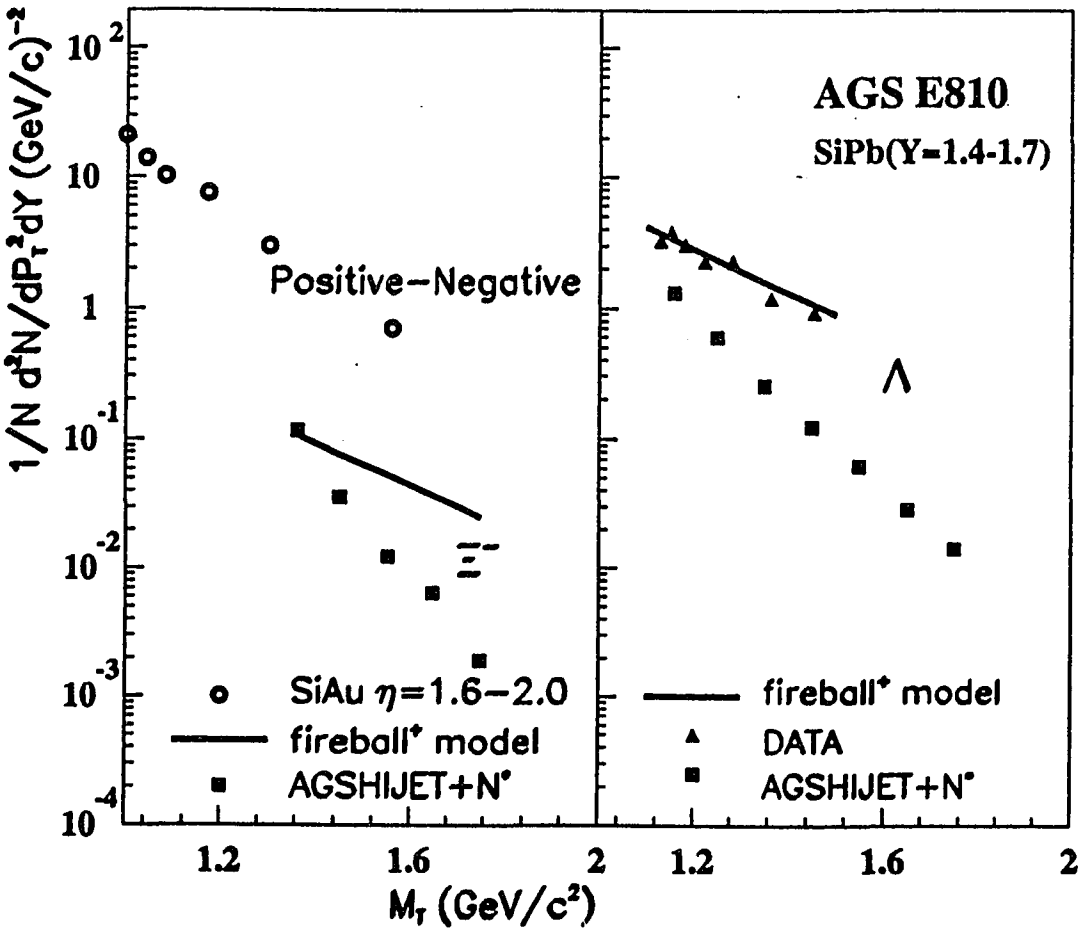

Figure[5.22] The M_t distribution of different baryons from *Si* on *Pb* data plotted along with the prediction of AGSHIJET+N*.

fits the Λ data well, and one would expect on even flatter slop for Ξ^- than for Λ, thus even more Ξ^- production than the model yields. The fireball$^+$ model is[3,11]:

$$\frac{1}{m_t}\frac{d^2N}{dydm_t} = Ae^{-m_t(a+bcosh(y-y_0))}. \tag{5.15}$$

Where A is an arbitrary constant, $m_t = \sqrt{m_0^2 + p_t^2}$, and the cosh term represents a fireball. The constants a, b and y_0 were adjusted to fit E810 data in the measured region ($1.4 \leq Y < 2.9, P_t < 1.0$ GeV/c). They were 2.6712, 1.1071 and 1.2688 respectively. One should note that the constant a simulates the cascade contribution.

The Ξ^-'s generated using the fireball$^+$ model were embedded in HIJET central events, followed by the same Monte Carlo process as above. The acceptance for Ξ^- at different rapidity bins using the fireball$^+$ model is shown in Figure[5.23]. This acceptance gives us the ratio of N(Ξ^-)/N(Λ)=0.12$\pm$0.02 and the yield of 0.25$\pm$0.04 Ξ^- per central event in the measured rapidity region(1.4-2.9) as shown in Figure[5.24] along with 1/8 of our Λ data.

Comparing Figure[5.21] with Figure[5.24], we see that our acceptance calculation is sensitive to the model used mainly due to the high P_t region which is not well measured. With the M_t slope given by HIJET (equivalent to $<$ 100 MeV) as an extreme case of underestimating the Ξ^- production, we find that the ratio of N(Ξ^-)/N(Λ)=0.12$\pm$0.02 has an additional systematic uncertainty of 50% in the range of $0 \leq P_t < P_t^{Max}$. If we restrict the discussion to the well measured $0 \leq P_t < 1.0$ GeV/c, this uncertainty drops to 30%. In a further restricted smaller region of $0 \leq P_t < 0.8$ GeV/c, the uncertainty will be 20%, while the ratio remains the same.

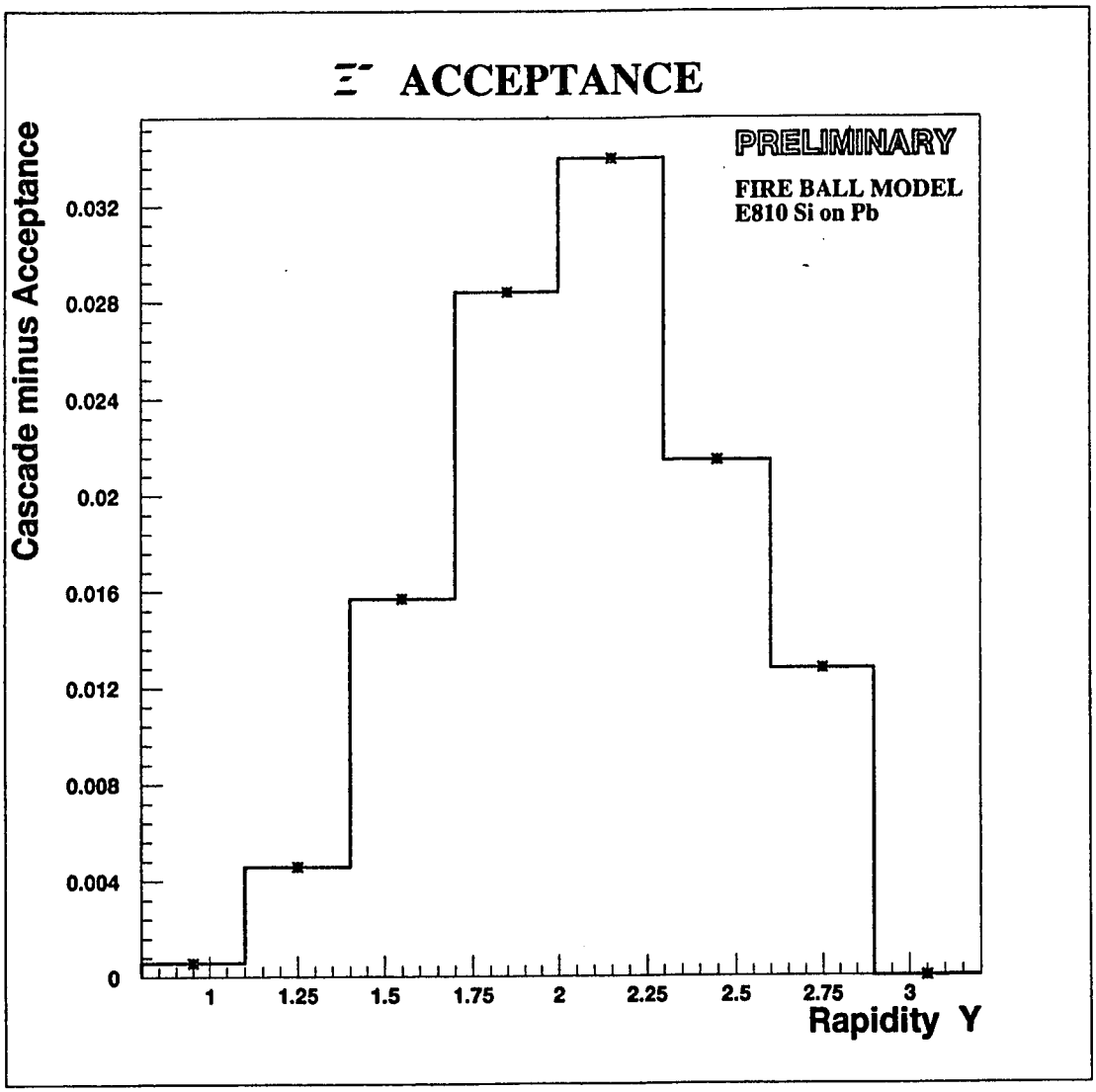

Figure[5.23] The acceptance for Ξ^- at different rapidity bins using the fireball$^+$ model (see text).

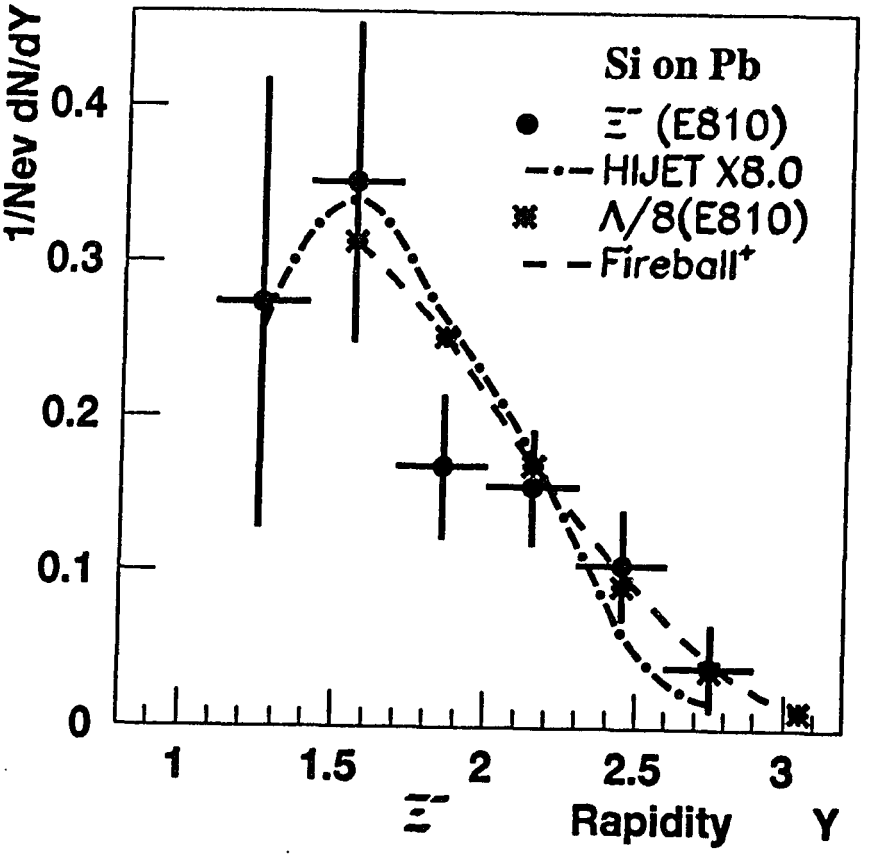

Figure[5.24] The rapidity distribution of Ξ^- after acceptance correction using the fireball$^+$ model (see text).

In conclusion, we have shown in previous discussions that the dN/dY distribution of the detected Ξ^-'s is dependent on its transverse mass slope(Figure[5.21] Figure[5.24]). Since heavier particles have smaller m_t slopes, we believe that using the Λ's m_t slope to calculate the acceptance for Ξ^- is more realistic than using the HIJET cascade model(Figure[5.22]). We conclude that the Ξ^- production(at 14.6×A GeV/c $Si + Pb$) in our data is enhanced with respect to generally known cascade models. In our measured rapidity region(1.4-2.9), we obtained a yield of 0.25 ± 0.04 Ξ^- per central event and a ratio of $N(\Xi^-)/N(\Lambda)=0.12 \pm 0.02$ with a systematic uncertainty of 50%. If we restrict to the best measured smaller region of $0 \leq P_t < 0.8$ GeV/c, this uncertainty in the ratio drops to 20%.

It should be noted that WA85 reported[23] a similar ratio of $N(\Xi^-)/N(\Lambda)= 0.11 \pm 0.02$ at a higher energy (200×A GeV/c $S + W$) in the range of $1 < P_t < 2$ Gev/c and $2.3 < Y < 3.0$. In the table below we compare our data with different cascade models of the ratio of $N(\Xi)/N(\Lambda)$ in the $P_t < 0.8$ GeV range. Note that all presently used cascade models give an $N(\Xi)/N(\Lambda)$ ratio at least a factor of 3 lower than our data. Although these models invoked secondary interactions in their strangeness production (including Ξ^-) and they reproduced single strangeness hadron production amazingly well, their predictions of multi-strange hyperon production are still in disagreement with the data or is not available(ARC[24]).

E810 (data)	$N(\Xi^-)/N(\Lambda)= 0.12 \pm 0.02 \pm 0.025$
AGSHIJET+N*	$N(\Xi^-)/N(\Lambda)=0.02$
RQMD[24]	$N(\Xi^0)^{\#}/N(\Lambda)\approx 0.025$

#: $\Xi^- \sim \Xi^0$ from isospin conservation.

Table[5.2] Abundance of Ξ^- yield relative to Λ in E810 $Si + Pb$ data (in the range of $0.0 < P_t < 0.8$ GeV and $1.4 \leq y < 2.9$) compared with cascade models' predictions.

5.5 The Multi–Λ Production

We considered that multi–Λ production could be another signature of the same value as the multi-strange hyperon production, as far as the quark gluon plasma (QGP) signature is concerned. Excess strangeness production is expected in the QGP environment (with respect to the hadron gas environment). This enhanced strangeness production is going to produce more Λ's when hadronizing. However we lack a quantitative prediction of how much multi–Λ production is necessary to distinguish between QGP and HG phase. We anticipated that a considerable deviation from the poisson distribution in multi–Λ production would be a good smoking gun for QGP, as it would indicate that the higher Λ multiplicity events are not merely due to statistical cascade phenomena, but are related to a change in the physics.

Events of multi–Λ production have been studied and plotted as in Figure[5.25]. Due to limited statistics, no obvious deviation from poisson distribution has been found although we had a five-Λ candidate event in $Si+W$ data. However a multi–Λ event search remains to be one of the interesting subject to be explored further in the future.

5.6 The Possible Resonant States That Decay Strongly

Using the E810 $Si+Pb$ data, we also conducted a search for the possible signals of strange clusters(e.g. H-dibaryon) by studying ΛΛ, Λp and Λπp correlations. Figure[5.26] shows the π^-p correlation, indicating a peak exists at the Δ mass value. We have assumed that all negative tracks are π^-'s and positive tracks with Y>2.3 are protons (this results in 10% contamination of π^+ in proton).

Again, limited statistics has prevented us from drawing a final conclusion, but

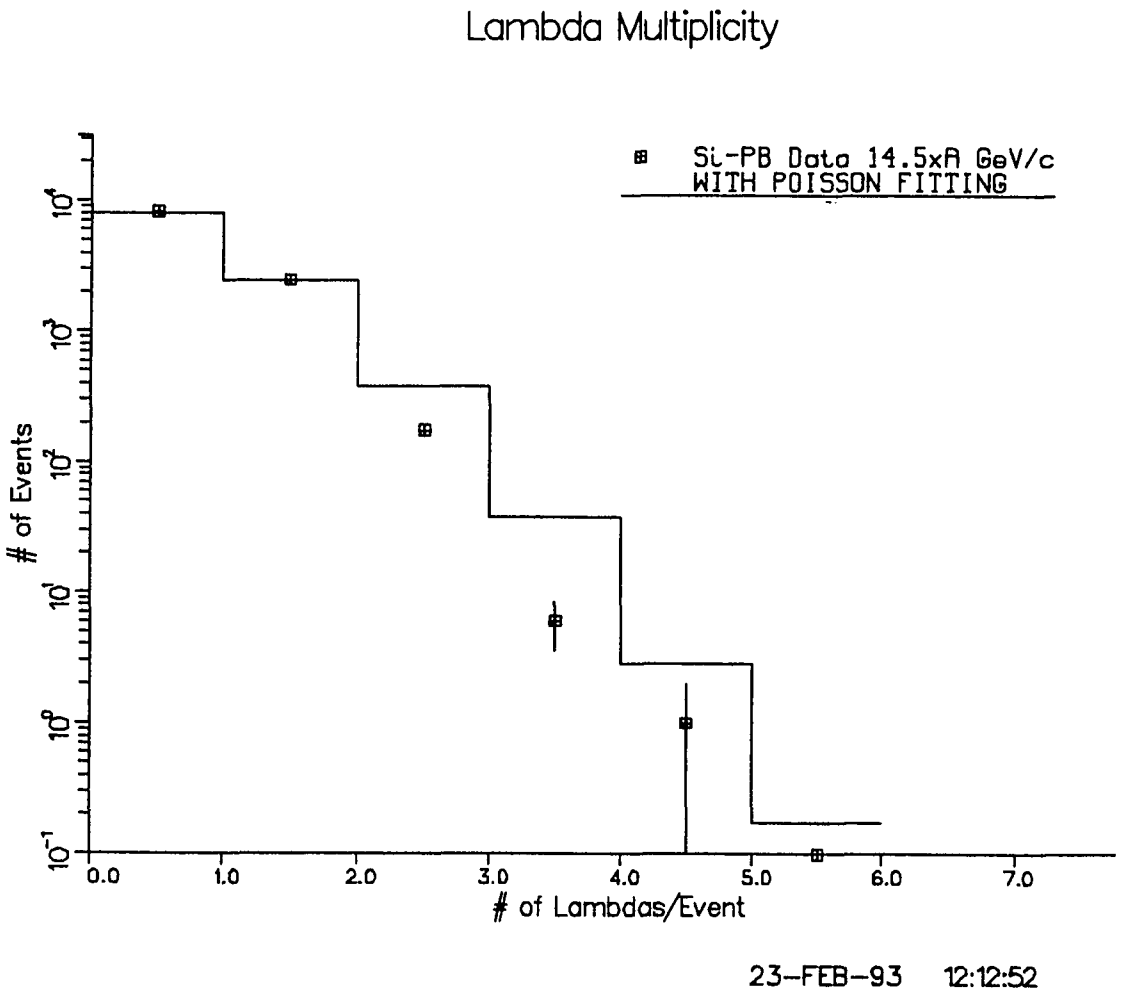

Figure[5.25] Number of central events with multi-Λ production.

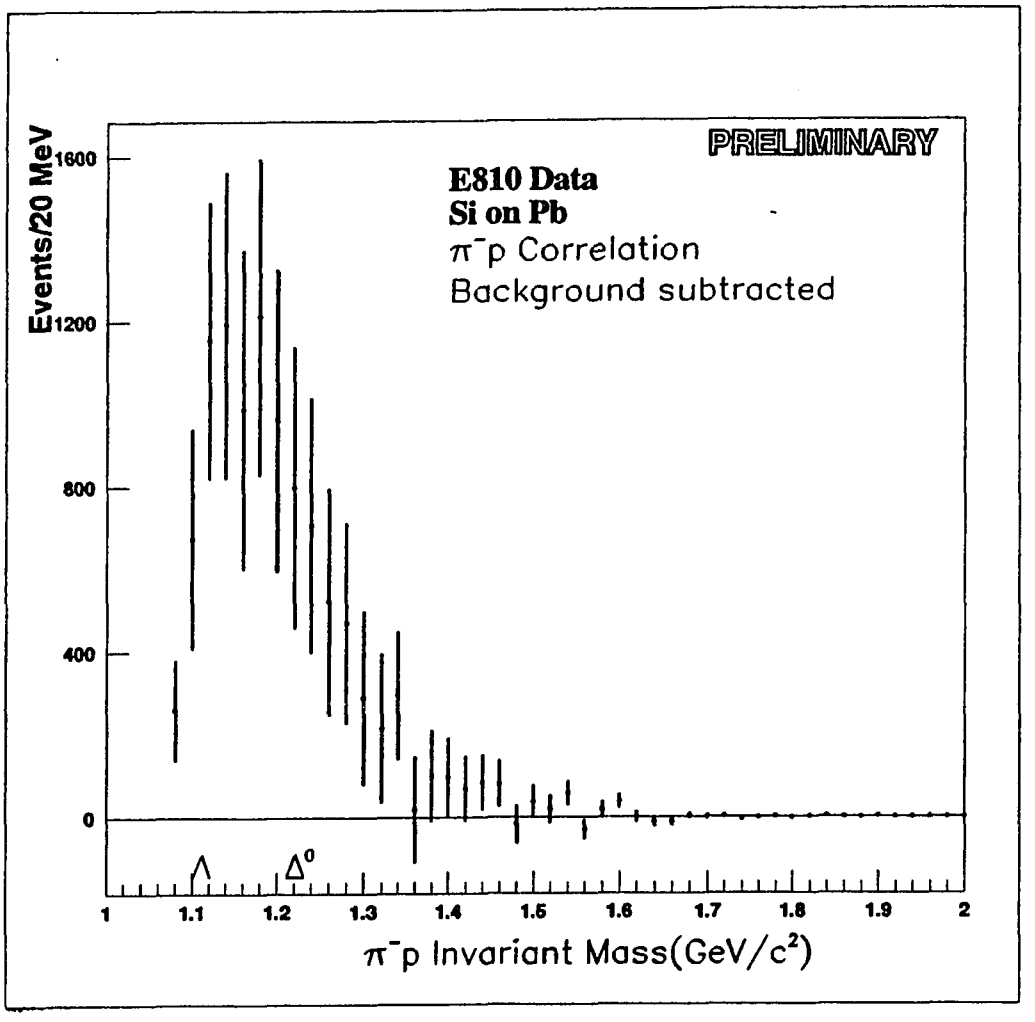

Figure[5.26] The π^-p (from primary target) invariant mass indicating a peak at Δ mass. We have assumed that all negative tracks are π^-'s and positive tracks with Y>2.3 are protons (this results in 10% contamination of π^+ in proton).

interesting correlated phenomena have been detected and remains to be explored further in the $Au+Au$ data.

5.7 Have We Seen The QGP ?

From the above discussion we conclude that we need more data for further study of the multi-Λ production and search for the possible signals of strange clusters (e.g. H-dibaryon). But the Ξ^- signal is enhanced with respect to currently used cascade models, despite the systematic uncertainties introduced due to limited statistics! Obviously the currently used cascade models are challenged by our data.

Does this mean we have seen the quark gluon plasma? With the question in mind, in order to draw a conclusion from our experimental data, we worked out a simple model trying to explain our data.

Following Rafelski's general argument, the number of baryons produced in a heavy ion collision is dependent on the abundance of the corresponding quarks accordingly.

$$P\{duu\} \cdots\cdots\cdots\cdots p(d) \cdot \beta_u \cdot \left(\frac{N_u}{N_{total}}\right) \cdot \beta_u \cdot \left(\frac{N_u}{N_{total}}\right) \tag{5.16}$$

$$\Lambda\{dus\} \cdots\cdots\cdots\cdots p(d) \cdot \beta_u \cdot \left(\frac{N_u}{N_{total}}\right) \cdot \beta_s \cdot \left(\frac{N_s}{N_{total}}\right) \tag{5.17}$$

$$\Xi^-\{dss\} \cdots\cdots\cdots\cdots p(d) \cdot \beta_s \cdot \left(\frac{N_s}{N_{total}}\right) \cdot \beta_s \cdot \left(\frac{N_s}{N_{total}}\right) \tag{5.18}$$

Where on the left are the quark content of the different baryons (proton, Λ and Ξ^-), and on the right hand side are the probabilities of forming these baryons starting

with a d quark to look for u and s quarks in the fireball region and combine them into baryons (hadronize). Here $p(d)$ is the probability of having a d quark to begin with, and β_u (or β_s) represents the probability for a d quark (and it's company) to combine a u (or s) quark when it meets one. N_u (or N_s) is the number of u (or s) quarks available (including created) in the fireball.

In a pure fireball region, everything is created from the collision with the probability described as above and it is easy to see that the following relation stands:

$$\frac{\Lambda \cdot \Lambda}{P \cdot \Xi^-} = 1 \tag{5.19}$$

But in the experimental data, the Λ's we detected included a certain amount from the $\Sigma^0\{dus\}$ decay which is an electro-magnetic decay in a time frame of $7.4 \pm 0.7 \times 10^{-20}$ second. We assume the Σ^0 to Λ ratio is α:

$$\Sigma^0 = \alpha\Lambda \tag{5.20}$$

so that $(1+\alpha)\Lambda$ is the quantity we really measure as Λ.

$$\frac{(\Lambda + \Sigma^0) \cdot (\Lambda + \Sigma^0)}{P \cdot \Xi^-} = (1+\alpha)^2 \tag{5.21}$$

In a pure quark gluon plasma, Λ and Σ^0 will be equally formed (same quark content) without isospin restraints, so that $\alpha = 1$. While in a pure hadron gas phase, from isospin conservation (Λ has I=0 and I_3=0, Σ^0 has I=1 and I_3=0), Σ^0 is only one third of an isospin one state, so that we should have $\alpha = 1/3$.

We hope to determine the α value from our data in order to get a clue about the status of the fireball. Is it due to a QGP or an HG ?

First of all, we have to separate the fireball region from the fragmentation region. With the Λ and Ξ^- data from E810 and proton data from Ref.25, we fitted the following equation:

$$\frac{(\Lambda - F_{Pb}\Lambda_{Pb} - F_{Si}\Lambda_{Si})^2}{(P - F_{Pb}P_{Pb} - F_{Si}P_{Si})\Xi^-} = (1+\alpha)^2 \quad (5.22)$$

Where Λ_{Pb} and P_{Pb} are fragmentation production of Λ and proton from pp data[8] (with a gaussian term added 6:1 peak to peak, representing secondary interactions in the fragmentation region—see Ref.12), while Λ_{Si} and P_{Si} are the reflection of Λ_{Pb} and P_{Pb} about the mid-rapidity. F_{Pb} and F_{Si} are constants to be adjusted. We first had F_{Pb} fixed to make the proton production in the target fragmentation region equal to the total proton production at the target rapidity $y = 0.4$. Then we adjusted the F_{Si} and α to obtain the best χ^2s.

This way we separated the central fireball region from the target and projectile fragmentation region as shown in Figure[5.27], and calculated the α value for the fireball region only. This allows us to look into the hottest region (fireball) with less background from the fragmentation region. In Figure[5.27] solid lines are experimental measurements, dotted lines are the fragmentation products and dashed lines are the particles produced in the fireball. It is very obvious that almost all of the Λs are produced from the fireball, but there are certain amount of protons from the fragmentation of two incident ions (projectile and target). The α values obtained at different rapidity bins were plotted in Figure[5.28]. It is very clearly seen in Figure[5.28] that α is more likely to be closer to 1/3 as calculated from our data, especially at the central rapidity region ($y = 1.7$).

When we fitted the equation (5.22) with one α and one F_{Si} value for all the rapidity bins ($1.4 < y < 2.9$), we obtained an α—χ^2 relation as plotted in Figure[5.29]

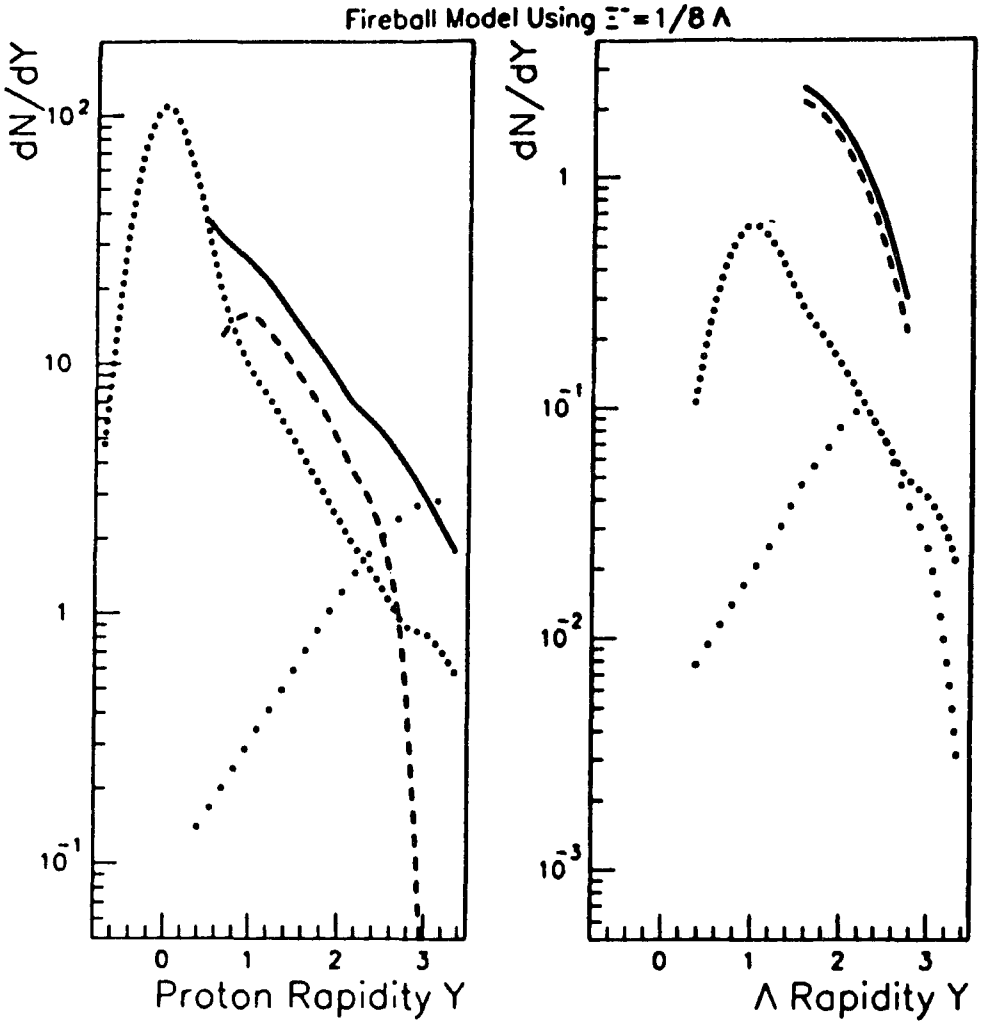

Figure[5.27] The solid lines are experimental measurements, dotted lines are the fragmentation products (target and projectile) and dashed lines are the particles produced in the fireball. It is obvious that almost all of the Λ's are produced in the fireball region.

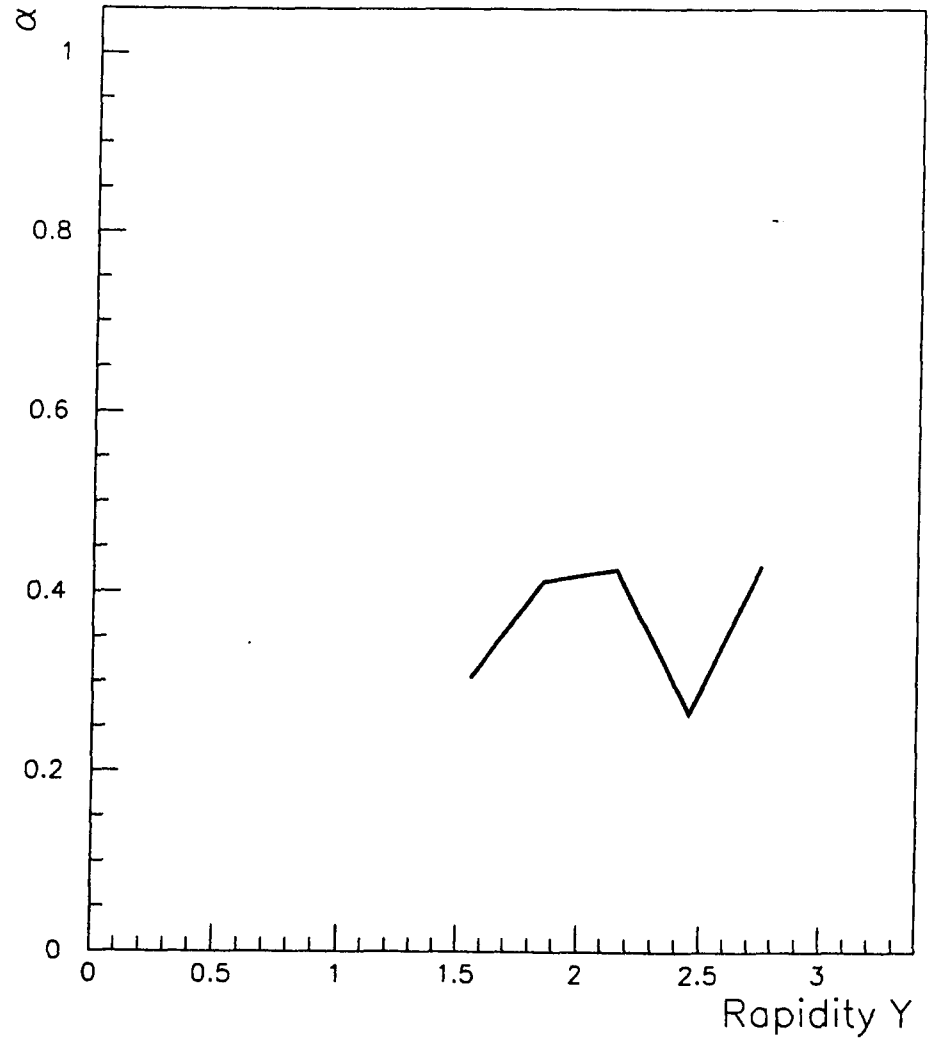

Figure[5.28] The Σ to Λ ratio (α) as a function of rapidity.

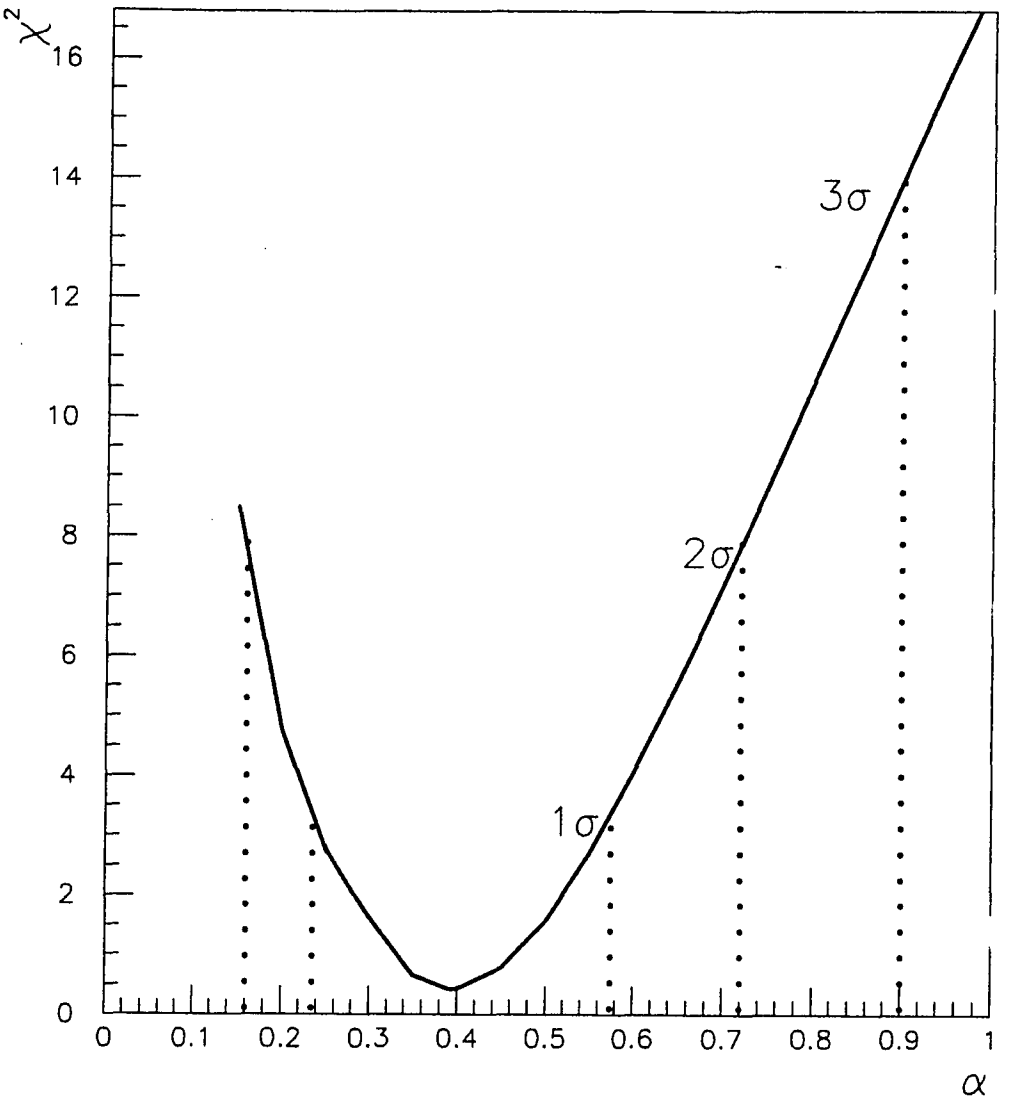

Figure[5.29] The confidence level as a function of α value (percentage of Σ content in Λ detected).

from which we conclude that with 95% confidence level $0.15 < \alpha < 0.7$, and the confident level for $0.24 < \alpha < 0.58$ is 68%.

From the simple model discussed and it's fit to our data, it seems that a hadron gas picture is favored as the predominant component, but we still cannot rule out the possibility of an accompanying QGP phase for the following two reasons:

(a). The QGP phase achieved by AGS $Si + Pb$ may be just a small fraction of the total, and the only way to confirm it is probably a decisive strangelet signal or an enhanced Ξ^- (or multi-Λ) signal which cannot be explained by a theoretical model without invoking a QGP scenario.

(b). When a quark gluon plasma hadronizes, it will first evaporate excited resonant states with higher energies. Then these resonant state collide and decay into the particles that finally reach our detectors. The decay products of these resonant states will be distributed just like a hadron gas, and the α value calculated from this part of the data will be 1/3, which will obscure the α value from the QGP phase if any.

The conclusion is, our Ξ^- data still contradicts the available conventional cascade models because of the enhanced strangeness productions. Further theoretical study is needed to explain the data. Our simple model with indictor α is probably not a sensitive approach to determine if some quark gluon plasma formation occurs. It really is only a usefully indicator of QGP if large amounts of QGP were formed in a large fraction of the central collisions.

Chapter 6

Summary

This thesis work has been concentrated on strangeness production in heavy ion collisions at the AGS energies, especially multi-strange hyperon and multi-Λ productions.

In searching for a Quark Gluon Plasma (QGP) in heavy ion collisions, the strangeness enhancement has long been regarded as one of the most promising signatures[1]. The BNL and CERN experiments reported significantly enhanced production of single strangeness particles over that of a simple cascade of NN collisions[2,6,9,13,23]. However, recent cascade models such as RQMD, ARC and AGSHIJET+N*[15,20], RANDOM have reproduced these results reasonably well at AGS energies by involving rescatterings of resonant states such as Δ and N^*[2,3,10,18,19]. The enhancement of particles with single strangeness cannot serve as a clean signature of the QGP formation[4]. We consider hyperons of multiple strangeness a much better probe for QGP than single strangeness hadrons, since their production more directly measures the expected high strangeness density[5] in a QGP. Ref. 5 pointed out that $\bar{s}$ quarks will buildup in HG phase during hadronization and there will be an excess of s quark content left in the plasma phase. E802 and E810 data have shown that indeed $\bar{s}$ quarks, in the form of K^+ and K^0_s† respectively, are enriched in the hadronic sector. We anticipated that multi-strange hyperon formation is likely to be favored in the final stage of the hadronization of the plasma phase. Therefore, we have searched for Ξ^- in the E810 $Si+Pb$ data.

---

† The K^0_s's we measured in our experiment are indistinguishable from $\bar{K}^0_s$'s.

We searched for vertices of well measured negative tracks (sagitta $\geq$ 0.375 cm) with 4894 Λ's from the Pb target data sample (requiring neither should fit the primary vertex). The Ξ^- defined by these vertices was extrapolated to the target (using $\vec{P}(\Xi^-) = \vec{P}(\Lambda) + \vec{P}(\pi^-)$) and required to match the primary vertex. A reconstructed Ξ^- decaying in our TPC modules is shown in Figure[4.6] and Figure[4.7].

For all the vertices that survived the above cuts, we calculated their effective mass (Figure[4.5]). We selected those 99 candidates that lie in the range of 1.306-1.336 GeV/c^2 as our Ξ^- signal. Those 22 which lie in the range of 1.280-1.294 GeV/c^2 and 1.348-1.364 GeV/c^2 (outside our Ξ^- width) are treated as backgrounds. We have a clear Ξ^- signal (Figure[4.5]) with the right lifetime (Figure[5.19]). Using mixed tracks from different observed events showed no such peak (Figure[4.8]). We also analyzed 0.5×10^6 Ξ^- Monte Carlo events to make sure that this mass peak was not caused by the cuts applied (Figure[4.9]).

In order to calculate the acceptance corrections for the rapidity distribution, we performed a complete Monte Carlo simulation of the effects of the apparatus and cuts to our final data sample using HIJET events embedded with Ξ^- generated by AGSHIJET+N* and Fireball$^+$ models. The GEANT3 program was used to track the generated particles through a magnetic field and the simulated signals in the TPC were written out in the same format as our recorded data. The generated hits included all the known effects of detector apertures, efficiencies and distortions. The results of this simulation were then analyzed by the same program used to analyze the actual data, including the tracking.

Due to the limited statistics of our Ξ^- data, the acceptance calculation was not done as we did for Λ and K^0_s, which is to cut the momentum space into small grids (in rapidity and transverse momentum space). Instead, we chose to calculate

the acceptance in each rapidity bin and treat the transverse momentum distribution as an integrated quantity. This way we have introduced a certain level of dependence of yield on the transverse momentum distribution, or in other words, model dependence (depending on the P_t distribution of the Ξ^- generated for acceptance calculation). The systematic errors introduced by this model dependency was calculated.

Comparing different baryons' m_t distribution in Figure[5.22], where data are from Ref. 14 and Ref. 21, we find that the heavier the particles, the flatter their m_t spectrum[22]. Since Ξ^- is heavier than Λ, we assumed that Ξ^-'s obey the same transverse mass distribution as Λ's‡ and used our fireball$^+$ model (a good fit to our Λ data[3]) to do acceptance calculation in our measured rapidity region(1.4-2.9). Since the Ξ^- is heavier than the Λ, the slope of its m_t distribution is expected to be flatter than that for the Λ. Thus this is a conservative assumption which would underestimate Ξ^- production. The fireball$^+$ model (includes a fireball plus a term simulating a cascade) is[3]:

$$\frac{1}{m_t}\frac{d^2N}{dydm_t} = Ae^{-m_t(a+bcosh(y-y_0))}. \tag{6.1}$$

Where A is an arbitrary constant, $m_t = \sqrt{m_0^2 + p_t^2}$, and the cosh term represents a fireball and the constant a represents a cascade term. The constants a, b and y_0 were adjusted to fit E810 data in the measured region ($1.4 \leq Y < 2.9, P_t < 1.0$ GeV/c). They were 2.6712, 1.1071 and 1.2688 respectively. The constant a simulates the cascade contribution.

In the measured rapidity region(1.4-2.9) for 14.6×A GeV/c Si on Pb, this acceptance gives us the ratio of N(Ξ^-)/N(Λ)=0.12±0.02 and the yield of 0.25±0.04

‡ Since Ξ^- is heavier than Λ, this assumption should give a lower value for the ratio N(Ξ^-)/N(Λ).

Ξ^- (in the region of $1.4 \leq y < 2.9$ and statistical errors only) per central event as shown in Figure[5.24] along with 1/8 of our Λ data. This result is larger than any cascade model prediction so far.

We find that the shape of our acceptance calculation is relatively model insensitive, but the total yield is sensitive (mainly due to the high P_t region which is not well measured)[§]. The M_t slope given by AGSHIJET+N* (equivalent to < 100 MeV) is an extreme case of underestimating the $N(\Xi^-)/N(\Lambda)$ ratio, from which we find $N(\Xi^-)/N(\Lambda)=0.12\pm0.02$ has an additional systematic (model) uncertainty of $\approx 50\%$ in the range of $0 \leq P_t < P_t^{max}$. Using the same procedure, in the range of $0 \leq P_t < 0.8$ GeV/c, the uncertainty is $\approx 20\%$ for this value. It also should be noted that an overall scale uncertainty of $\approx 20\%$ exists, but this will not affect the ratio of $N(\Xi^-)/N(\Lambda)$.

One should note that all experiments, even with high overall statistics, need a model to cover regions used and measured with insufficient statistics. As the statistics increases the model dependence decreases. Since in the Λ case the model dependence was small compared to the other errors, and since we are using the same model (fireball$^+$) based on our previous discussion, we conclude that our acceptance corrections are reasonable within the limited statistics and stated systematic uncertainties. Any bias in them would lower the calculated $N(\Xi^-)/N(\Lambda)$.

It should be noted that WA85 reported[23] a ratio of $N(\Xi^-)/N(\Lambda)= 0.11 \pm 0.02$ at a higher energy (200×A GeV/c $S + W$) in the range of $1 < P_t < 2$ Gev/c and $2.3 < Y < 3.0$. In the table below we compare our data for the ratio of $N(\Xi^-)/N(\Lambda)$ in the $P_t < 0.8$ GeV range with different cascade models. Note that all presently

---

§ For example, AGSHIJET+N* gave a factor of 2 lower total (uncut) yield of Ξ^- than the fireball$^+$ model.

used cascade models give an N(Ξ)/N(Λ) ratio at least a factor of 3 lower than our data. Although these models invoked secondary interaction in their strangeness production (including Ξ^-) and they reproduced single strangeness hadron production amazingly well, their predictions of multi-strange hyperon production are still in disagreement with our data or is not available(ARC[24]).

We conclude that the Ξ^- production(at 14.6×A GeV/c $Si + Pb$) in our data is enhanced with respect to generally known cascade models. Of course some QGP production (of Ξ^-/Λ) could naturally explain our data[1].

E810 (data)	N(Ξ^-)/N(Λ)= $0.12 \pm 0.02 \pm 0.025$
AGSHIJET+N*	N(Ξ^-)/N(Λ)=0.02
RQMD[24]	N(Ξ^0)$^{\#}$/N(Λ)$\approx$0.025

$^{\#}$: $\Xi^- \sim \Xi^0$ from isospin conservation.

Table[6.1] Comparison of our data with currently used cascade models' predictions ($0 < P_t < 0.8$ GeV/c, and $1.4 \leq y < 2.9$).

We tried to explain our data with a simple model as described in Chapter 5. Due to the fact that in a quark gluon plasma, all quarks are free, Λ's and Σ^0's will be formed equally. While in a hadron gas phase, Σ^0 will be formed less abundantly than Λ. Our model tried to use the ratio of $\frac{\Sigma^0}{\Lambda}$ calculated from our data as an indicator of the quark gluon plasma formation. The answer favors a hadron gas picture. But still, the model may not be a sensitive approach to confirm a quark gluon plasma formation because when a QGP hadronizes, it will first evaporate a large amount of excited resonant states which have higher energies and will decay into particles that finally reached our detector. These particles will be distributed just like coming from a hadron gas, and it will obscure our signal of quark gluon plasma if we ever had any in a small volume.

We conclude that our experimental results still can not be explained by conventional cascade models. Further theoretical work is needed to better understand our data. It will at least put a tighter constraint on the conventional models if they still don't have to invoke the quark gluon plasma scenario in order to explain our data. So far, the enhanced Ξ^- production in our data remains a challenge to the currently used cascade models, and could naturally be explained by some QGP production.

References:

1. P. Koch, B. Müller and J. Rafelski, Phys. Rep. **142,** 167(1986)
2. S.E. Eiseman *et al.*, Phys. Lett. **B297**(1992) 44-48
3. A. Saulys, Neutral Strange Particle Production at the AGS, in: Proc. Heavy-Ion Physics at the AGS (Massachusetts Institute of Technology, Jan. 1993) 196
4. K.S. Lee, M. J. Rhoades-Brown and U. Heinz, Phys. Rev. **C37,** 1452(1988)
5. C. Greiner, P. Koch and H. stöcker, Phys. Rev. Lett. **58** (1987) 1825.
6. S.E. Eiseman *et al.*, Phys. Lett. **B292**(1992) 10-12
7. A.C. Saulys *et al.*, Comp. Phys. Commun. **57** (1989) 353-357
8. V. Blobel *et al.*, Nucl. Phys. **B69** (1974) 454.
9. Y. Miake *et al.*, Spectra and Strangeness Production, in: Proc. Workshop on Heavy-Ion Physics at the AGS (Brookhaven National Laboratory, March. 1990) p.27
10. R. Mattiello, H. Sorge, H. Stöcker and W. Greiner, Phys. Rev. Lett. **63** (1989) 1459.
11. S.E. Eiseman *et al.*, Phys. Lett. **B248**(1990) 254-258
12. A. Shor and R. Longacre, Phys. Lett. **B218**(1989) 100.
13. T. Abbott *et al.*,Phys. Rev. Lett. **64**(1990) 847.
14. A. C. Saulys *et al.*,Proceedings of the XIII Particles and Nuclei International Conference (PANIC'93) in print.
15. R. Longacre, Proc. Workshop on Heavy-Ion Physics at the AGS (Brookhaven National Laboratory, March. 1990)
16. R. D. Field and R. P. Feynman, Nucl. Phys. **B136,**1(1978).
17. R. Mattiello, H. Sorge, H. Stöcker and W. Greiner, Phys. Rev. Lett. **63** (1989) 1459

18. H. Sorge, R. Mattiello, A. Jahns, H. Stöcker, W. Greiner, Phys. Lett. **B271** (1991) 37

19. Y. Pang, T.J. Schlagel and S.H. Kahana, Phys. Rev. Lett. **68** (1992) 2743

20. R. Longacre, HIJET with AGS Physics and N*'s, in: Proc. Heavy-Ion Physics at the AGS (Massachusetts Institute of Technology, Jan. 1993) p.304

21. W. Love *et al.*, AGS Silicon Gold Collisions Measured in the E810 TPC, in: Proc. Workshop on Heavy-Ion Physics at the AGS (Brookhaven National Laboratory, March. 1990) p.27

22. S. Nagamiya, Nuclear Physics **A544** (1992) 5c–26c

23. S. Abatzis *et al.*, Phys. Lett. **B244**(1990)130; **B259** (1991) 508; **B270** (1991) 123. Nuclear Physics **A544** (1992) 321c-334c

24. C. Dover *et al.*, Production of Strange Clusters in Relativistic Heavy Ion Collisions, in: Proc. Heavy-Ion Physics at the AGS (Massachusetts Institute of Technology, Jan. 1993) p.213

25. F. Videbaek, Baryon Distributions in Heavy Ion collisions at AGS energies: An experimental overview, in: Proc. Heavy-Ion Physics at the AGS (Massachusetts Institute of Technology, Jan. 1993) 89